

**PREDICTION OF OXIDE SCALE GROWTH
AND THERMO-MECHANICAL STRESS-STRAIN OF
AUSTENITIC STEEL AND NICKEL-BASED ALLOY TUBES
IN ULTRA-SUPERCRITICAL POWER PLANT**

YEO WEI HONG

**FACULTY OF ENGINEERING
UNIVERSITY OF MALAYA
KUALA LUMPUR**

2017

**PREDICTION OF OXIDE SCALE GROWTH
AND THERMO-MECHANICAL STRESS-STRAIN OF
AUSTENITIC STEEL AND NICKEL-BASED ALLOY
TUBES IN ULTRA-SUPERCRITICAL POWER PLANT**

YEO WEI HONG

**THESIS SUBMITTED IN FULFILMENT
OF THE REQUIREMENTS FOR THE DEGREE OF
DOCTOR OF PHILOSOPHY**

**FACULTY OF ENGINEERING
UNIVERSITY OF MALAYA
KUALA LUMPUR**

2017

UNIVERSITY OF MALAYA
ORIGINAL LITERARY WORK DECLARATION

Name of Candidate: Yeo Wei Hong

Matric No: KHA110087

Name of Degree: Doctor of Philosophy (PhD)

Title of Project Paper/Research Report/Dissertation/Thesis ("this Work"): Prediction of oxide scale growth and thermo-mechanical stress-strain of austenitic steel and nickel-based alloy tubes in ultra-supercritical power plant

Field of Study:

Engineering Design

I do solemnly and sincerely declare that:

- (1) I am the sole author/writer of this Work;
- (2) This Work is original;
- (3) Any use of any work in which copyright exists was done by way of fair dealing and for permitted purposes and any excerpt or extract from, or reference to or reproduction of any copyright work has been disclosed expressly and sufficiently and the title of the Work and its authorship have been acknowledged in this Work;
- (4) I do not have any actual knowledge nor do I ought reasonably to know that the making of this work constitutes an infringement of any copyright work;
- (5) I hereby assign all and every rights in the copyright to this Work to the University of Malaya ("UM"), who henceforth shall be owner of the copyright in this Work and that any reproduction or use in any form or by any means whatsoever is prohibited without the written consent of UM having been first had and obtained;
- (6) I am fully aware that if in the course of making this Work I have infringed any copyright whether intentionally or otherwise, I may be subject to legal action or any other action as may be determined by UM.

Candidate's Signature

Date:

Subscribed and solemnly declared before,

Witness's Signature

Date:

Name:

Designation:

ABSTRACT

The increasing of energy demand and aims of reducing CO₂ emissions promote the future coal-fired fuel power industries to pursue for the higher steam temperatures and pressures to increase the boiler efficiency. Higher operating temperatures and pressures will increase the risk of steam-side oxidation in the boiler tubing and this could post several potential concerns such as the thickening of low thermal conductivity oxide scale can cause rapid increase in the fire-side and steam-side oxidation rates. Furthermore, the associated stresses and strains accumulation during the scale growth can cause scale exfoliation, especially when the hoop strain exceeded a value obtained from the oxide failure criteria. Austenitic steel and nickel-based alloys are often known to be the preferred choice of materials under the aggressive operation environment, thus, the oxidation behavior and thermo-mechanical stress-strain should be investigated when these materials are used for boiler tubing. To date, no literature has been reported on estimating the oxide scale growth and thermo-mechanical stress-strain of austenitic steel and nickel-based alloy tubes under the USC operation. Thus, in this research, a simple and efficient analytical solution was proposed to evaluate the temperature distribution and thermo-mechanical stress-strain of multi-layered cylinder tubes. The analytical solutions were then included into the iterative procedures for the estimation of oxide scale growth in boiler tubes. It would allow the simulation to produce more comprehensive results. The scale growth predictions were verified with actual data from power plants. Meanwhile the results obtained from the analytical thermo-mechanical solutions were compared and verified with those produced by the finite element analysis software of ANSYS. To investigate the events of the scale exfoliation during the service, an oxide scale failure model was adopted, and the parameters for determining the critical strain causing the exfoliation were proposed. Verification of the findings with the published data was provided. The evaluations of the effect of oxide scale growth and presumed exfoliation on

the temperature distribution and thermo-mechanical stress-strain in the boiler tubes (austenitic steel and nickel-based alloy) were carried out. In general, based on the simulations demonstrated in the present work, the oxide scale growth rates of austenitic at steam temperatures of around 650°C seemed to be acceptable in USC operations, meanwhile those of nickel-based alloys at steam temperatures up to 750°C were found to be allowable in the operations. With regard to the potential of faster rates of oxidation, further viability studies and careful consideration on the use of nickel-based alloys for steam temperatures operations of 800°C or higher are required. It was also observed that when both steam-side/ID (inner diameter) and fireside/OD (outer diameter) scales developed on the tube, the ID scales would experience higher strain than that in the OD scales. As a result, the ID scales were more susceptible to oxide scale failure as compared to the OD scales. The research revealed that blockage due to exfoliation of steam-side scale could result in steam flow starvation in the tube thus leading to elevation of the metal temperature, and consequently causing rapid scale growth in the tube.

ABSTRAK

Peningkatan permintaan tenaga dan matlamat untuk mengurangkan pelepasan CO₂ menggalakkan industri kuasa elektrik di masa akan datang terus berusaha giat mencapai peningkatan kecekapan dandang dengan meningkatkan operasi suhu dan tekanan stim yang lebih tinggi. Walaubagaimanapun, dilaporkan bahawa operasi suhu dan tekanan yang lebih tinggi akan meningkatkan risiko pengoksidaan di bahagian dalam tiub dandang dan ini akan meningkatkan kadar kegagalan tiub dandang seperti melalui pengoksidaan di sisi-stim dan pengakisan di tepi perapian. Selain daripada itu, masalah berkaitan tekanan dan terikan meningkat semasa pertumbuhan oksida boleh menyebabkan pengelupasan oksida, terutama sekali apabila terikan melebihi nilai yang diperolehi daripada kriteria kegagalan oksida. Keluli austenik dan nikel aloi sering dikenali sebagai pilihan utama untuk operasi persekitaran dandang yang agresif, maka, pengoksidaan dan termo-mekanik tekanan-terikan hendaklah disiasat apabila bahan-bahan ini akan digunakan untuk pembinaan tiub dandang. Dalam kajian ini, analisis penyelesaian yang mudah dan cekap telah dicadangkan untuk menilai suhu pengagihan dan termo-mekanik tegasan-terikan tiub yang berlapisan. Kemudiannya, penyelesaian analisis yang dicadangkan akan dimasukkan ke dalam prosedur lelaran untuk anggaran pertumbuhan oksida dalam tiub dandang. Ia akan membenarkan simulasi untuk menghasilkan keputusan analisis yang lebih tepat/teliti. Ramalan-ramalan pertumbuhan oksida yang dibuat dalam analisis ini telah disahkan dengan data sebenar dari loji-loji janakuasa. Dalam masa yang sama, keputusan yang diperolehi daripada analisis penyelesaian termo-mekanikal telah dibandingkan dan disahkan dengan yang dihasilkan oleh perisian kaedah unsur terhingga ANSYS. Untuk menyiasat pengelupasan oksida semasa operasi, model kegagalan oksida telah diguna-pakai dan parameter untuk menentukan terikan kritikal yang menyebabkan pengelupasan telah dicadangkan. Pengesahan daripada penyelidikan dengan data yang diterbitkan telah dilaporkan.

Penilaian kesan pertumbuhan oksida dan pengelupasan yang dianggarkan pada suhu pengagihan dan thermo-mekanik tekanan-terikan dalam tiub dandang (dibuat oleh austenik keluli dan nikel aloi) telah dijalankan. Secara amnya, berdasarkan simulasi yang ditunjukkan dalam kerja kajian ini, kadar pertumbuhan oksida daripada austenik pada suhu stim sekitar 650°C seolah-olah boleh diterima dalam operasi USC, manakala oksida yang berasaskan nikel aloi didapati dibenarkan dalam operasi pada suhu stim sehingga 750°C. Dengan mengambil kira potensi kadar pengoksidaan yang lebih cepat, analisis untuk penggunaan nikel aloi dalam operasi suhu stim 800°C atau lebih tinggi lagi memerlukan analisis selanjutnya dengan pelbagai pertimbangan. Juga diperhatikan bahawa apabila pertumbuhan oksida pada tiub di sisi-stim/ID (diameter dalaman) mahupun sisi-perapian/OD (diameter luar), oksida ID akan mengalami terikan yang tinggi berbanding dalam oksida OD. Hasilnya, mungkin kegagalan oksida pada oksida ID lebih tinggi jika dibandingkan dengan oksida OD. Kajian ini mendedahkan bahawa penyekatan yang diakibatkan oleh pengelupasan oksida sisi-stim boleh mengakibatkan pengurangan aliran stim dalam tiub tersebut dengan meningkatkan suhu logam. Ini boleh menyebabkan pertumbuhan oksida secara pantas dalam tiub tersebut.

ACKNOWLEDGEMENTS

I would like to express my appreciation to all the individuals that have supported and guided me throughout the course of my PhD research:

- My project supervisors, Assoc. Prof. Dr. Judha Purbolaksono, Prof. Ir. Dr. Ramesh Singh and Dr. Liew Haw Ling for their tremendous supervision, guidance, knowledge sharing and support rendered throughout the completion of this research and thesis.
- The Ministry of Higher Education Malaysia (MoHE) for the sponsorship of my PhD study via MYBRAIN15 scholarship program.

Finally, I would like to thank my parents and my wife for their patience, constant support and encouragement.

University of Malaya

TABLE OF CONTENTS

Abstract	iii
Abstrak	v
Acknowledgements	vii
Table of Contents	viii
List of Figures	xi
List of Tables.....	xv
List of Symbols and Abbreviations.....	xvi
List of Appendices	xx
CHAPTER 1: INTRODUCTION.....	1
1.1 Background.....	1
1.2 Objectives	5
1.3 Scope of project	5
1.4 Structure of Thesis.....	6
CHAPTER 2: LITERATURE REVIEW.....	8
2.1 Introduction to steam power plant	8
2.2 Materials for boiler components in ultra-supercritical power plant	10
2.3 Heat transfer in superheater and reheater tubes	16
2.3.1 Conduction	17
2.3.2 Convection.....	19
2.4 High temperature oxidation of boiler tube materials	20
2.4.1 Ferritic steels	21
2.4.2 Austenitic steels and Nickel-base alloys	26
2.4.3 Correlation of scale thickness with the Larson-Miller parameter	29

2.5	Thermo-mechanical stress-strain of the cylindrical tube.....	30
2.6	Scale exfoliation and the oxide scale failure diagram	32
2.7	Summary.....	34
CHAPTER 3: METHODOLOGY.....		36
3.1	Introduction.....	36
3.2	Heat Conduction Equation and Thermo-mechanical Stress-strain in Multilayered Tube	36
3.2.1	Priori assumptions	36
3.2.2	Geometry and material properties	37
3.2.3	Boundary conditions.....	38
3.2.4	Heat conduction equations	39
3.2.5	Displacements and stress-strain relations.....	42
3.2.6	Computational procedures.....	48
3.2.7	Convection coefficient of internal flow, h_s	49
3.2.8	Convection coefficient of external flow on tubes, h_g	50
3.3	Iterative procedure for scale growth prediction.....	52
3.4	Failure criteria for oxide scale	55
3.5	Physical Data and Parameters.....	55
3.6	Summary.....	59
CHAPTER 4: RESULTS AND DISCUSSION		60
4.1	Results validation.....	60
4.1.1	Validation for estimation of thermo-mechanical stress-strain developed in oxide scale.....	60
4.1.2	Validation for prediction of oxide scale growth.....	65
4.2	The oxide scale failure diagram.....	69

4.3	Case A: Growth of steam-side oxide scale on tubes	71
4.4	Case B: Growth of both steam-side and fire-side scales	87
4.5	Case C: Growth of both steam-side and fireside scales, exfoliation on fireside scale	95
4.6	Case D: Growth of both steam-side and fireside scales, exfoliation of steam-side scale	98
4.7	Summary.....	101
CHAPTER 5: CONCLUSIONS AND FUTURE WORK		102
5.1	Conclusions	102
5.2	Suggestions for future work.....	104
References		106
List of Publications		114
Appendix		115

LIST OF FIGURES

Figure 2.1: Evolution of ferritic steels for boilers (Masuyama, 2001).....	11
Figure 2.2: Developments of austenitic steels for boilers (Abe, 2014b).....	14
Figure 2.3: Schematic of 2-D axisymmetric tube model with oxide scale on the internal surface of the tube and the thermal resistance for each portion.....	19
Figure 2.4: Typical scale structure formed on ferritic steel (Sabau et al., 2011).	22
Figure 2.5: The oxide morphology of steel alloy formed at high temperature steam environment (Viswanathan et al., 2006b). a) Pure Iron, b) Ferritic steel with ~2%Cr content, c) Ferritic steel with 9-12 %Cr, d) Austenitic Steel with < 20% Cr, e) Ni-based alloy.....	23
Figure 2.6: General trend of oxidation kinetics for ferritic steels as a function of %Cr and temperature (Viswanathan et al., 2006b).....	25
Figure 2.7: Typical oxide morphology formed on coarse-grained, 300-series (18Cr- 12Ni) austenitic steels in steam. Cross section of scale formed on TP304H after 28000 hours at 538 °C and 5bar steam (left) and a schematic representation of oxide types (right) (Shingledecker et al., 2009).	26
Figure 2.8: A schematic representation of oxide scale morphology formed on nickel-based alloys exposed to steam (Shingledecker et al., 2009).....	28
Figure 2.9: Scale thickness increase with temperature and time expressed in terms of Larson Miller parameter (Osgerby & Fry, 2003).	30
Figure 2.10: The oxide scale failure diagram (OSFD)/ Armitt diagram (Armitt et al., 1978)	33
Figure 2.11: Schematic of an advanced oxide scale failure diagram (Schütze et al., 2010).	34
Figure 3.1: Multi-layered tube that is subjected to with steam on the inner surface and flue gas on the outer surface.....	37
Figure 3.2: Inline and staggered arrangements of bare tubes (Purbolaksono et al., 2010).....	52

Figure 3.3: Bands of data for the relationship between the Larson-Miller Parameter and the oxide scale thickness for austenitic and nickel-based alloys (Fry, 2011).....	53
Figure 4.1: Temperature distribution across the tube.....	61
Figure 4.2: Radial stress and strain across the tube.....	62
Figure 4.3: Hoop stress and strain across the tube.	63
Figure 4.4: Estimated steam-side oxide scale growths and the actual data (304H and TP347) from the power plants for austenitic alloys (Uerlings et al., 2008).	66
Figure 4.5: Estimated steam-side oxide scale growths and the actual data of nickel based alloy (Alloy 617) from the power plants (Uerlings et al., 2008).	67
Figure 4.6: Temperature distributions of 2D axisymmetric solid in superheater tubes in FEA after 80000 h.....	68
Figure 4.7: Comparison of simulated results obtained from analytical method and FEA.	68
Figure 4.8: Oxide scale failure diagram of magnetite (Fe_3O_4).....	70
Figure 4.9: Oxide scale failure diagram of chromium oxide (Cr_2O_3).....	70
Figure 4.10: Model 1 with austenitic steel (TP347HFG): (a) estimation of oxide scale growth and metal temperature using different LMP fitting constants, (b) hoop stress and strain developed during the oxide growth.	72
Figure 4.11: Model 2 with different size of tube: (a) estimation of oxide scale growth and metal temperature, (b) hoop stress and strain developed during the oxide growth.....	74
Figure 4.12: Models with austenitic steel working under steam temperature ranging from 600°C to 750°C: (a) estimation of oxide scale growth and metal temperature, (b) hoop stress and strain developed during the oxide growth.....	76
Figure 4.13: Representation of oxide scale failure diagram and evolution of strain in the magnetite (Fe_3O_4) layer formed on austenitic tube under Models 1, 2, 3 and 6.....	77

Figure 4.14: Model 3 with austenitic (TP347) and nickel-based alloy (A617): (a) estimation of oxide scale growth and metal temperature using upper band and mean value of C_m in LMP equation, (b) hoop stress and strain developed during the oxide growth.....	79
Figure 4.15: Models 3, 4 and 5 with nickel-based alloy (A617) under different flue gas temperatures: (a) estimation of oxide scale growth and metal temperature, (b) hoop stress and strain developed during the oxide growth.....	81
Figure 4.16: Models 6, 7 and 8 with nickel-based alloy (A617) under different flue gas temperatures: (a) estimation of oxide scale growth and metal temperature, (b) hoop stress and strain developed during the oxide growth.....	82
Figure 4.17: Models 9, 10 and 11 with nickel-based alloy (A617) under different flue gas temperature: (a) estimation of oxide scale growth and metal temperature, (b) hoop stress and strain developed during the oxide growth.	83
Figure 4.18: Representation of oxide scale failure diagram and evolution of strain in the Cr_2O_3 layer formed on nickel-based alloys tube under the steam temperature of $700^\circ C$ (Models 3, 4, 5).	85
Figure 4.19: Representation of oxide scale failure diagram and evolution of strain in the Cr_2O_3 layer formed on nickel-based alloy tube under the steam temperature of $750^\circ C$ (Models 6, 7, 8).	86
Figure 4.20: Representation of oxide scale failure diagram and evolution of strain in the Cr_2O_3 layer formed on nickel-based alloy tube under the steam temperature of $800^\circ C$ (Models 9, 10, 11).	86
Figure 4.21: Model 2 with (case B) and without (case A) fireside scale: (a) estimation of oxide scale growth and metal temperature, (b) hoop stress and strain developed during the oxide growth.	88
Figure 4.22: Model 3 with austenitic (TP347) and nickel-based alloy (A617): (a) estimation of oxide scale growth and metal temperature, (b) hoop stress and strain developed during the oxide growth.	90
Figure 4.23: Representation of oxide scale failure diagram and evolution of hoop strain in the magnetite (Fe_3O_4) layer formed on inner (ID) and outer diameter (OD) of austenitic tube (Models 2 and 3).	91
Figure 4.24: Model 6 with Ni-based alloy (A617): (a) estimation of oxide scale growth and metal temperature, (b) hoop stress and strain developed during the oxide growth.....	92

Figure 4.25: Model 9 with Ni-based alloy (A617): (a) estimation of oxide scale growth and metal temperature, (b) hoop stress and strain developed during the oxide growth.	93
Figure 4.26: Representation of oxide scale failure diagram and evolution of hoop strain in Cr ₂ O ₃ layer formed on inner (ID) and outer diameter (OD) of nickel-based alloy tube under Models 3, 6 and 9.....	94
Figure 4.27: Effect of fireside scale formation and exfoliation on oxide scale growth and average metal temperature in (a) Model 2 (austenitic steel, TP347HFG) and (b) Model 7 (Ni-based alloy, A617)..	97
Figure 4.28: Effect of fireside scale formation and exfoliation on heat flow in Models 2 and 7.....	98
Figure 4.29: The exfoliation and re-growth of the steam-side oxide scale in Model 2 with austenitic steel (TP347HFG) at 650°C steam condition.	100
Figure 4.30: The exfoliation and re-growth of the steam-side oxide scale in Model 6 with nickel-based alloy (A617) at 750°C steam condition.	100

LIST OF TABLES

Table 2.1:	Types of Boilers and the mode of combustion (D. Zhang, 2013)	9
Table 2.2:	Types of Nickel Based Alloys (Wheeldon & Shingledecker, 2013).	15
Table 2.3:	Materials for different categories of supercritical boiler tubes (Wheeldon & Shingledecker, 2013)	16
Table 2.4:	General forms of oxide correlation for low alloy Cr-Mo steels.	25
Table 3.1:	Properties of steam and flue gas	56
Table 3.2:	Geometry of tube models.....	56
Table 3.3:	Properties of tube wall materials	57
Table 3.4:	Parameters used to determine gas mass velocity G_v	57
Table 3.5:	Materials and heat transfer parameters referring to properties presented in Table 3.1 and Table 3.3	58
Table 3.6:	The steps of time used in the incremental procedure.....	58
Table 4.1:	Hoop stress and hoop strain results in the oxide layer using present proposed method, Sabau & Wright method and FEA.....	65
Table 4.2:	The correlation functions (B) of nickel based models	84

LIST OF SYMBOLS AND ABBREVIATIONS

q_{steam}''	Heat flux of steam
$q_i''(r)$	Heat flux in layer i
$q_{fluegas}''$	Heat flux of flue gas
h_s	Coefficient of convection of steam
\bar{T}_0	Temperature on the inner surface of tube
\bar{T}_{steam}	Temperature of steam
k_1	Thermal conductivity of 1 st layer
k_i	Thermal conductivity of layer i
k_n	Thermal conductivity of last layer
r_0	Radius of the inner surface of tube
r_n	Radius of outer surface of tube
p_0	Pressure on the inner surface of tube
$\sigma_{rr,i}$	Radial stress of layer i
h_g	Coefficient of convection of flue gas
\bar{T}_n	Temperature on the outer surface of tube
\bar{T}_{gas}	Temperature on the flue gas
$\sigma_{rr,n}(r_n)$	Radial stress on the outer surface of last layer
p_n	Pressure on the outer surface of last layer
$T_i(r_i)$	\bar{T}_i , Temperature of outer surface of layer i
$u_{r,i}(r_i)$	Radial displacement in layer i
$T_i(r)$	Temperature as a function of radius in layer i
\dot{R}_i	internal heat generation of layer i
\dot{R}	internal heat generation
ρ	density
c	specific heat
A_i	Temperature coefficient of temperature distribution in layer i
B_i	Temperature coefficient of temperature distribution in layer i
x_i	$\delta_i \delta_{i+1}$
y_i	$\delta_{i+1} - \frac{k_i}{k_{i+1}}(\delta_{i+1} - 1)$
δ_i	$\frac{\ln r_{i-1}}{\ln r_i}$

L	Length of cylinder
Q	Heat flow
R_{steam}	Thermal resistance of steam
R_{tube}	Thermal resistance of tube
R_{gas}	Thermal resistance of flue gas
E_i	Modulus of elasticity of layer i , GPa
ν_i	Poisson ration of layer i
α_i	Coefficient of thermal expansion of layer i
θ_i	Temperature change
T_i	interfacial temperature of layer i
T_r	temperature at reference point, K
$\epsilon_{rr,i}$	radial strain for layer i
$\epsilon_{\theta\theta,i}$	hoop strain for layer i
$\epsilon_{zz,i}$	axial strain for layer i
ν_i	Poisson ration of layer i
$u_{r,i}$	displacement field component in radial direction for layer i
β_i	$\frac{1}{E_i}$
λ_i	$-\frac{(1+\nu_i)}{E_i}$
u_z	axial displacement
C_z	Constant to determine axial displacement
z	axial coordinate variable
$\epsilon_{r\phi,i}$	Shear strain of $r\phi$ plane
$\epsilon_{rz,i}$	Shear strain of rz plane
$\epsilon_{\phi z,i}$	Shear strain of ϕz plane
E_i	Young modulus of layer i
α_i	temperature expansion coefficient for layer i
C_i	Displacement coefficient in radial direction of layer i
D_i	Displacement coefficient in radial direction of layer i
r	radial coordinate variable
I_i	$-\frac{E_i\alpha_i}{1-\nu_i} \int_{r_{i-1}}^r \theta_i r dr$
φ_i	$\nu_i \epsilon_{zz} / \beta_i$
$\sigma_{rr,i}$	Radial stress of layer i
$\sigma_{\phi\phi,i}$	Hoop stress of layer i

$\sigma_{zz,i}$	Axial stress of layer i
p_i	Interface pressure of between layer i and layer $i+1$
S_i	$\gamma_i \gamma_{i+1} (\lambda_i - \beta_{i+1}) + (\lambda_{i+1} - \lambda_i) \gamma_i$
G_i	$\lambda_{i+1} - \beta_i + (\beta_i - \beta_{i+1}) \gamma_{i+1}$
γ_{i+1}	$\frac{r_i^2}{r_{i+1}^2}$
p_0	Pressure subjected to the internal surface of tube
c_i	recurrence constant
d_i	recurrence constant
e_i	recurrence constant
f_i	recurrence constant
a_i	recurrence constant
p_n	Pressure subjected to the external surface of tube
ω_i	$(f_i - \frac{f_n}{a_n} a_i) p_0$
p_i^o	$\frac{a_i}{a_n} p_n + (e_i - \frac{e_n}{a_n} a_i) p_0$
F_{zz}	axial force
Nu	Nusselt number of steam
Re_s	Reynolds number
Pr_s	Prandtl number
D_0	inner diameter of tube
μ_s	dynamic viscosity of steam
m_s	mass flow rate of steam
Cp_s	specific heat of steam
k_s	thermal conductivity of steam
G_v	gas mass velocity
W_g	gas flow
N_w	number of tube wide
S_t	transverse pitch depending the type of tubes arrangement
μ_g	dynamic viscosity of flue gas
Cp_g	specific heat of flue gas
k_g	thermal conductivity of flue gas
MW	molecular weight
Y	volume fraction
I	gas constituent

LMP	Larson-miller parameter
C_m	Constant to determine LMP
C_h	Constant to determine LMP
X	scale thickness
T	temperature
t	service time (in hour)
X_0	absence of scale
X_I	new scale thickness, $X_0 + \Delta X_I$
ΔX_I	change of scale thickness
K_{Ic}	fracture toughness
f	geometrical parameter
\tilde{c}, \tilde{c}_0	size of a physical scale defect

University of Malaya

LIST OF APPENDICES

Appendix A: The raw data for the Larson Miller Parameter and the scale thickness from National Physical Laboratory, United Kingdom	115
Appendix B: Sample calculation for Case A	118
Appendix C: Sample calculation for Case B	120
Appendix D: Sample calculation for Case C	122
Appendix E: Sample calculation for Case D	124

University of Malaya

CHAPTER 1: INTRODUCTION

1.1 Background

Today, coal remains the backbone of electricity generation and has been the fuel for supporting the rapid industrialization of emerging economies, raising living standards and lifting hundreds of millions of people from the energy poverty. It is estimated that the global population will reach about nine billion by 2050. Due to up-and-coming growth economy and necessity of a better quality of life, sustainable energy resources are required. In comparison to other fossil fuels, e.g. the reserves of oil that are projected to last about 40 years, coal is widely and dispersedly available around the world and is estimated to last about 250 years. Therefore, the global demand and price issue can be resolved by the use of coal (X. Zhang, 2013).

As reported by the International Energy Agency (IEA), the increase of global energy demand is projected to be around 50% by 2030. While realizing an improved quality of life globally, it is not easy to resolve the issues with the solutions that are associated with the increased energy demand (X. Zhang, 2013). Furthermore, in order to address the essential reduction of CO₂ emissions, operating higher stream temperature may be reasonable step to improve the efficiency of coal power plants (Mäenpää et al., 2009). Pollutants and levels of CO₂ resulted from the traditional methods of coal combustion are widely known to be higher in comparison to those by other generation options. Thus, these environmental issues shall be addressed by employing suitable methods while using coal as a generating option in the 21st century (Viswanathan et al., 2006b). Today's modern technology allows coal-fired power plant to emit less pollutants over its life time in comparison to the earlier generations of coal plants that emitted in just a single year (Viswanathan et al., 2005; X. Zhang, 2013). Since technology has grown to be available, it is essential to put into practice the policies that will sustain the advanced development of coal-fired power plants. High-efficiency coal-fired power plant is

purposefully designed for realizing the increase of energy demand and reducing CO₂ emissions (X. Zhang, 2013). Under the supposition of coal as a technologically clean energy source, abundant reserves and the low-level of prices would make coal to be one of the major energy alternatives for oil and gas in the future (Shafiee & Topal, 2009). To this end, the ultra-supercritical (USC) boilers that seem more suitable technology for power generation from coal will be generally employed by the power plant operators (Beer, 2007; Pettinau et al., 2012; Zhong et al., 2012). As reported by Viswanathan et al. (2006a), increasing steam temperature and pressure can simultaneously increase the efficiency and reduce the CO₂ emissions that result from pulverized coal-fired boilers. However, much more economical operation can viably be achieved by raising steam temperature than increasing steam pressure. To preserve the gains of the power plant efficiency with higher steam temperature operation, more advanced materials may be utilized by lowering main steam pressure. Since operating 600°C steam condition in coal-fired power plant has been commercially established with excellent availability (X. Zhang, 2013), several programs for developing advanced ultra-supercritical power plants with steam temperatures above 700°C (e.g., the European AD700 programme, the American A-USC (760°C) programme, and the Japanese A-USC) have been launched. Fukuda (2011) reported the development programs for advanced USC in Japan by particularly focusing on the employments of the candidate materials that have excellent resistances to high-temperature corrosion and steam oxidation. The use of materials that are capable of withstanding steam conditions up to 650°C with a view of arriving at 700°C over the next decade is the aim of the programmes. In addition, China has planned a program that is projected to commence in 2018 for constructing demonstration power plants with operating 700°C steam condition and is targeted for completion by 2020 (X. Zhang, 2013). Therefore, the feasibility of designing an USC boiler operating at 700°C or higher and 35 MPa with current development of candidate materials is encouraging.

The improvement of the coal-fired plant efficiency by more than 50% is generally the overall goal of the programmes worldwide.

Increased rates of strength degradation of materials due to creep and oxidation are well known failure mechanism in higher temperature operations, resulting in a shorter component lifetime. Improvements of the creep strength and oxidation resistance of the material with reasonable cost for high-temperature applications have been the challenges to achieve (Yamamoto et al., 2007). One of the important considerations in the selection of materials for a USC boiler is steam-side oxidation. Power plants operating at higher steam temperatures would pose the possibility of having higher rates of steam-side oxidation. In a power plant, steam-side oxidation could post several potential concerns such as the thickening of low thermal conductivity oxide scale could increase the fire-side and steam-side corrosion rates, and thus promoting the creep rupture of the tube. Besides that, stresses and strains started to accumulate during the scale growth. At a certain point, the scale thickness is unable to bear the increased stress/strain and it releases via cracking and results the scale spallation (Khanna, 2002). Furthermore, the thicker oxide scales may more easily spall during the cooling process of the shutdown of the power plant, blocking steam flow or causing erosion damage of the steam turbine (Henry et al., 2007; Masuyama, 2001). It has also been reported that a combination of practices in service, for example running the plant at near to full load, longer periods between scheduled maintenance, higher steam temperature and pressure and plant cycling, has contributed to further concerns over the increasing thickness of steam-side oxide scales. Consequently, the control of steam-side oxidation is an important factor in the successful operation of a USC boiler, as demonstrated in the US programme sponsored by the U.S. Department of Energy and the Ohio Coal Development Office. In which, one of the main task is devoted to the study of the steam-side oxidation of candidate alloys. The goal of this task is to study the steam-side oxidation behavior and temperature limits of currently

available candidate alloys (Viswanathan et al., 2006b).

It has been widely reported that the austenitic and nickel-based alloys are suitable for higher temperature applications in power plants (Lu, 2010; Weitzel, 2011). In a relevant work, Kritzer (2004) reported phenomena of wet air oxidation and supercritical water oxidation. However, there are relatively few published reports of the systematic collection of data concerning the growth of oxide scales on the steam-side surfaces of austenitic and nickel-based alloys in steam boilers. Sarver and Tanzosh (2003) reported an extensive literature review on the oxidation kinetics and the steam oxidation resistance of the candidate materials that could potentially be used in the USC coal power plants where the power plant could be operated up to 760°C and 38 MPa steam conditions. However, information on the suitable alloys for the use at the higher steam temperatures and pressures is actively sought. Currently, a number of relevant researches particularly for studying the oxidation of austenitic steel and nickel-based alloys are in progress and associated with the US USC Steam Boiler Tubing program as well as in European and Japanese programs. Results of these endeavors are expected to be available in a few upcoming years (Wright & Dooley, 2010). Besides that, to the author knowledge, no literature has been reported on estimating the oxide scale growth and development of thermo-mechanical stress-strain of candidate alloys' tube under the USC operation. Thus, for being in line with the ongoing programmes worldwide particularly in addressing steam-side oxidation of candidate alloys for USC operation, this work aims to propose the analytical approach that can be used to estimate the oxide scale growth and evaluate the thermo-mechanical stress-strain of austenitic steel and nickel-based alloys tubes under higher steam conditions in the USC power plant.

1.2 Objectives

The objectives of the present research work are:

1. To propose a mathematical model that can be used to assess the temperature distribution and thermo-mechanical stress-strain of multi-layered hollow cylinder tubes.
2. To develop a computational method for the estimation of oxide scale growth in the coal-fired boiler tubes.
3. To propose appropriate parameters utilizing a suitable scale failure model to determine the critical strain for oxide scale exfoliation.
4. To evaluate the effect of oxide scale growth and exfoliation on the temperature distribution and thermo-mechanical stress-strain of austenitic steel and nickel-based alloy boiler tubes.

1.3 Scope of project

In this project, a computational procedure to estimate the oxide scale growth is proposed. As it is commonly known that the oxide scale growth on the surface of the tubes may affect the stress-strain in the tubes, a new and simple analytical solution is derived to evaluate thermo-mechanical stress-strain in the boiler tube that contain oxide scales. The estimations obtained from the proposed method are validated with the field data from power plant and works reported in the literatures. Next, the computational method was then used to evaluate the effect of oxide scale growth on the temperature distribution, heat flux and the changes of thermo-mechanical stress-strain of the austenitic steel and nickel-based alloy superheater and reheater (SH/RH) tubes. Several models with different parameters are considered to investigate the factors that could affect the oxide scale growth on the boiler tubes. Besides that, the effects of oxide scales exfoliation and regrowth on the overall performance of the tubes are also studied.

1.4 Structure of Thesis

This thesis is organized based on the outline described below,

Chapter 1 gives the overall background of this study, presents the objectives of present work, scope of work and outlines the structure of thesis.

Chapter 2 started with the discussion on type of steam power plant with particular attention given to pulverized fuel fired power plant. Then following with the literature review on types of materials for boiler components in ultra-supercritical power plant, type of heat transfer mode involving in superheater and reheater tubes, high temperature oxidation of boiler tube materials, thermo-mechanical stresses of the cylindrical tube and the scale exfoliation and oxide scale failure diagram.

Chapter 3 discusses the methodology involving the heat transfer analysis of the boiler tube which starting with the priori assumptions, the heat transfer model and analytical solution to estimate the temperature distribution of multilayered tube such as for tube with oxide scales. A new and simple computational method to evaluate the thermo-mechanical stress-strain of multilayered hollow tube is presented. Subsequently, the iterative procedure for the prediction of scale growth and failure criteria of oxide scale based on through-scale cracking are elaborated. Lastly, the data and parameters used for simulation are also detailed in this chapter.

The results and discussion are presented in Chapter 4. Here, then results obtained from the proposed analytical solution are compared with finite element solution to ensure the analytical method is reliable. The proposed computational method to predict the scale growth is verified with the published data in the literature. In order to examine the limit of integrity of the oxide scales, the critical strain is obtained based on through scale crack, oxide scale failure diagram is plotted and verified with the laboratory results reported in literature. A systematic study is carried out to evaluate of oxide scale growth and

presumed exfoliation in austenitic and nickel based alloy tube of USC power plants under different assumed service conditions.

Finally, the conclusions and future work are presented in Chapter 5.

University of Malaya

CHAPTER 2: LITERATURE REVIEW

2.1 Introduction to steam power plant

Electricity is an important form of the energy and is essential for the operation of many industries and economic development. The large scale electricity generation is done in power plants where a source of primary energy is converted to electrical energy. The typical power plants used in the world include steam power plant, gas turbine power plant, nuclear power plant, hydro power plant, wind power plant, geothermal power plant and solar power plant (D. Zhang, 2013). Steam power plant (sometimes called thermal power plant) is the most dominant and widespread type of power generation. In operation, a steam power plant converts heat energy into electrical energy. Steam power plants are normally classified based on the type of fuels, such as coal-fired, gas-fired, oil-fired or biomass-fired thermal power plant (Speight, 2013).

Currently, about 40% of the world's electricity is generated by coal-fired power plants. The boiler used in coal fired power plants may be classified based on the mode of combustion as shown in Table 2.1.

Table 2.1: Types of Boilers and the mode of combustion (D. Zhang, 2013)

Type of boiler	Mode of combustion
Pulverized fuel fired boiler	Coal is milled into fine powders (usually in micron size) and blown into the combustion chamber and burn with the air and combustion gases. The fine pulverized fuel size provides highly efficient and rapid combustion.
Fluidized-bed boiler	The coal is crushed into small and fine particles, usually less than a few millimetres in size and fed into a column combustion chamber where it is burnt with air in a bed material (usually sand).
Stock fired boiler	The fuel is burnt in lumps, normally several to tens of centimetres in size, on a still or moving grate within the combustion chamber.

The operation types of the steam power plants can be classified based on the steam conditions as (Wheeldon & Shingledecker, 2013; D. Zhang, 2013):

- 1) Conventional subcritical power plant with the steam temperature ranging from 811K to 820K (538°C-547°C) and the pressure up to 17 MPa. The plant fuel to electricity conversion efficiency is expected to be around 38%.
- 2) Supercritical power plant with the steam temperature of around 870K (~590°C) and the pressure ranging from 22 to 24MPa (the expected efficiency of around 45%).
- 3) Ultra-supercritical (USC) and Advanced ultra-supercritical (A-USC) power

plant with steam temperature ranging from 870 to 1033K (590°C-760°C) and the pressure greater than 34 MPa (the efficiency is approaching 50%).

Despite the USC and A-USC plants are having the advantage of higher electricity conversion efficiency, the widespread implementation of the technology is governed by the stringent requirements of materials for construction, operation and the cost of maintenance (Starr, 2014). The following section presents the background and concerns related to materials used in the boiler for ultra-supercritical power plant.

2.2 Materials for boiler components in ultra-supercritical power plant

As mentioned in previous section, the ultra-supercritical boilers operate higher steam temperatures considerably in the range of 870-1033K. This is higher than the advanced supercritical pulverized coal boiler that operates temperatures around 870K. Though these boilers are capable to produce efficiencies in the range of 40% to 50%, the tubes materials are susceptible to oxidation which could lead to a failure. When the boiler tubes are exposed to high steam temperatures, a layer of oxide film may be formed on the steam-side wall of the tubes (Starr, 2014). As the steam temperature increases, the oxide scale layers grow more rapidly to greater thickness in a period of time. A thick oxide layer is known to have a low thermal conductivity and in turn it would insulate the tube material from the cooling fluid. As a result, it would pose higher corrosion and creep rates on the flue gas side. This is a paramount concern in the construction of USC boilers. Meanwhile, not many materials that are suitable for extreme operating conditions are available. It is mainly known due to inadequate oxidation/corrosion and creep resistance (Shibli, 2011). Significant researches and developments have been conducted in the past three decades to produce high-strength alloys for heavy thermal duties in boiler tube applications. In general, the materials are expected to have excellent properties for higher steam operations such as thermal conductivity, rupture strength, steam oxidation resistance and

creep resistance. To date, the developments are focused on three types of alloys, which are ferritic, austenitic and nickel based alloys (Abe, 2014b).

Masuyama (2001) has summarized the evolution of the steel alloys for boiler applications as illustrated in Figure 2.1. Significant improvements on the creep rupture strengths (from 35 MPa to 180 MPa at temperature of 600°C) have been made. The enhancements of the ferric steels were done by adding Molybdenum (Mo), Vanadium (V) and Niobium (Nb) to 9-12% Chromium (Cr) steels. Subsequently, the alloys were further improved by varying the Carbon (C), Nb and V contents. Partial substitution of Tungsten (W) for Mo was then applied, and later it was followed by the additions of more W and Cobalt (Co) in the current generation of high-strength steels.

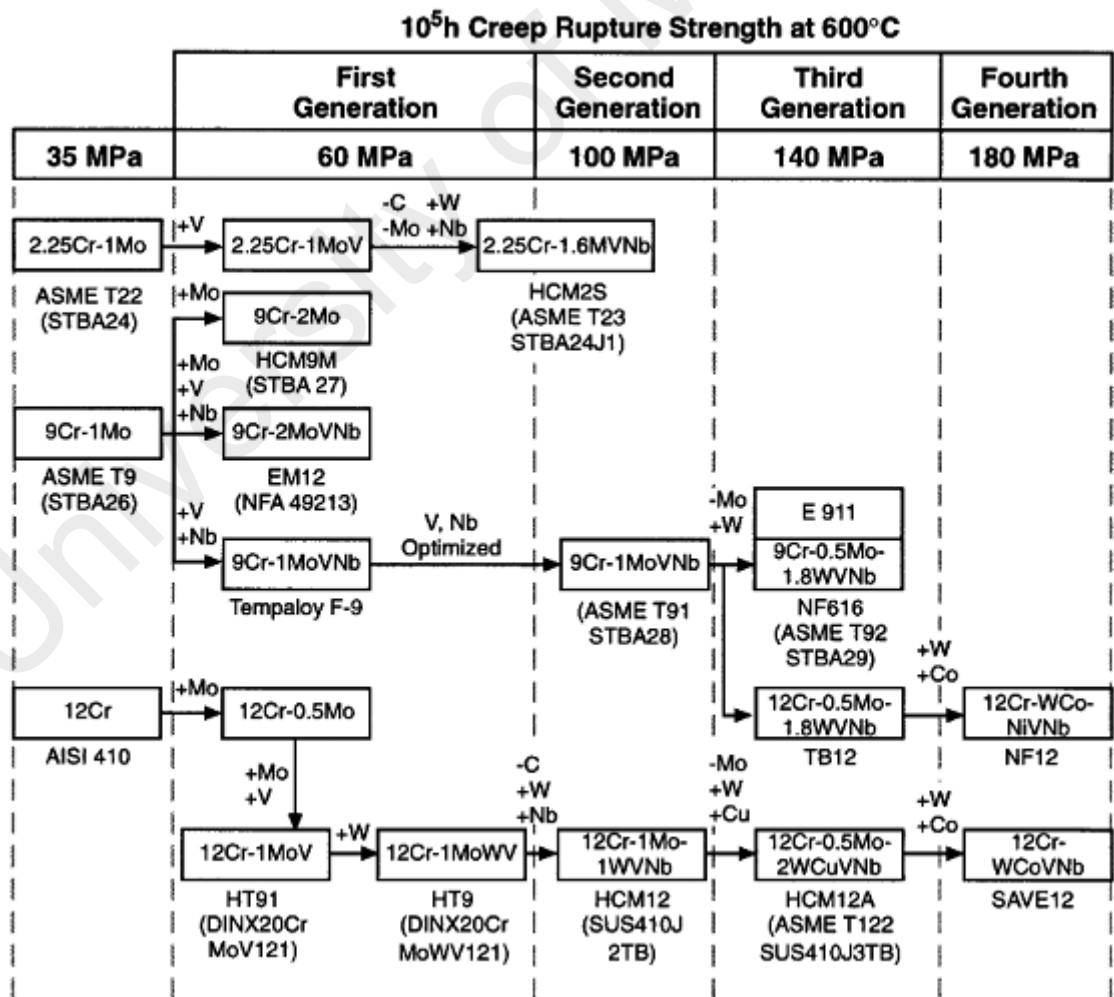


Figure 2.1: Evolution of ferric steels for boilers (Masuyama, 2001).

W, Mo and Co are considered to be primary solid-solution strengtheners. V and Nb strengthen the alloys by forming fine and coherent precipitates of the M(C,N)X-type carbonitrides in the ferritic matrix (where M denotes the metallic elements and X is for the carbon and nitrogen). V also precipitates as VN during the tempering process or during long-term creeping. The combination of about 0.25% V and 0.05% Nb was found to be more effective improvement (D. Zhang, 2013). Cr can strengthen the solid-solution and provides better corrosion and oxidation resistances. Nickel (Ni) improves the toughness with the offset of creep strength. The partial replacement of Ni by Cu helps to stabilize the creep strength. Carbon is needed for the formation of fine carbide precipitates, but the amount needs to be controlled for having a good weldability. On the other hand, the experimental analysis showed that Boron (B) can segregate the $M_{23}C_6$ -matrix interface and reduce the coarsening of $M_{23}C_6$. Boron assists the nucleation of VN, which in turn enhances the latent creep resistance (Garrison & Buck, 1999; Masuyama, 2011).

Viswanathan et al. (2006a) have extensively reported the role of Co in ferritic steels. Co is a good stabilizer for austenite and also able to regulate the tempering effect in martensitic steels. Besides that, Co can promote the nucleation of finer secondary carbides in tempering and also lower the coarsening of alloy carbides in secondary hardening steels. This is known that Co is not soluble in alloy carbides.

Ferritic steel developments are mostly developed for the use of thick section pipes and headers in the boiler system. Among the fully commercialized 9% Cr steels, the P91 steel is found to have the highest allowable stress and has been widely used as the material for the headers and steam pipes in USC plants with steam temperatures up to 593°C (D. Zhang, 2013). Alloy NF616 (P-92), that contains W (instead of Mo in P91), has even higher allowable stress and been used for steam temperatures up to 620°C. E911 is a European alloy that is known to have similar composition and capabilities to NF616. Beyond 620°C operation, the oxidation rate of the 9%Cr steels is considerably high, and

the use of 12%Cr steel and austenitic steels are safer for the operations (Purbolaksono et al., 2009).

Superheater and reheater (SH/RH) tubing applications often require good weldability, high creep strength, thermal fatigue strength, resistance to steamside oxidation and spallation and resistance to fireside corrosion/erosion. Ferritic/martensitic steels have been used extensively as tubing materials due to good thermal fatigue resistance and low cost. Unfortunately, these alloys can only be used up to the metal temperature of around 620°C due to the concern of insufficient creep strength and fireside corrosion resistance. On the other hand, tubing material with poor steamside oxidation resistance and exfoliation can cause multiple problems. Oxidation of tube wall can reduce the heat transfer of tubes and cause the increase of the metal temperature which could eventually lead to premature creep failures. Oxide scale exfoliation can potentially lead to tube blockages and the damage in the turbine blades. The use of high sulfur corrosive may result in an acute concern due to excessive corrosion in ferritic steels by liquid iron-alkali sulfates in the tube deposits (Shibli & Ford, 2014). Therefore, high strength ferritic stainless steels (SS) such as T91 are rarely used in certain countries, e.g. U.S. The T22 for the lower steam temperatures and austenitic steels such as SS304H or SS347 for the higher steam temperatures are widely used in practices. For steam temperature higher than 700°C, the use of Ni-base alloys is recommended (Viswanathan et al., 2006a).

In respect to the creep strength, T91 has a limited application to 565°C steam (metal 593°C), meanwhile NF616, HCM12A and E911 may be used for the operating temperature of around 593°C steam (metal 620°C). In practice, due to excellent properties of oxidation resistance, fireside corrosion and creep strength, the austenitic steels are chosen in the SH/RH tubing with steam temperature above 565°C (metal 593°C). Hence, there have been significant developments of the austenitic stainless steels since decades ago. In general, the austenitic steels are widely known to be into four categories: 15Cr,

18Cr, 20-25Cr and higher Cr stainless steels. The alloys were initially developed by adding Ti and Nb to stabilize corrosion properties of steels, then reducing the Ti and Nb contents (understabilizing) to promote better creep strength. Next, the addition of Cu into the alloy was purposely used to improve the strength by having fine precipitations (Sandström, 2014). Wright and Shingledecker (2015) called these enhanced austenitic alloys as advanced austenitic stainless steels. Then, the use of 0.2% nitrogen and W addition in the alloys was introduced for strengthening the solid solution. The development of the austenitic alloys is illustrated in Figure 2.2.

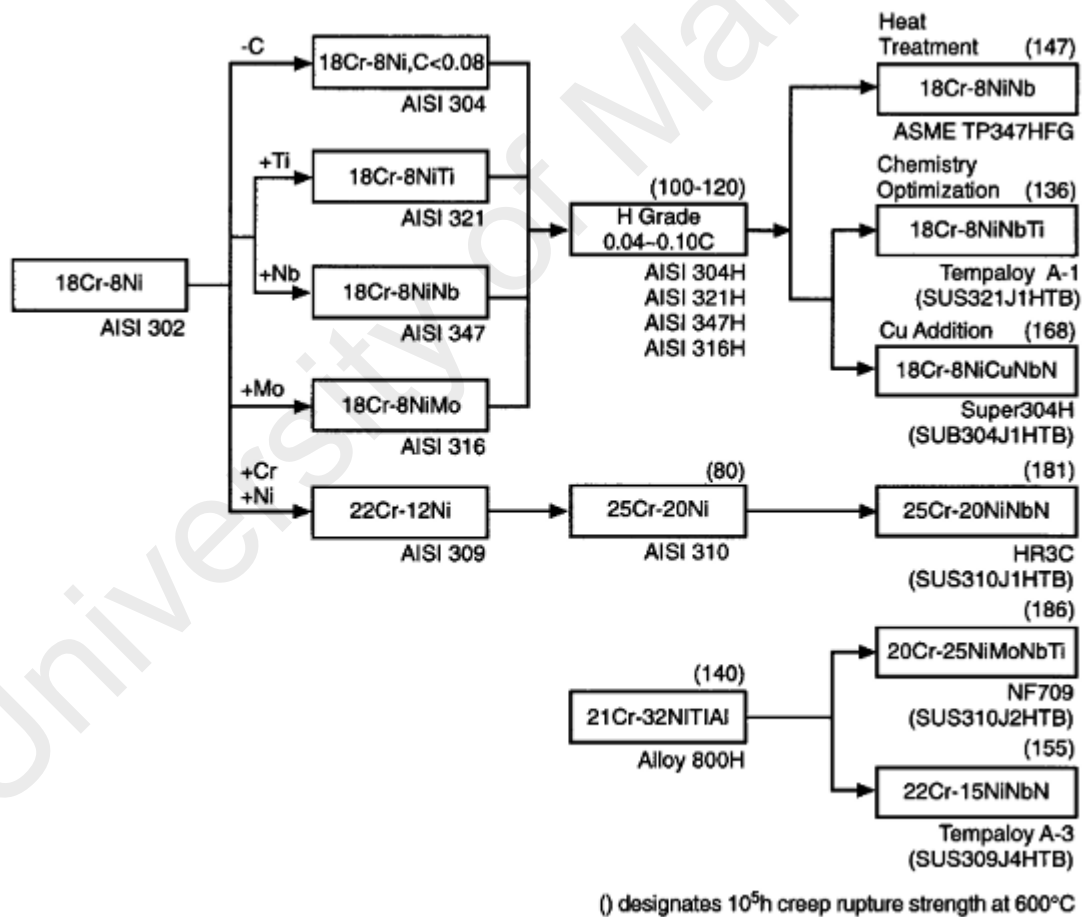


Figure 2.2: Developments of austenitic steels for boilers (Abe, 2014b)

The austenitic steels are able to withstand metal temperatures above 620°C, but the use is limited to 700°C (Wright & Shingledecker, 2015). For higher operating conditions in the USC, nickel-based alloys are known to be the suitable materials. According to Purbolaksono et al. (2009), the good mechanical and physical properties of nickel-based alloys allow the plant operators to run higher operational temperatures. Table 2.2 shows the popular commercial nickel-based materials with their compositions (for application in SH/RH tubing with metal temperatures of above 680°C). Holcomb et al. (2005) studied the steam oxidation of commercially available Ni-based alloys (Alloy 617, Alloy 230 and Alloy 740). They concluded that at 760°C the materials still exhibited slow oxidation rates and formation of protective oxides. This finding was in accordance with the conclusions made by Viswanathan et al. (2006b), where their tests confirmed the low oxidation rates of the nickel-based alloys under USC conditions. Unfortunately, the applications of Ni-based alloys require an economical consideration due to its high cost. However, the use of highly-cost nickel-based alloys remains a good option for the development of industrial size USC power plants (Ennis, 2014; Wright et al., 2004b). Experimental studies in high pressure testing rigs showed that Inconel 617 and Inconel 740 were considered to be the two most promising candidates for the new steam boilers (Baker & Gollihue, 2011; Viswanathan et al., 2002). According to Baker and Gollihue (2011), these two Inconels can potentially be used for the SH/RH tubing in the temperatures between 675-700°C. Further development of the nickel-based materials should aim to push their maximum temperature limit to 760°C and above.

Table 2.2: Types of Nickel Based Alloys (Wheeldon & Shingledecker, 2013).

Material	Average composition
IN617	22Cr-9Mo-10Co
Haynes 230	22Cr-14W-2Mo
IN740	25Cr-20Co-Al-Ti-Nb

Wheeldon and Shingledecker (2013) summarized the suitable materials that can satisfy the both economic manufacture and operation requirements for the superheater and reheater tubing as per stated in Table 2.3. However, they encouraged further relevant studies on the materials under boiler's steam environment $>700^{\circ}\text{C}$.

Table 2.3: Materials for different categories of supercritical boiler tubes (Wheeldon & Shingledecker, 2013)

Material	Average composition	Application ^a		
		SC	USC	A-USC
<i>Cr-Mo Steels</i>				
Gr. 22	2 1/4 Cr-Mo	√	-	-
<i>CSEF^b Steels</i>				
Gr. 91	9Cr-Mo-V-Nb	√	√	-
<i>Austenitic Stainless Steels</i>				
304H	18Cr-8Ni	√	-	-
347H	18Cr-10Ni-Nb	√	-	-
<i>Advanced Austenitic Stainless Steels</i>				
347HFG	18Cr-10Ni-Nb ^c	√	√	-
Super304H	18Cr-10Ni-Nb-Cu	√	√	-
NF709	20Cr-25Ni-Mo-Nb-B	-	√	√
HR3C	25Cr-20Ni-Nb	-	√	√
<i>Nickel-based alloys</i>				
IN617	22Cr-9Mo-10Co	-	-	√
Haynes230	22Cr-14W-2Mo	-	-	√
IN740	25Cr-20Co-Al-Ti-Nb	-	-	√

^aApplication insuperheater and reheater tubing of SC = Supercritical, USC= Ultra supercritical; A-USC = Advanced Ultra supercritical boilers.

^b CSEF = Creep-strength enhanced ferritic

^c Fine grained form of 347H obtained by thermo-mechanical processing.

2.3 Heat transfer in superheater and reheater tubes

Heat transfer is an important phenomenon to describe the thermal energy transfer mechanism in boiler. Prior to discussing the heat transfer in superheater and reheater tubes, a background of heating mechanism in the overall boiler system and components

is discussed. A boiler is a closed vessel for generating steam under pressure. It comprises of three important systems which are 1) feedwater system, 2) steam system, and 3) fuel system. The feedwater system supplies water to the boiler to meet the steam demand. The steam system collects and controls the steam produced in the boiler, usually the steam pressure is regulated by using valves and steam pressure gauges (Speight, 2013). The fuel system generates the required heat by burning the coal. In the furnace, high temperature flue gas is generated through the pulverized coal combustion, and is cooled when the heat is transferred to the working fluid (water/steam). The economizer, superheater and reheater have the same functions regardless of subcritical, supercritical or ultra-supercritical boiler. The economizer heats the feedwater before it enters the furnace, and the superheater and reheater heat the steam. It is noted that the water-cooled wall in the furnace is used to convert the feedwater into saturated steam in boilers, but this is not its only function in the latter, where it is also used to increase the steam temperature (Starr, 2014).

In the operation of superheater and reheater, heat is transferred from the hot flue gas through the steel tube to the cooler steam. Under the steady state condition, the temperature distribution in the tube is associated with the correlation between the thermal resistance and the heat transfer by radial conduction through the cylindrical tube wall and the convection at the inner and outer surface of tube as illustrated in Figure 2.3. In general, there are two major modes of heat transfer being involved in boiler tubes, namely conduction and convection.

2.3.1 Conduction

The heat conduction can be defined by the Fourier's law which describes the rate of heat transfer with respect to the time to be proportional to the negative temperature gradient and the area at the right angles to the gradient across of the heat flow. It can be

expressed as (Incropera, 2011):

$$Q = -kA \frac{dT}{dx} \quad \text{Eq. 2.1}$$

where Q is a heat flow (W) in direction x , k is the thermal conductivity of material (W/m/K), whereas the minus sign denotes the proper direction of decreasing temperature (it decreases with distance), A is area (m²), dT/dx is the temperature gradient in direction x (K/m).

The heat conduction on the boiler tube wall is illustrated in Figure 2.3, the heat transfer equation can be written as:

$$q_{conduction} = \frac{2\pi kL(T_1 - T_2)}{\ln\left(\frac{r_2}{r_1}\right)} \quad \text{Eq. 2.2}$$

where $q_{conduction}$ is heat transfer (W), T is the temperature (K), R is radius (m) and k is conduction coefficient (W/m/K), L is length (m).

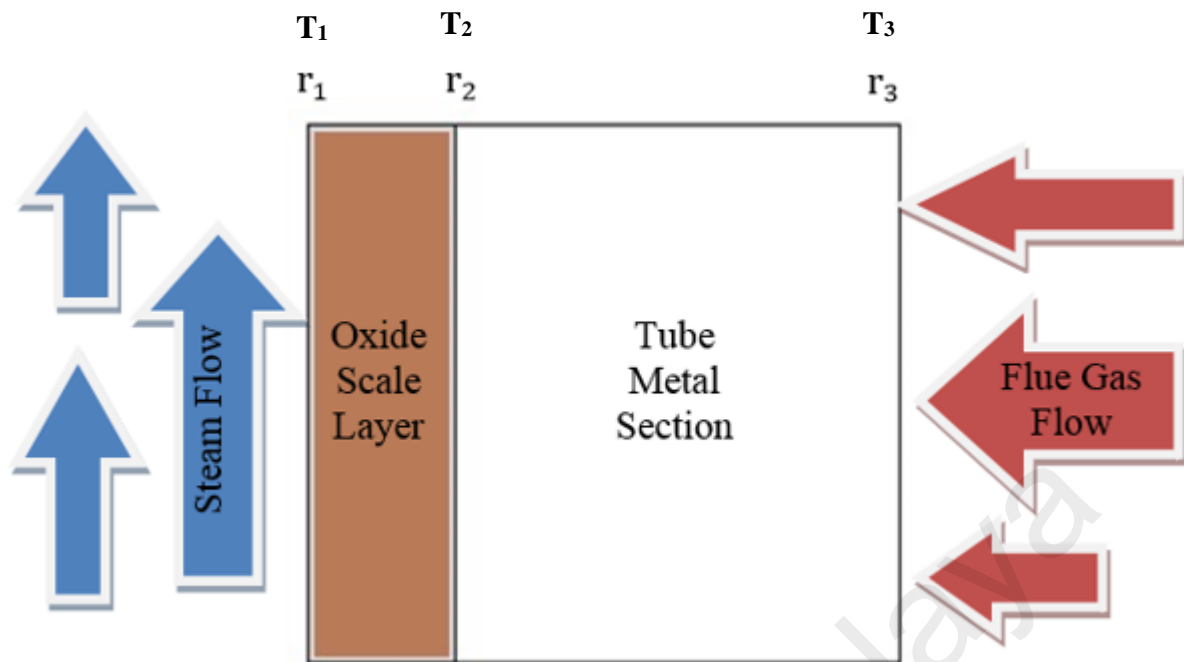


Figure 2.3: Schematic of 2-D axisymmetric tube model with oxide scale on the internal surface of the tube and the thermal resistance for each portion.

2.3.2 Convection

On the other hand, convection is a mode of the heat transfer that proceeds due to the bulk movement of a fluid; thus fluid mechanics is a crucial subject to be understood for studying the convection phenomena (Incropera, 2011). There are two types of convection:

- Forced when the flow of the fluid is caused by external driving force, which enhances the heat transfer
- Natural when a result of a thermally induced density gradient.

Considering the heat transfer from the wall to fluid, the mechanism of heat transfer at the wall would be conduction due to that liquid velocity being zero, but it changes to convection with distance from wall surface (Janna, 2009). The rate of heat transfer varies with the angle between the wall and temperature; the steeper the angle the larger the temperature difference. Convection is proportional to the temperature difference and is

written as the Newton's law of cooling (Incropera, 2011):

$$q_{conv} = h_c(T_3 - T_g) \quad \text{Eq. 2.3}$$

where h_c is the convection coefficient ($\text{W/m}^2/\text{K}$), T is temperature ($^{\circ}\text{C}$) whereby T_3 is temperature of the wall, T_g is temperature at infinitive distance perpendicular to the wall.

The conduction and convection equations will be used as part of the analytical equations to determine the temperature distributions of the tube with and without oxide scales.

2.4 High temperature oxidation of boiler tube materials

The corrosion behavior of materials in steam at a high temperature is of concern mainly due to the thickness/formation of the oxide films. With increasing temperature, the films form more rapidly and grow to a greater thickness in a given time, leading to three potential concerns. First, the wall loss of the pressure boundary can increase the stress and cause creep ruptures. Second, the increased insulation of the tube material from the cooling fluid by the low thermal conductivity of the oxide film leads to an increase in metal temperature; thus, in turn causes the increased corrosion and creep rates on the flue gas side. The third concern is that oxide scale spallation due stress/strain release from the thick oxides (Henry et al., 2007). The spalled material may lodge somewhere in the system, causing tube blockages, or it may be swept out with a working fluid and eventually enter the steam turbine, causing erosion damages on the steam path components. Loss of plant availability due to tube overheating resulting from oxide formation as well as subsequent exfoliation in austenitic and ferritic steel tubing have been reported for nearly 30 years (Holcomb, 2011; Wright et al., 2004a). In the United States (US), solid particle erosion (SPE) of turbine nozzles due to exfoliated scales has also been widely prevalent. Both problems have been on the increase in the US. Several

failures of T91 alloy tubing due to long term overheating have been reported. A combination of changes in operating practices, with extended running at near to full load, longer periods between scheduled maintenance, the trend towards higher steam temperatures and pressures and plant cycling, have contributed to mounting concerns over the increasing thickness of steam-side oxide scales. It is notable that long-term overheating failures due to flow restriction from exfoliated oxide scale is the second most important cause of boiler tube failures and reduced plant availability worldwide (Viswanathan et al., 2006b). Oxidation resistance of materials in steam is governed principally by alloy composition, temperature, and time. The following section discusses the oxidation characteristic based on the three main of materials used in superheater and reheater tubes.

2.4.1 Ferritic steels

The oxide scale formation on ferritic steel under the steam environment typically consists of double-layered structure that contains magnetite (Fe_3O_4) and hematite (Fe_2O_3). The outer layer is pure magnetite that is formed by columnar grain structure with pores. The inner layer usually has an equiaxed grain structure and finer, irregular porosity. Although hematite (Fe_2O_3) is expected to form on the outermost layer, it is not always present (Wright & Dooley, 2010). Usually, the hematite is found to be in discontinuous patches, and sometimes it is completely absent. A schematic of a typical scale structure formed on ferritic steel is showed in Figure 2.4.

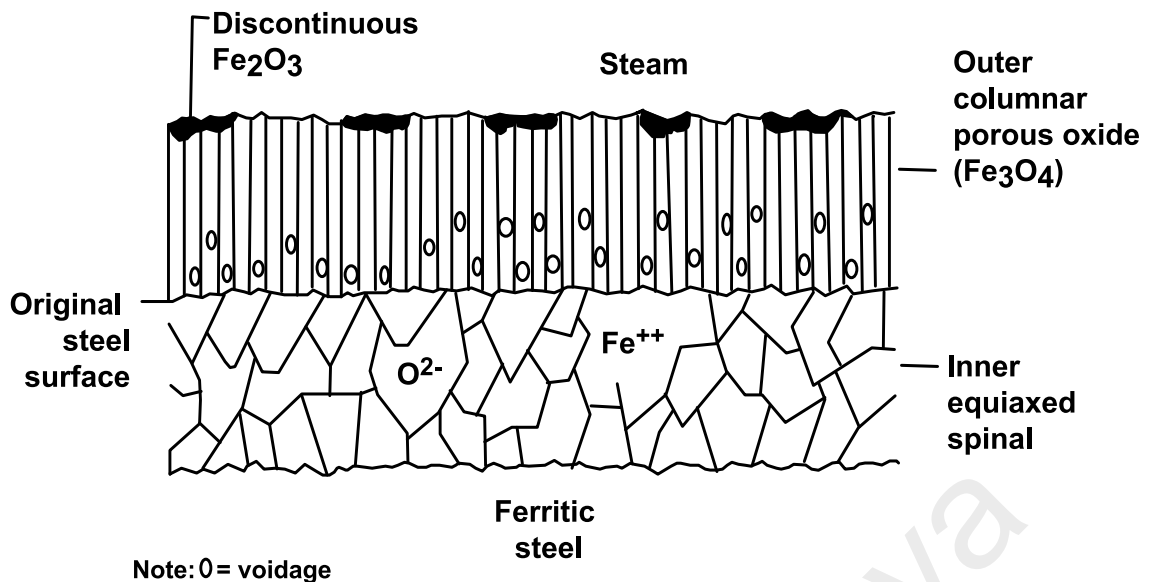


Figure 2.4: Typical scale structure formed on ferritic steel (Sabau et al., 2011).

At higher metal temperatures ($>580^\circ\text{C}$), an additional inner layer of wustite (FeO) may present such as shown in Figure 2.5(b) and (c). With increasing temperature, FeO formation increases. The FeO transformation temperature is variously cited as 570°C for carbon steel, 585°C for 1-1/4Cr1/2Mo steel, and 595°C , or 615°C , for 2-1/4Cr1Mo steel as summarized in Viswanathan et al. (2006b). Higher chromium alloys will have higher chromium traces in the inner oxide layer. In 9-12Cr alloys, the inner scale consists actually of mixed $\text{Fe}(\text{Fe},\text{Cr})_2\text{O}_4$ spinel with chromium content up to 46 % as indicated in Figure 2.5. Additionally, if the chromium content of the alloy is sufficient, a continuous layer of pure Cr_2O_3 may be detected. However, at the elevated temperatures the chromium content required to form a continuous scale of Cr_2O_3 is relatively high, ~ 25 wt% as seen in Figure 2.5. On lower chromium contents the Cr_2O_3 can be detected, but it does not form a continuous layer and thus does not provide sufficient protection at elevated temperature and pressure levels (Viswanathan et al., 2006b).

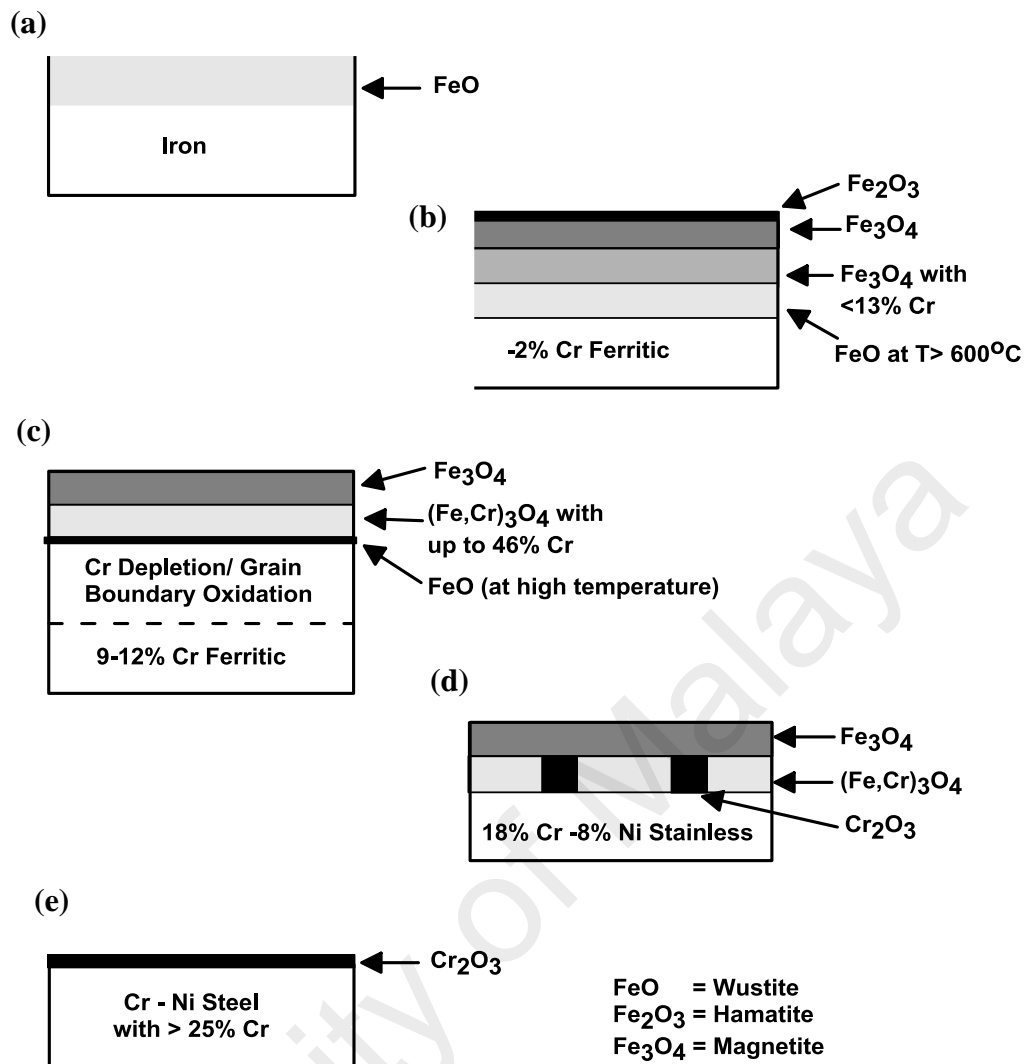


Figure 2.5: The oxide morphology of steel alloy formed at high temperature steam environment (Viswanathan et al., 2006b). a) Pure Iron, b) Ferritic steel with ~2%Cr content, c) Ferritic steel with 9-12 %Cr, d) Austenitic Steel with < 20% Cr, e) Ni-based alloy

In general, there is a consensus that the oxidation kinetics of ferritic boiler tubes occurs at a rate that can be represented by the following model (Wright & Dooley, 2010):

$$d_{ox}^2 = 2k_p t \quad \text{Eq. 2.4}$$

where d_{ox} is the oxide thickness and t is the time in hours. The temperature-dependence of the proportionality constant (k_p) typically is given by,

$$k_p = Ae^{-Q/RT} \quad \text{Eq. 2.5}$$

where Q is the activation energy for the rate-controlling process; T is the metal temperature (absolute); A is the Arrhenius constant, and R is the universal gas constant.

On the other hand, most laboratory studies tend to present the oxidation kinetics of alloy in steam with the following form,

$$\text{Scale thickness, } d_{ox} = (2k_p t)^{1/n} \text{ or } d_{ox} = kt^{1/n} \quad \text{Eq. 2.6}$$

where for ferritic tubing, n has been found to vary from 2 to 3 such as shown in Table 2.4 and is believed to be a function of time and temperature (Dewitte & Stubbe, 1986; Paterson et al., 1992; Paterson & Rettig, 1987; Rehn & Abplett, 1981). All the correlations, except those of Dewitte and Stubbe (1986), were developed based on data obtained from the as-received tubes/samples. The Dewitte & Stubbe correlations were derived from the data in air of the laboratory tests.

The oxidation kinetics for ferritic steels can be illustrated by the diagram shown in Figure 2.6. In this diagram, the line that divides linear kinetics from parabolic kinetics is not distinct because the factors other than temperature and Cr content (e.g., other alloying elements, other environmental factors, heat flux, etc.) play an important role in determining oxidation kinetics (Viswanathan et al., 2006b).

Table 2.4: General forms of oxide correlation for low alloy Cr-Mo steels.

General form of expression(s)	Approximate oxide-growth law
Rehn and Abplett (1981): Log x = A + B (LMP)	$x=k(t)^{1/3}$
Paterson and Rettig (1987) Log x = A + B (LMP)	$x = k(t)^{1/2.1 \text{ to } 1/2.6}$
Dewitte and Stubbe (1986): $x^2 = kt$	$x= k(t)^{1/2}$
Paterson et al. (1992): $x = k(T, A, P)^{1/2.6 \text{ to } 1/3.0}$	$x=kt^{1/2.6 \text{ to } 1/3.0}$

x, oxide scale thickness; t, time; k, oxide scale growth law rate constant;
A, B, C and D, coefficients; LMP, Larson-Miller parameter; T, Temperature;
P, bulk steam pressure. Note: Oxide scale thickness = 2.4 metal loss (penetration).

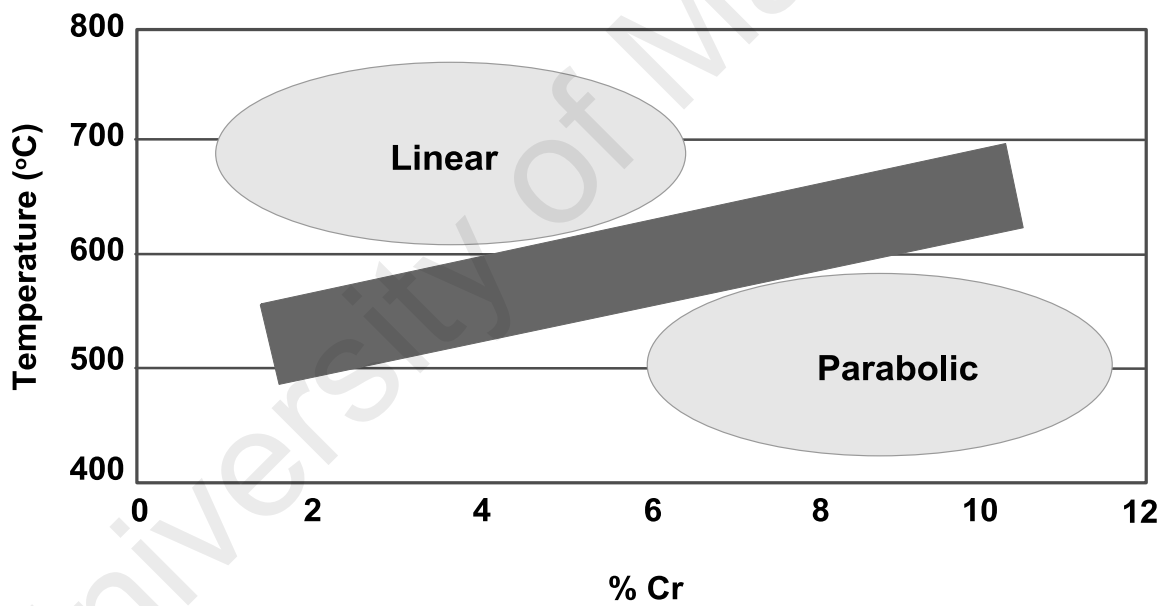


Figure 2.6: General trend of oxidation kinetics for ferritic steels as a function of %Cr and temperature (Viswanathan et al., 2006b).

2.4.2 Austenitic steels and Nickel-base alloys

According to Wright and Dooley (2010), the oxidation behavior of austenitic steels in steam can be divided into two distinct classes:

- 1) For the class of alloys with < 20 wt-% Cr and < 20 wt-% Ni and because of coarse-grained microstructure, the oxidation rates are significantly faster than equivalent fine-grained alloys. Besides that, these alloys do not form uniform chromium-rich oxide layer because of insufficient Cr content and Cr diffusivity.
- 2) Alloys with > 22 wt-% Cr and > 20 wt-% Ni, or fine-grained microstructure. Alloys oxidize at a slower rate than the coarse-grained and lower Cr and Ni alloys and able to form a continuous chromium-rich oxide layer.

Figure 2.7 shows the typical cross-sections of oxide scale morphologies detected on austenitic steels after being exposed to steam.

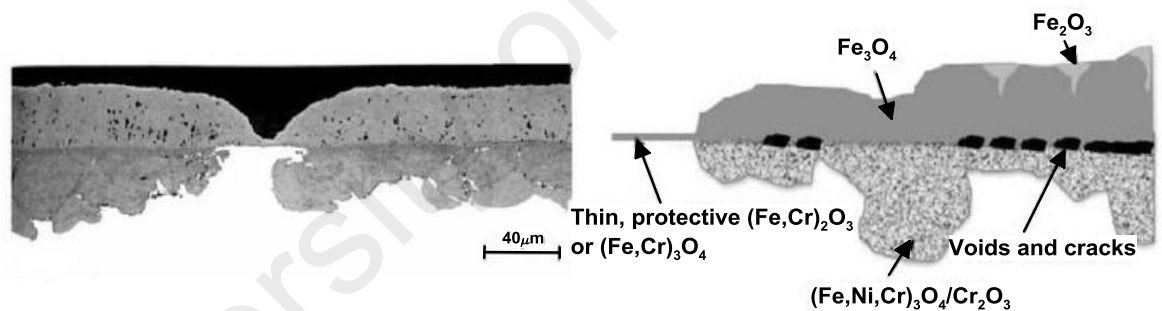


Figure 2.7: Typical oxide morphology formed on coarse-grained, 300-series (18Cr-12Ni) austenitic steels in steam. Cross section of scale formed on TP304H after 28000 hours at 538 °C and 5bar steam (left) and a schematic representation of oxide types (right) (Shingledecker et al., 2009).

The oxide layer formed on lower Cr and Ni steels consist predominantly of two layers: an outer layer of magnetite (Fe₃O₄) and inner layer of spinel (Fe-Cr) as shown in Figure 2.7. Similar to ferritic steels, sometimes an outer zone of hematite Fe₂O₃ may be detected. The oxide scales may become thicker with an increasing time and very often

the inner layer becomes increasingly non-uniform, and the outer magnetite layer becomes more porous. Various studies reported in Wright and Dooley (2010) indicated that initially the oxide scale consists of uniform layer of M_3O_4 (or sometime M_2O_3 oxides), where M is Fe and Cr. Normally the layer is enriched in Cr. After some time, a local breakdown of these initial scales begins through formation of nodules, which grow simultaneously inward and outward. The outward growing layer is pure magnetite, while the inward growing layer is a combination of Fe-Cr spinel, magnetite and other alloying elements, such as Mo, Mn and Ni that have similar crystal structure as magnetite. The inner Cr-rich layer grows by diffusing into the grain boundaries of Fe-Cr spinel and encircle the whole grain. Eventually, the grain body becomes depleted from chromium and further oxidization of the chromium-depleted grain bodies could essentially form the magnetite. This mechanism causes the inner oxide layer to consist of magnetite and Fe-Cr spinel, with Cr-rich spinel next to the alloy (Wright & Dooley, 2010).

The scale structures develop on higher Cr and Ni with fine-grained austenitic steels are similar to scale structures in lower Cr and Ni austenitic steels, except that the scales on higher Cr and Ni steels develop at considerably slower rate. The scale is double-layered with outer magnetite layer and inner homogenous Cr_2O_3 layer. For lower chromium content steel, there may be a layer of chromium rich Fe-Cr spinel in between the magnetite and Cr_2O_3 layers. These steels are having a sufficient Cr content that can improve the diffusion rate of Cr so that the Cr rich oxide layer is formed on the alloy-scale interface. In some cases, the oxide layer is very thin and it is difficult to distinguish the scale morphology. These oxide scales are however becoming thicker after being exposed to high temperature steam environment for longer time (Montgomery et al., 2012).

On the other hand, nickel-base alloys are frequently chosen due to their superior corrosion resistance to supercritical and high-temperature steam. The formation of oxide

scales on nickel-based alloys containing >16wt% chromium in steam up to 700°C are usually very thin and uniform in thickness (Viswanathan et al., 2006b). The layer consists of an outer layer, which is essentially the main chromia-based scale with some minor MnCr_2O_4 and Ni, depending on the alloying content. In some cases there may be some internal penetration beneath the external oxide scale. Internal penetration may range from few discrete precipitates to high population of internal precipitates and penetration along alloy grain boundaries. Usually this type of internal penetration is particularly detected on alloys containing Al and Ti (Shingledecker et al., 2009; Wright & Dooley, 2010). A schematic of oxide structure developed on nickel-based alloys in steam is presented in Figure 2.8.

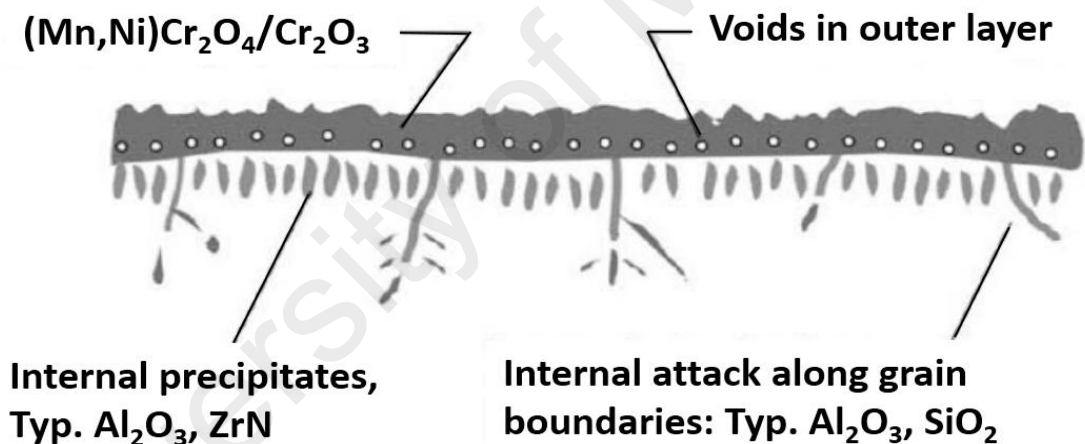


Figure 2.8: A schematic representation of oxide scale morphology formed on nickel-based alloys exposed to steam (Shingledecker et al., 2009).

In terms of the oxidation kinetics to predict the scale growth, several literatures have reported to use the parabolic oxidation rate law equation (Eq. 2.6) for austenitic steel. The activation energy (Q) and Arrhenius constant (A) have been detailed in the Sabau et al. (2011) and Matsuo et al. (2005), however, the estimation works have not been verified with field data. On the other hand, to the author knowledge, no estimation work for scale growth of Ni-based alloy tube has been reported in the existing literature.

Thus, the proposed estimation procedure and the systemic simulation studies in this research may provide a general guide and implication on the effects of oxide scale formations in austenitic steel and Ni-based alloy tube used in ultra-supercritical power plants.

2.4.3 Correlation of scale thickness with the Larson-Miller parameter

The correlation of scale thickness with Larson-Miller parameter (LMP) for ferritic steel with 1-3% chromium was reported by Rehn and Abblett (1981). Viswanathan et al. (2006b) briefly mentioned the data of scale thickness versus Larson-Miller parameter for all three classes of materials that are suitable for uses in boiler tubes, namely, ferritic steel, austenitic steel and nickel-based alloys. The data as shown in Figure 2.9 were produced by the National Physical Laboratory, United Kingdom (Osgerby & Fry, 2003). By comparing with the field data report in literature such as Fleming et al. (2000), Matsuo et al. (2005), Sato et al. (2005), and Nishiyama et al. (2003), it was found that all field data fall within the scatter bands by different classes of materials cited in National Physical Laboratory, United Kingdom (Osgerby & Fry, 2003).

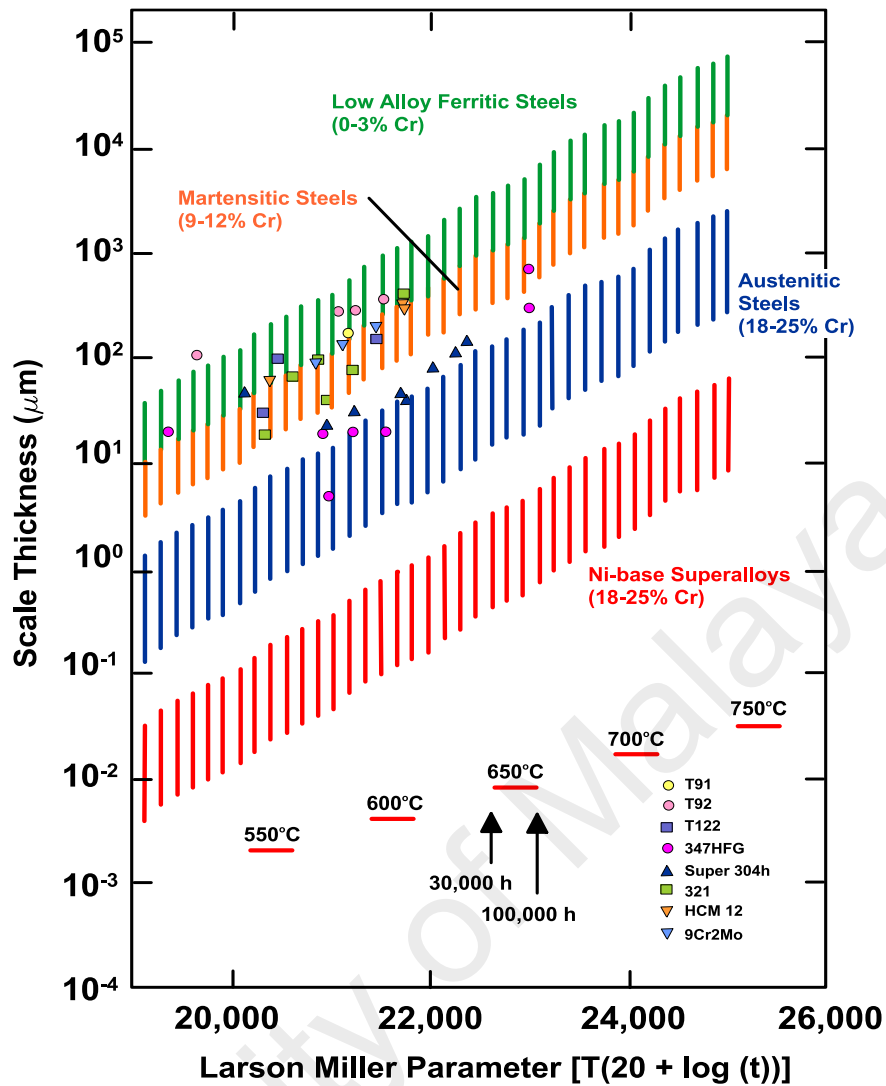


Figure 2.9: Scale thickness increase with temperature and time expressed in terms of Larson Miller parameter (Osgerby & Fry, 2003).

2.5 Thermo-mechanical stress-strain of the cylindrical tube

When the oxide scales on the inner surface of tubes become thicker, it would pose a reduction in the ability to accommodate stresses resulting from the growth process (Henry et al., 2007). Accommodating these stresses leads to modification of scale morphology, development of flaws and eventual exfoliation of the oxide from the tube surface into the steam flow (Tonti, 2014). As mentioned in the earlier section, the oxide scale exfoliation could lead to undesired damage and break down of the boiler operation. Thus, to anticipate the occurrence of scale exfoliation, it is necessary to develop a

quantitative understanding of the stress-strain development in the tube, particularly when it is subjected to high temperature and pressure.

The stress-strain relationship of hollow tube with variation of the radial temperatures can be expressed as follows (Eslami et al., 2013),

$$\epsilon_{rr} = \frac{1}{E} [\sigma_{rr} - \nu(\sigma_{\theta\theta} + \sigma_{zz})] + \alpha\theta \quad \text{Eq. 2.7}$$

$$\epsilon_{\theta\theta} = \frac{1}{E} [\sigma_{\theta\theta} - \nu(\sigma_{rr} + \sigma_{zz})] + \alpha\theta \quad \text{Eq. 2.8}$$

$$\theta = T - T_r \quad \text{Eq. 2.9}$$

where ϵ_{rr} is radial strain, $\epsilon_{\theta\theta}$ is hoop strain, E is young modulus, ν is Poisson's ratio, α is coefficient of thermal expansion, σ_{rr} is radial stress, $\sigma_{\theta\theta}$ is hoop stress, σ_{zz} is axial stress, θ radial temperature, T is average temperature and T_r being the reference temperature. Assuming plain strain condition, $\epsilon_{zz} = \epsilon_{rz} = \epsilon_{\theta z} = 0$, where ϵ_{zz} is axial strain and $\epsilon_{rz}, \epsilon_{\theta z}$ are shear strains.

The radial displacement can be expressed as,

$$u_r(r) = \frac{1+\nu}{1-\nu} \frac{\alpha}{r} \int_{r_{i-1}}^r \theta r dr + Cr + \frac{D}{r} \quad \text{Eq. 2.10}$$

where r is the radial distance, C and D are the integration constants. Using the radial displacement, strain-displacement relation can be known as,

$$\epsilon_{rr} = \frac{du_r}{dr} \text{ and } \epsilon_{\theta\theta} = \frac{u_r}{r} \quad \text{Eq. 2.11}$$

Thus, the equations for the radial and hoop stresses can be written in terms of displacements as follows (Eslami et al., 2013),

$$\sigma_{rr} = \frac{E}{(1+\nu_i)(1-2\nu_i)} \left[(1-\nu) \frac{du_r}{dr} + \nu \frac{u_r}{r} - (1+\nu)\alpha\theta \right] \quad \text{Eq. 2.12}$$

$$\sigma_{\phi\phi} = \frac{E}{(1+\nu)(1-2\nu)} \left[(1-\nu) \frac{u_r}{r} + \nu \frac{du_r}{dr} - (1+\nu)\alpha\theta \right] \quad \text{Eq. 2.13}$$

$$\sigma_{zz} = \nu(\sigma_{rr} + \sigma_{\phi\phi}) - E\alpha\theta \quad \text{Eq. 2.14}$$

Equations Eq. 2.7 - Eq. 2.14 are only suitable for evaluating the thermo-mechanical stresses and strains of boiler tube without oxide scale. As oxide scale formation on the internal and external surface of the tubes could affect the overall stress distribution of the tube, an analytical solution for evaluating the thermo-mechanical stress-strain of multilayer cylinder tube is required. Thus, in this present work, a new mathematical model has been derived based on the fundamental equations to solve the thermo-mechanical stress-strain of multilayer cylinder tube.

2.6 Scale exfoliation and the oxide scale failure diagram

As mentioned in earlier discussion, exfoliation of oxide scales is primarily associated with the stress and strain developed as the oxide grown. The scale structure which commonly contained of voids can affect the ability of the scales to withstand the strains. In many instances, the exfoliation occurs near the metal-scale interface or at the interface between the outer and inner part of the scale (Viswanathan et al., 2006a). Armitt et al. (1978) introduced an exfoliation mechanism by relating the accumulated elastic strain in oxide scales to the scale thickness and plotted the relation into a map to estimate the tendencies of scale damage and exfoliation. They presented the concept of oxide scale failure diagram (also called Armitt diagram) such as shown in Figure 2.10 to define the regimes in which various failure modes as a function of strain (in the oxide) and oxide thickness. In the oxide scale failure diagram, the regime of scale integrity (without

exfoliation) narrows rapidly with increasing scale thickness, this simply implied that the amount of total elastic strain can be accommodated is decreasing as the scale thickness increases. Although this concept has been reported working well in certain material system such as oxide grown on 2.25Cr1Mo steel, but it may not produce a desire estimation in other material system (Quadackers et al., 2005).

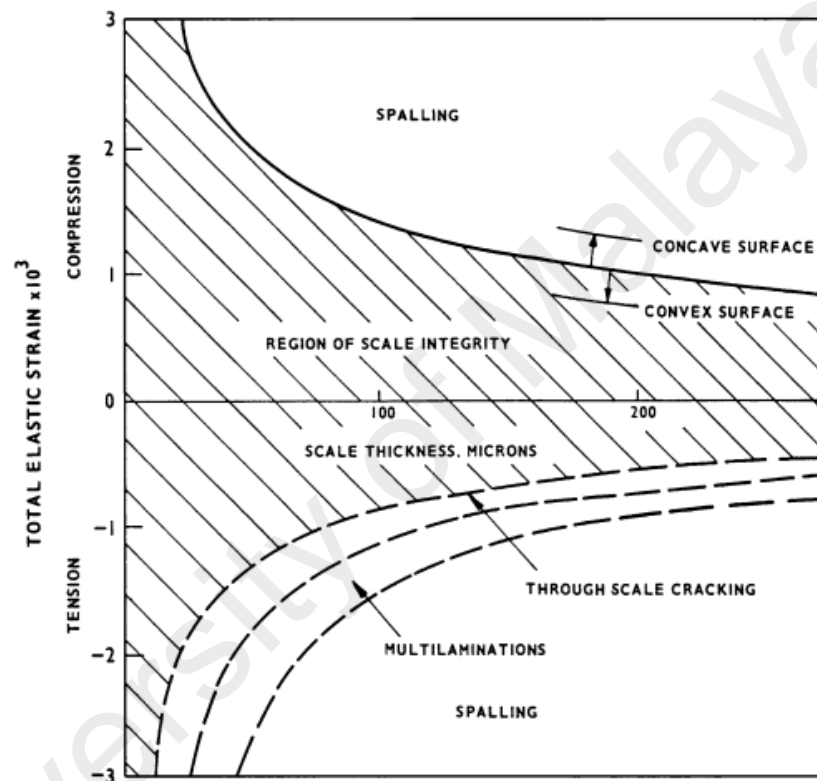


Figure 2.10: The oxide scale failure diagram (OSFD)/ Armitt diagram (Armitt et al., 1978)

Furthermore, the shortcoming of this Armitt diagram has been reported in Schütze et al. (2010) whereby the role of physical defects such as porosity and microcrack have not been directly taken into account via the fracture energy which used to determine the critical failure strain. Figure 2.11 shows a more comprehensive approach called Advance Oxide Scale Failure Diagram (A-OSFD) which was introduced by Schütze et al. (2010). They considered a more comprehensive operational parameter (ω) which summarized all

contributing factors such as physical defect size, interface roughness, scale thickness, Young's modulus, fracture toughness and etc., that could affect the critical failure strain. Rudolphi and Schütze (2013) validated the A-OSFD using experimental results and data from existing literatures for various material systems such as nickel oxide, titanium oxide and iron oxide. Nevertheless, the study related to the iron oxide was primarily focusing on FeO. Since the magnetite (Fe_3O_4) and chromium oxide (Cr_2O_3) are the interested oxide system in this research, the validations for the respective A-OSFD are required and will be carried out in this work.

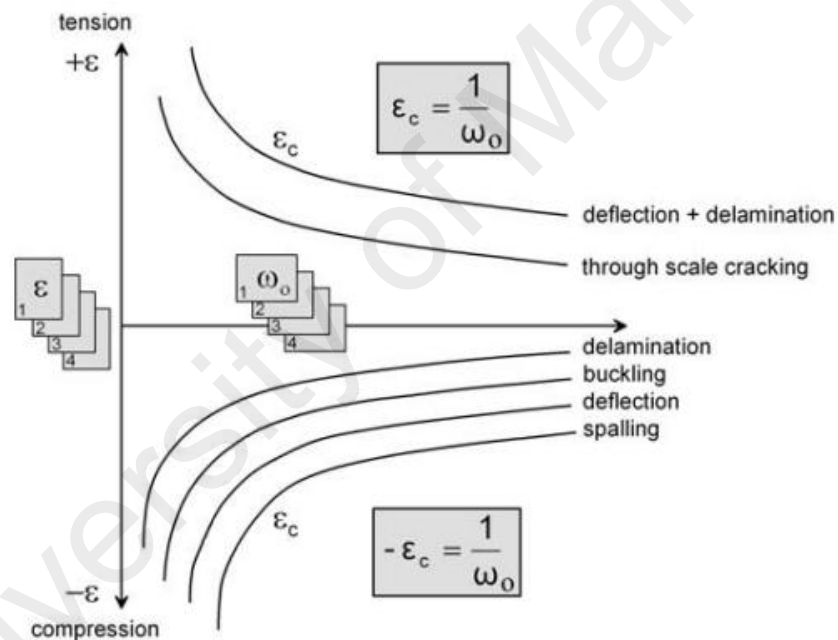


Figure 2.11: Schematic of an advanced oxide scale failure diagram (Schütze et al., 2010).

2.7 Summary

The future energy demand and higher electricity efficiency have encouraged the power generation operators to implement the USC technology. However, the technology is facing various challenges such as the maintenance costs, material requirements for construction and operation under extreme environment. On the other hand, the

superheater and reheater tubes that operate high steam conditions in the USC plants would be exposed to the risk of steam oxidation resulting in the formation of oxide scale on the tube walls. The formation of the oxide layer can hinder the heat transfer of the tube to the cooling fluid, causing the elevation of the metal temperature. Thus, higher risks of the increased corrosion rate, thinning issues and creep rates on the flue gas side are imminent. In addition, the oxide scale exfoliations due to stress/strain accumulation and the mismatch of the thermal expansion coefficients between the scales and tube material are well known events. The spalls may be carried in the steam flow causing a blockage in the tube-line and the erosion damage of the turbine components. Thus, upon either undesirable event, an unscheduled shutdown of the power plant is expected and the loss of massive revenue is a big consequence.

One of the important challenges in the successful operation of a USC boiler is how to control the steam-side oxidation. However, there is currently insufficient information on the steam-side oxidation and temperature limits of candidate alloys (the austenitic steels or nickel based alloys). Thus this concern has motivated European countries, Japan and US to run major programmes associated with the studies on the steam oxidation of the alloys for USC operation.

On the other that, it is worth pointing out that no literature has been reported on estimating the oxide scale growth and thermo-mechanical stress-strain of austenitic steel and nickel-based alloy tubes under the USC operation. Therefore, to be in line with those ongoing programmes, this work develops the analytical approach for estimating the oxide scale growth and evaluating the thermo-mechanical stress-strain of austenitic steel and nickel-based alloys tubes under higher steam conditions in the SH/RH tubing. Next chapter presents the proposed methodology and the relevant parameters and data that are used to carry out the analyses in this work.

CHAPTER 3: METHODOLOGY

3.1 Introduction

In this chapter, a simple and efficient analytical solutions are proposed to estimate the scale growth, temperature distribution and the thermo-mechanical stress-strain of boiler tubes used in ultra-supercritical power plant. A number of properties, parameters and data used for analysis are also presented in this chapter.

3.2 Heat Conduction Equation and Thermo-mechanical Stress-strain in Multilayered Tube

3.2.1 Priors assumptions

The priori assumptions used in the heat transfer analysis are stated as follows:

- the heat transfer is in a steady state condition;
- the steam flow, steam temperature, steam pressure and flue gas temperature are constant;
- heat transfers on the inner and outer surface are assumed to be forced convection due to turbulent flow and flue gas cross flow;
- the stress-strain equations are derived based on the generalized plane strain condition;
- all the layers for the multilayered tube are perfectly bonded together and without sliding.

3.2.2 Geometry and material properties

A tube with n -layers is subjected to steam temperatures and pressures on the inner surface (r_0) and outer surface (r_n) as shown in Figure 3.1. Let r_i be the outer radius of i -th layer. The notations for the material properties of i -th layer, i.e. the elastic modulus E_i , Poisson's ratio ν_i , the thermal conductivity k_i , and the coefficient of thermal expansion α_i , are depicted in Figure 3.1.

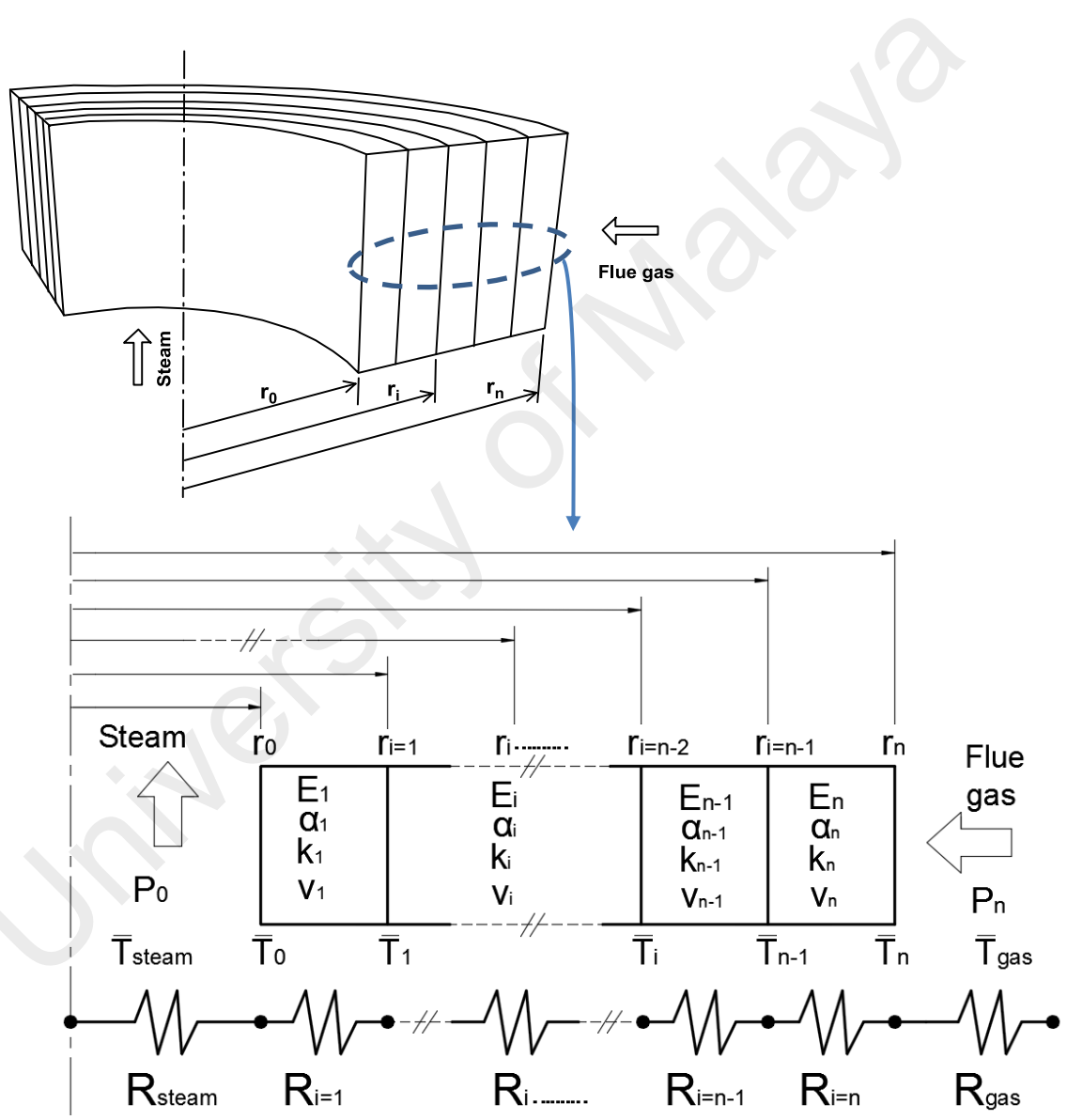


Figure 3.1: Multi-layered tube that is subjected to with steam on the inner surface and flue gas on the outer surface.

3.2.3 Boundary conditions

On the inner surface of the tube, the boundary conditions are prescribed as follow,

$$q''_{steam} = q''_0(r_0)$$

$$-h_s(\bar{T}_0 - \bar{T}_{steam}) = -k_1 \left. \frac{dT_1(r)}{dr} \right|_{r=r_0} \quad \text{Eq. 3.1}$$

$$\sigma_{rr,1}(r_0) = -p_0 \quad \text{Eq. 3.2}$$

where q''_{steam} and $q''_0(r_0)$ are, respectively, the heat flux of steam and heat flux on the inner surface of 1st layer; \bar{T}_0 and \bar{T}_{steam} are, respectively, the temperature on the inner surface and steam; h_s and k_1 are, respectively, denote the coefficient of convection of steam and thermal conductivity of 1st layer; p_0 and $\sigma_{rr,1}(r_0)$, respectively, indicate the pressure and radial stress on the inner surface of 1st layer.

Similarly, the boundary conditions on the outer surface can be written as

$$q''_n(r_n) = q''_{fluegas}$$

$$-k_n \left. \frac{dT_n(r)}{dr} \right|_{r=r_n} = h_g(\bar{T}_n - \bar{T}_{gas}) \quad \text{Eq. 3.3}$$

$$\sigma_{rr,n}(r_n) = -p_n \quad \text{Eq. 3.4}$$

where $q''_{fluegas}$ and $q''_n(r_n)$ are, respectively, the heat flux of flue gas and heat flux on the outer surface of last layer; \bar{T}_n and \bar{T}_{gas} are, respectively, the temperature on the outer and flue gas; h_g and k_n are, respectively, the coefficient of convection of flue gas and thermal conductivity of last layer; p_n and $\sigma_{rr,n}(r_n)$, respectively, represent the pressure and radial stress on the outer surface of last layer.

The temperature, heat flux, radial stress and displacement at each interface of the layers i and $i+1$ can be expressed, respectively, as

$$T_i(r_i) = T_{i+1}(r_i) \quad \text{Eq. 3.5}$$

$$q_i''(r_i) = q_{i+1}''(r_i) \quad \text{Eq. 3.6}$$

$$\sigma_{rr,i}(r_i) = \sigma_{rr,i+1}(r_i) \quad \text{Eq. 3.7}$$

$$u_{r,i}(r_i) = u_{r,i+1}(r_i) \quad \text{Eq. 3.8}$$

3.2.4 Heat conduction equations

The governing equation of heat conduction in the cylindrical coordinates is generally written as (Eslami et al., 2013),

$$k_i \left(\frac{\partial^2 T_i(r)}{\partial r^2} + \frac{1}{r} \frac{\partial T_i(r)}{\partial r} + \frac{1}{r^2} \frac{\partial^2 T_i(\theta)}{\partial \theta^2} + \frac{\partial^2 T_i(z)}{\partial z^2} \right) + R_i = \rho_i c_i \frac{\partial T_i(t)}{\partial t} \quad \text{Eq. 3.9}$$

where k , R , ρ and c , respectively, denote the thermal conductivity, the internal heat generated per unit volume, the mass density and the specific heat. In the absence of heat generation, the governing equation for one-dimensional steady state problem can be simplified as (Eslami et al., 2013),

$$\frac{\partial}{\partial r} \left(r \frac{\partial T_i(r)}{\partial r} \right) = 0 \quad \text{Eq. 3.10}$$

Integrating Eq. 3.10 yields

$$T_i(r) = A_i + B_i \ln r \quad \text{Eq. 3.11}$$

To estimate the temperature distribution across the wall thickness of the hollow cylinder, the constants A_i and B_i may be determined by substituting Eq. 3.11 into Eq. 3.5, it gives

$$A_i + B_i \ln r_i = A_{i+1} + B_{i+1} \ln r_i \quad \text{Eq. 3.12}$$

Similarly, utilizing heat flux equation of Eq. 3.6 leads to another relation as

$$-k_i \left(\frac{B_i}{r_i} \right) = -k_{i+1} \left(\frac{B_{i+1}}{r_i} \right) \quad \text{Eq. 3.13}$$

Eq. 3.12 and Eq. 3.13 can be rewritten as

$$A_{i+1} = A_i + B_i \ln r_i \left(1 - \frac{k_i}{k_{i+1}} \right) \quad \text{Eq. 3.14}$$

$$B_{i+1} = B_i \left(\frac{k_i}{k_{i+1}} \right) \quad \text{Eq. 3.15}$$

Thus, the temperatures at the interface of two adjacent layers can be defined as

$$A_i + B_i \ln r_{i-1} = \bar{T}_{i-1} \quad \text{Eq. 3.16}$$

$$A_{i+1} + B_{i+1} \ln r_{i+1} = \bar{T}_{i+1} \quad \text{Eq. 3.17}$$

Substituting Eq. 3.14 and Eq. 3.15 into Eq. 3.16 and Eq. 3.17 gives

$$A_i = \frac{\bar{T}_{i+1} x_i - \bar{T}_{i-1} y_i}{x_i - y_i} \quad \text{Eq. 3.18}$$

$$B_i = \frac{x_i (\bar{T}_{i-1} - \bar{T}_{i+1})}{\ln r_{i-1} (x_i - y_i)} \quad \text{Eq. 3.19}$$

where $x_i = \delta_i \delta_{i+1}$, $y_i = \delta_{i+1} - \frac{k_i}{k_{i+1}} (\delta_{i+1} - 1)$ and $\delta_i = \frac{\ln r_{i-1}}{\ln r_i}$

The outer temperature of the layer i can be then written as

$$T_i(r_i) = A_i + B_i \ln r_i = \bar{T}_i \quad \text{Eq. 3.20}$$

Substituting Eq. 3.18 and Eq. 3.19 into Eq. 3.20 results in a relationship of the temperature

at the interface as

$$\bar{T}_{i+1} = \frac{\bar{T}_{i-1}(\delta_i y_i - x_i) + \bar{T}_i \delta_i (x_i - y_i)}{x_i (\delta_i - 1)} \quad \text{Eq. 3.21}$$

Making use of Eq. 3.21, the Eq. 3.18 and Eq. 3.19 can be written in terms of the temperatures on the inner and outer surfaces of layer i as

$$A_i = \frac{\bar{T}_i \delta_i - \bar{T}_{i-1}}{\delta_{i-1}} \quad \text{Eq. 3.22}$$

$$B_i = \frac{(\bar{T}_{i-1} - \bar{T}_i)}{\ln(r_i/r_{i-1})} \quad \text{Eq. 3.23}$$

To calculate A_i and B_i in Eq. 3.22 and Eq. 3.23, it is necessary to find \bar{T}_0 , \bar{T}_n and \bar{T}_i . By applying Fourier's law to Eq. 3.11,

$$q_i''(r_i) = -k_i \frac{dT_i}{dr} = -k_i \frac{B_i}{r_i} = \frac{k_i (\bar{T}_{i-1} - \bar{T}_i)}{r_i \ln(r_i/r_{i-1})} \quad \text{Eq. 3.24}$$

The area across which the heat flow is

$$A_i = 2\pi r_i L \quad \text{Eq. 3.25}$$

Therefore, the heat flow can be written as

$$Q = q_i'' A_i = \frac{2\pi k_i L (\bar{T}_{i-1} - \bar{T}_i)}{\ln(r_i/r_{i-1})} \quad \text{Eq. 3.26}$$

To find the heat flow (Q), it is necessary to construct the expressions of thermal resistance through each portion of the heat flow as illustrated in Figure 3.1,

$$\text{Steam side, } R_{steam} = \frac{1}{h_s A_0} = \frac{1}{2\pi r_0 L h_s} \quad \text{Eq. 3.27}$$

$$\text{multilayered tube, } R_{tube} = \sum_{i=1}^n \frac{\ln(r_i/r_{i-1})}{2\pi k_i L} \quad \text{Eq. 3.28}$$

$$\text{gas side, } R_{gas} = \frac{1}{h_g A_n} = \frac{1}{2\pi r_n L h_g} \quad \text{Eq. 3.29}$$

Thus, the heat flow can be expressed as,

$$Q = \frac{\bar{T}_{gas} - \bar{T}_{steam}}{R_{steam} + R_{tube} + R_{gas}} \quad \text{Eq. 3.30}$$

By knowing the inner boundary condition stated in Eq. 3.1, the temperature at the inner surface of the tube can be found by using the following equation,

$$\frac{Q}{A_0} = h_s(\bar{T}_0 - \bar{T}_{steam}) \Rightarrow \bar{T}_0 = \bar{T}_{steam} + \frac{Q}{2\pi r_0 L h_s} \quad \text{Eq. 3.31}$$

T_i and T_n can also be found by using Eq. 3.26

$$\bar{T}_i = \bar{T}_{i-1} - \frac{Q \ln(r_i/r_{i-1})}{2\pi k_i L} \quad \text{Eq. 3.32}$$

where $i= 1,2,3 \dots n$.

3.2.5 Displacements and stress-strain relations

It is considered that the hollow cylinder shown in Figure 3.1 is under the generalized plane strain condition and has variation of the radial temperatures of $\theta_i = T_i - T_r$ with T_r being the reference temperature. The strain-displacement relation has been known as (Hetnarski & Eslami, 2009),

$$\epsilon_{rr,i} = \frac{du_{r,i}}{dr} \quad \text{Eq. 3.33}$$

$$\epsilon_{\theta\theta,i} = \frac{u_{r,i}}{r} \quad \text{Eq. 3.34}$$

$$\epsilon_{zz,i} = \frac{du_z}{dz} = C_z \quad \text{Eq. 3.35}$$

$$\epsilon_{zz,i} = \epsilon_{rz,i} = \epsilon_{\theta z,i} = 0 \quad \text{Eq. 3.36}$$

Thus, the stress-strain relations for i -th layer can be expressed as (Hetnarski & Eslami, 2009),

$$\sigma_{rr,i} = \frac{E_i}{(1+v_i)(1-2v_i)} [(1-v_i)\epsilon_{rr,i} + v_i\epsilon_{\theta\theta,i} - (1+v_i)\alpha_i\theta_i] \quad \text{Eq. 3.37}$$

$$\sigma_{\theta\theta,i} = \frac{E_i}{(1+v_i)(1-2v_i)} [(1-v_i)\epsilon_{\theta\theta,i} + v_i\epsilon_{rr,i} - (1+v_i)\alpha_i\theta_i] \quad \text{Eq. 3.38}$$

$$\sigma_{zz,i} = \frac{E_i}{(1+v_i)(1-2v_i)} [v_i(\epsilon_{\theta\theta,i} + \epsilon_{rr,i}) - (1-v_i)\epsilon_{zz,i} - (1+v_i)\alpha_i\theta_i] \quad \text{Eq. 3.39}$$

It is known that the equilibrium equation for axial symmetry in a composite cylinder is (Wang et al., 2015),

$$\frac{d\sigma_{rr,i}}{dr} + \frac{\sigma_{rr,i} - \sigma_{\theta\theta,i}}{r} = 0 \quad \text{Eq. 3.40}$$

By substituting Eq. 3.33 and Eq. 3.34 into Eq. 3.37 and Eq. 3.38, the equilibrium equation in terms of radial displacement $u_{r,i}$ can be obtained as (Wang et al., 2015),

$$\frac{d}{dr} \left[\frac{1}{r} \frac{d(u_{r,i}r)}{dr} \right] = \frac{1+v_i}{1-v_i} \alpha_i \frac{d\theta_i}{dr} \quad \text{Eq. 3.41}$$

Integrating Eq. 3.41 gives the radial displacement equation as

$$u_{r,i}(r) = \beta_i C_i r + \lambda_i \frac{(D_i + I_i)}{r} \quad \text{Eq. 3.42}$$

$$u_{\theta,i}(r) = 0 \quad \text{Eq. 3.43}$$

$$u_z(r) = C_z \frac{z}{L} = \epsilon_{zz} z \quad \text{Eq. 3.44}$$

where

$$I_i = I_i(r) = -\frac{E_i \alpha_i}{1-\nu_i} \int_{r_{i-1}}^r \theta_i r dr, \quad \beta_i = \frac{(1+\nu_i)(1-2\nu_i)}{E_i}, \quad \lambda_i = -\frac{(1+\nu_i)}{E_i}$$

$$C_i = \frac{\hat{C}}{\beta_i}, \quad D_i = \frac{\hat{D}}{\lambda_i}, \quad \text{The } \hat{C} \text{ and } \hat{D} \text{ are the integration constant.} \quad \text{Eq. 3.45}$$

Rewrite the Eq. 3.37 - Eq. 3.39 in terms of C_i and D_i yields

$$\begin{aligned} \sigma_{rr,i}(r) &= C_i + \frac{D_i + I_i}{r^2} + \varphi_i \\ \sigma_{\theta\theta,i}(r) &= C_i - \frac{D_i + I_i}{r^2} + \varphi_i - \frac{E_i \alpha_i \theta_i}{(1-\nu_i)} \\ \sigma_{zz,i}(r) &= 2\nu_i C_i + \hat{E}_i (1-\nu_i) \epsilon_{zz} - \frac{E_i \alpha_i \theta_i}{(1-\nu_i)} \end{aligned} \quad \text{Eq. 3.46}$$

$$\text{where } \varphi_i = \nu_i \epsilon_{zz} / \beta_i \quad \text{Eq. 3.47}$$

To calculate the radial stresses and displacements across the wall of the hollow cylinder, the constants C_i and D_i may be determined by utilizing Eq. 3.7 and Eq. 3.8. It yields

$$C_i + \frac{D_i + I_i}{r_i^2} + \varphi_i = C_{i+1} + \frac{D_{i+1} + I_{i+1}^0}{r_i^2} + \varphi_{i+1} \quad \text{Eq. 3.48}$$

$$\beta_i C_i r_i + \lambda_i \frac{(D_i + I_i)}{r_i} = \beta_{i+1} C_{i+1} r_i + \lambda_{i+1} \frac{(D_{i+1} + I_{i+1}^0)}{r_i} \quad \text{Eq. 3.49}$$

where

$$I_{i+1}^0 = I_{i+1}(r_i) = -\frac{E_{i+1} \alpha_{i+1}}{1-\nu_{i+1}} \int_{r_i}^{r_i} \theta_i r dr = 0;$$

$$I_i = I_i(r_i) = -\frac{E_i \alpha_i}{1-\nu_i} \int_{r_{i-1}}^{r_i} \theta_i r dr \quad \text{Eq. 3.50}$$

Solving Eq. 3.48 and Eq. 3.49 results in the constants C_{i+1} and D_{i+1} as

$$D_{i+1} = (D_i + I_i) \left(\frac{\lambda_i - \beta_{i+1}}{\lambda_{i+1} - \beta_{i+1}} \right) + C_i r_i^2 \left(\frac{\beta_i - \beta_{i+1}}{\lambda_{i+1} - \beta_{i+1}} \right) + \beta_{i+1} r_i^2 \left(\frac{\varphi_{i+1} - \varphi_i}{\lambda_{i+1} - \beta_{i+1}} \right)$$

$$C_{i+1} = \left(\frac{D_i + I_i}{r_i^2} \right) \left(\frac{\lambda_{i+1} - \lambda_i}{\lambda_{i+1} - \beta_{i+1}} \right) + C_i \left(\frac{\lambda_{i+1} - \beta_i}{\lambda_{i+1} - \beta_{i+1}} \right) + \lambda_{i+1} \left(\frac{\varphi_i - \varphi_{i+1}}{\lambda_{i+1} - \beta_{i+1}} \right) \quad \text{Eq. 3.51}$$

Utilizing the radial stresses of two adjacent layers gives the corresponding contact pressure as

$$\sigma_{rr,i}(r_{i-1}) = -p_{i-1} \Rightarrow C_i + \frac{D_i + I_i^0}{r_{i-1}^2} + \varphi_i = -p_{i-1}$$

$$\sigma_{rr,i+1}(r_{i+1}) = -p_{i+1} \Rightarrow C_{i+1} + \frac{D_{i+1} + I_{i+1}^0}{r_{i+1}^2} + \varphi_{i+1} = -p_{i+1} \quad \text{Eq. 3.52}$$

$$\text{where } I_i^0 = I_i(r_{i-1}) = -\frac{E_i \alpha_i}{1-\nu_i} \int_{r_{i-1}}^{r_{i-1}} \theta_i r dr = 0 \quad \text{Eq. 3.53}$$

Substituting Eq. 3.52 into Eq. 3.51 yields

$$D_i = \gamma_i r_i^2 \left(\frac{p_{i-1} G_i - p_{i+1} (\lambda_{i+1} - \beta_{i+1}) + \varphi_i (G_i + \beta_{i+1} \gamma_{i+1} - \lambda_{i+1}) - \varphi_{i+1} \beta_{i+1} (\gamma_{i+1} - 1)}{S_i - G_i} \right) - \frac{I_i S_i + I_{i+1} \gamma_i \gamma_{i+1} (\lambda_{i+1} - \beta_{i+1})}{S_i - G_i}$$

$$C_i = \frac{-p_{i-1} S_i + p_{i+1} (\lambda_{i+1} - \beta_{i+1}) - \varphi_i (S_i + \beta_{i+1} \gamma_{i+1} - \lambda_{i+1}) + \varphi_{i+1} \beta_{i+1} (\gamma_{i+1} - 1)}{S_i - G_i} + \frac{I_i S_i + I_{i+1} \gamma_i \gamma_{i+1} (\lambda_{i+1} - \beta_{i+1})}{r_{i-1}^2 (S_i - G_i)} \quad \text{Eq. 3.54}$$

where

$$S_i = \gamma_i \gamma_{i+1} (\lambda_i - \beta_{i+1}) + (\lambda_{i+1} - \lambda_i) \gamma_i$$

$$G_i = \lambda_{i+1} - \beta_i + (\beta_i - \beta_{i+1}) \gamma_{i+1}$$

$$\gamma_{i+1} = \frac{r_i^2}{r_{i+1}^2} \quad \text{Eq. 3.55}$$

The radial stress on outer surface of i -layer has the contact pressure as following,

$$\sigma_{rr,i}(r_i) = -p_i \Rightarrow C_i + \frac{D_i + I_i}{r_i^2} + \varphi_i = -p_i \quad \text{Eq. 3.56}$$

Next, substituting Eq. 3.54 into Eq. 3.56 yields the relationship of the adjacent contact pressures as

$$p_{i+1} = \frac{p_{i-1}(S_i - \gamma_i G_i) - p_i(S_i - G_i)}{(1 - \gamma_i)(\lambda_{i+1} - \beta_{i+1})} - \frac{I_{i+1}\gamma_{i+1}(\lambda_{i+1} - \beta_{i+1})(1 - \gamma_i) + I_i \left(\frac{S_i}{\gamma_i} - T_i \right)}{r_i^2(1 - \gamma_i)(S_i - G_i)} - \frac{(1 - \gamma_{i+1})(v_i - v_{i+1})\epsilon_{zz}}{(\lambda_{i+1} - \beta_{i+1})} \quad \text{Eq. 3.57}$$

Also, substituting Eq. 3.57 into Eq. 3.54 results in the constants D_i and C_i as

$$D_i = \frac{\gamma_i r_i^2}{1 - \gamma_i} \left(p_i - p_{i-1} + \frac{I_i}{r_i^2} \right) \quad \text{Eq. 3.58}$$

$$C_i = \frac{1}{1 - \gamma_i} \left(\gamma_i p_{i-1} - p_i - \frac{I_i}{r_i^2} \right) - \varphi_i \quad \text{Eq. 3.59}$$

To solve D_i and C_i as well as p_i in terms of p_0 and p_n , two simple recurrence relations can be proposed as

$$c_{i+1} = \frac{c_{i-1}(S_i - \gamma_i G_i) - c_i(S_i - G_i)}{(1 - \gamma_i)(\lambda_{i+1} - \beta_{i+1})} \quad \text{Eq. 3.60}$$

$$d_{i+1} = \frac{d_{i-1}(S_i - \gamma_i G_i) - d_i(S_i - G_i)}{(1 - \gamma_i)(\lambda_{i+1} - \beta_{i+1})} - \frac{I_{i+1}\gamma_{i+1}(\lambda_{i+1} - \beta_{i+1})(1 - \gamma_i) + I_i \left(\frac{S_i}{\gamma_i} - T_i \right)}{p_0 r_i^2 (1 - \gamma_i)(S_i - G_i)} - \frac{(1 - \gamma_{i+1})(v_i - v_{i+1})\epsilon_{zz}}{p_0(\lambda_{i+1} - \beta_{i+1})} \quad \text{Eq. 3.61}$$

where $i = 1, 2, \dots, (n-1)$.

Introducing p_i in terms of the recurrence relations gives

$$p_i = c_i p_1 + d_i p_0 \quad \text{Eq. 3.62}$$

For given initial values of

$$c_0 = 0, c_1 = 1, d_0 = 1, d_1 = 0 \quad \text{Eq. 3.63}$$

when $i = n$, it is found that

$$p_1 = \frac{p_n - d_n p_0}{c_n} \quad \text{Eq. 3.64}$$

Thus, solving p_i in terms of the recurrence relations and its boundary values results in

$$p_i = \frac{c_i}{c_n} p_n + \left(d_i - \frac{d_n}{c_n} c_i \right) p_0 \quad \text{Eq. 3.65}$$

Since the Eq. 3.61 consists of an unknown ϵ_{zz} , a solution strategy is proposed to isolate ϵ_{zz} by dividing d_i in Eq. 3.62 into two terms as,

$$d_i = e_i + f_i \epsilon_{zz} \quad \text{Eq. 3.66}$$

The e_i and f_i can be defined as,

$$e_{i+1} = \frac{e_{i-1}(S_i - \gamma_i G_i) - e_i(S_i - G_i)}{(1 - \gamma_i)(\lambda_{i+1} - \beta_{i+1})} - \frac{I_{i+1} \gamma_{i+1} (\lambda_{i+1} - \beta_{i+1})(1 - \gamma_i) + I_i \left(\frac{S_i}{\gamma_i} - T_i \right)}{p_0 r_i^2 (1 - \gamma_i)(S_i - G_i)} \quad \text{Eq. 3.67}$$

$$f_{i+1} = \frac{f_{i-1}(S_i - \gamma_i G_i) - f_i(S_i - G_i)}{(1 - \gamma_i)(\lambda_{i+1} - \beta_{i+1})} - \frac{(1 - \gamma_{i+1})(v_i - v_{i+1})}{p_0 (\lambda_{i+1} - \beta_{i+1})} \quad \text{Eq. 3.68}$$

With the given initial values as,

$$e_0 = 1, e_1 = 0, f_0 = f_1 = 0 \quad \text{Eq. 3.69}$$

Now Eq. 3.62 can be written as

$$p_i = \frac{a_i}{a_n} p_n + \left(e_i - \frac{e_n}{a_n} a_i \right) p_0 + \left(f_i - \frac{f_n}{a_n} a_i \right) p_0 \epsilon_{zz} \quad \text{Eq. 3.70}$$

Reorganize Eq. 3.70 into

$$p_i = p_i^o + \omega_i \epsilon_{zz} \quad \text{Eq. 3.71}$$

where

$$\omega_i = \left(f_i - \frac{f_n}{a_n} a_i \right) p_0$$

$$p_i^o = \frac{a_i}{a_n} p_n + \left(e_i - \frac{e_n}{a_n} a_i \right) p_0 \quad \text{Eq. 3.72}$$

Considering for the case of generalized plane strain condition with axial load is zero, the ϵ_{zz} can be found as follows,

$$\sum_{i=1}^n \sigma_{zz,i} \pi (r_i^2 - r_{i-1}^2) = F_{zz} = 0 \quad \text{Eq. 3.73}$$

$$\sum_{i=1}^n r_i^2 (1 - \gamma_i) \left\{ \frac{2v_i}{(1-\gamma_i)} \left(\gamma_i p_{i-1}^o - p_i^o - \frac{I_i}{r_i^2} \right) - \frac{E_i \alpha_i \theta_i}{(1-\nu_i)} + \left[\frac{2v_i}{(1-\gamma_i)} (\gamma_i \omega_{i-1} - \omega_i) + E_i \right] \epsilon_{zz} \right\} = 0 \quad \text{Eq. 3.74}$$

$$\epsilon_{zz} = \frac{-\pi \sum_{i=1}^n r_i^2 \left[2v_i \left(\gamma_i p_{i-1}^o - p_i^o - \frac{I_i}{r_i^2} \right) - \frac{E_i \alpha_i \theta_i (1 - \gamma_i)}{(1 - \nu_i)} \right]}{\pi \sum_{i=1}^n r_i^2 [2v_i (\gamma_i \omega_{i-1} - \omega_i) + E_i (1 - \gamma_i)]} \quad \text{Eq. 3.75}$$

3.2.6 Computational procedures

A simple computational procedure using a recursive method for estimating the temperatures and stress-strain across the wall of the multi-layer hollow cylinder is proposed as follows:

- 1) Determine the sequences of $\{\bar{T}_i\}$ in Eq. 3.32.
- 2) Compute the sequences of $\{A_i\}$ and $\{B_i\}$ in Eq. 3.22 and Eq. 3.23, and use them to calculate the sequences of $\{I_i\}$ in Eq. 3.50.
- 3) Establishing the sequences of $\{\beta_i\}$ and $\{\lambda_i\}$ in Eq. 3.45 and $\{\varphi_i\}$ in Eq. 3.47, then use them to compute the sequences of $\{S_i\}$, $\{G_i\}$ and $\{\gamma_i\}$ in Eq. 3.55.
- 4) Find the sequences of $\{c_i\}$, $\{e_i\}$ and $\{f_i\}$ in Eq. 3.60 Eq. 3.67 and Eq. 3.68, respectively.
- 5) Calculate the sequences of $\{p_i^o\}$ and $\{\omega_i\}$ in Eq. 3.72 and use them to find ϵ_{zz} in Eq. 3.75.
- 6) Determine the sequences of $\{p_i\}$ in Eq. 3.70.
- 7) $\{C_i\}$ and $\{D_i\}$ can be determined based on Eq. 3.58 and Eq. 3.59.

- 8) Lastly, making use of the computed sequences of $\{A_i\}$, $\{B_i\}$, $\{C_i\}$ and $\{D_i\}$, the temperatures in Eq. 3.11 ,stresses in Eq. 3.37 - Eq. 3.39 and strains in Eq. 3.33 - Eq. 3.35 can be obtained.

3.2.7 Convection coefficient of internal flow, h_s

To determine the convection coefficient of steam (h_s) for Eq. 3.1, the steam flow in tubes can be treated as a fully developed turbulent flow (French, 1993). The heat transfer inside the boiler tube is considered as an internal forced convection with turbulent flow. Thus, the Nusselt number of the steam can be computed using the Dittus-Boelter equation (French, 1993; Huang et al., 2013):

$$Nu = 0.023 (Re_s)^{0.8} (Pr_s)^{0.4} \quad \text{Eq. 3.76}$$

where the Reynolds number (Re_s) and the Prandtl number (Pr_s) of the steam can be expressed as:

$$Re_s = \frac{\dot{m}_s}{900\pi D_1 \mu_s} \quad \text{Eq. 3.77}$$

$$Pr_s = \frac{\mu_s C_{p_s}}{k_s} \quad \text{Eq. 3.78}$$

where \dot{m}_s is mass flow rate of steam (kg/h), D_1 is inner diameter of tube (m), μ_s dynamic viscosity of steam (N s/m²), C_{p_s} is specific heat of steam (J/kg °C) and k_s is the thermal conductivity of steam (W/m °C).

In order to determine the dynamics viscosity, specific heat and thermal conductivity of steam, the operating steam temperature and pressure are required. Thus, the values for dynamic viscosity (μ_s), specific heat (C_{p_s}) and thermal conductivity (k_s) of

the steam are extracted from the Tables of Steam Dynamic Viscosity, Specific Heat and Thermal Conductivity (Wagner & Kretzschmar, 2007).

The Eq. 3.76 must comply with the following conditions (Incropera, 2011):

- I) $0.7 < Pr < 160$
- II) $Re > 10\,000$
- III) $\frac{L}{D} > 10$; where L is the length of tube, m
- IV) All fluid properties are evaluated at mean temperature, T_m .

Since

$$Nu = \frac{h_s D_1}{k_s} \quad \text{Eq. 3.79}$$

the steam convection coefficient for fully developed turbulent flow in circular tube is obtained by rearranging the Eq. 3.79

$$h_s = 0.0023 \frac{k_s}{D_1} (Re_s)^{0.8} (Pr_s)^{0.4} \quad \text{Eq. 3.80}$$

3.2.8 Convection coefficient of external flow on tubes, h_g

The heat transfer of the hot flue gas outside the boiler tube is treated as external forced convection as a result of cross flow of the flue gas over the superheater and reheater tubes. To estimate the convection coefficient of flue gas (h_g) for Eq. 3.3, the flow of flue gas over the bare tubes can be expressed as (Ganapathy, 2003):

$$h_g = 0.33 \frac{k_g}{D_o} (Re_g)^{0.6} (Pr_g)^{0.33} \quad \text{Eq. 3.81}$$

whereby the Reynolds (Re_g) and Prandtl (Pr_g) numbers of flue gas can be expressed as:

$$Re_g = \frac{G_v D_o}{3600 \mu_g} \quad \text{Eq. 3.82}$$

$$Pr_g = \frac{\mu_g C_{p_g}}{k_g} \quad \text{Eq. 3.83}$$

where k_g (W/m °C) is the thermal conductivity of flue gas, D_o (m) is outer diameter of tube, μ_g (N s/m²) is dynamic viscosity of flue gas and C_{p_g} (J/kg °C) is specific heat of flue gas.

The corresponding gas mass velocity (G_v) may be expressed as:

$$G_v = \frac{W_g}{N_w L (S_t - D_o)} \quad \text{Eq. 3.84}$$

where W_g (kg/h) is gas flow, N_w is number of tube wide, L (m) is length of tube, S_t (m) is transverse pitch depending the type of tubes arrangement (see Figure 3.2).

The dynamic viscosity, specific heat and thermal conductivity of flue gas can be obtained from the Tables of Steam Dynamic Viscosity, Specific Heat and Thermal Conductivity in Ganapathy (2003) and the equations as shown in the following:

$$\mu_g = \frac{\sum Y_i \mu_i (MW_i)^{-1}}{\sum Y_i (MW_i)^{-1}} \quad \text{Eq. 3.85}$$

$$C_{p_g} = \frac{\sum C_{p_i} MW_i Y_i}{\sum MW_i Y_i} \quad \text{Eq. 3.86}$$

$$k_g = \frac{\sum Y_i k_i (MW_i)^{-3}}{\sum Y_i (MW_i)^{-3}} \quad \text{Eq. 3.87}$$

where MW is molecular weight, Y is volume fraction and i is gas constituent.

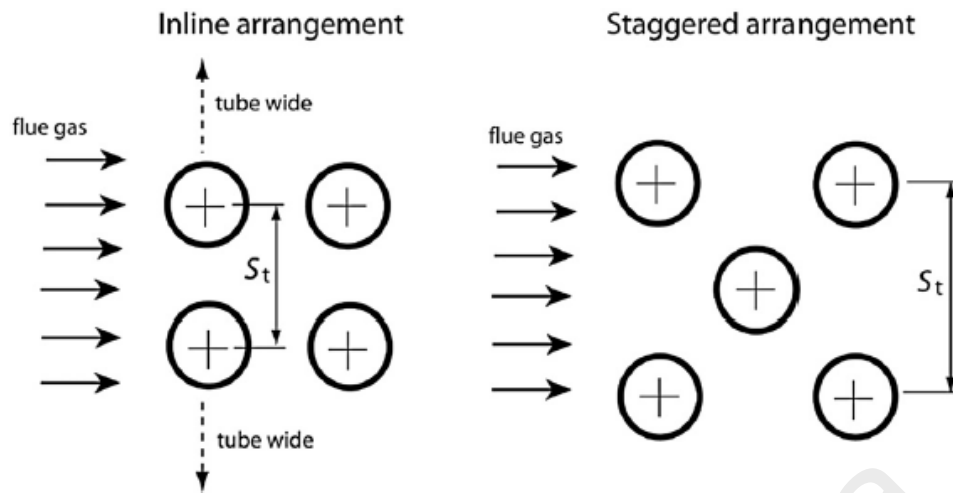


Figure 3.2: Inline and staggered arrangements of bare tubes (Purbolaksono et al., 2010)

3.3 Iterative procedure for scale growth prediction

The oxide layers formed on 18% Cr austenitic steel commonly consist of two distinct layers (duplex): an outer layer of porous magnetite and inner layer consisting of a mixture of Fe-Cr spinel and $(\text{Fe,Cr,Mo})_3\text{O}_4$, meanwhile the oxide scale in nickel-based alloys consists of an outer layer of essentially Cr_2O_3 with some MnCr_2O_4 and traces of Ni (Wright & Dooley, 2010). However, for simplification and the purposes of this study the scale shall be treated as to be all magnetite (for austenitic alloys) and Cr_2O_3 (for nickel based alloys).

The scale growth prediction is carried out using incremental approach and the relationship between the Larson Miller Parameter (LMP) and the scale thickness. The data of the scale thickness versus the LMP such as shown in Figure 3.3 can be generally approximated in the form of a linear equation

$$\text{Log}(X) = C_h \cdot \text{LMP} - C_m \quad \text{Eq. 3.88}$$

where the constant C_m are found to be 10.633 (upper band), 11.133 (mean value), 11.633 (lower band) for austenitic alloys, and 12.235 (upper band), 12.696 (mean value), 13.156 (lower band) for nickel-based alloys. Meanwhile, the constant C_h for both austenitic and

nickel-based alloys is 0.000564 and X is the scale thickness in μm . and the Larson-Miller method LMP as a function of time and temperature is expressed as (Fry, 2011),

$$\text{Log}(X) = (T + 273)(20 + \log t) \quad \text{Eq. 3.89}$$

where T is the temperature in degree Celsius; t is the service time in hours. The raw data (provided in Appendix A) for the Larson Miller Parameter and the scale thickness are available through a personal communication with National Physical Laboratory, United Kingdom (Fry, 2011) and would be utilized in this work for scale growth prediction.

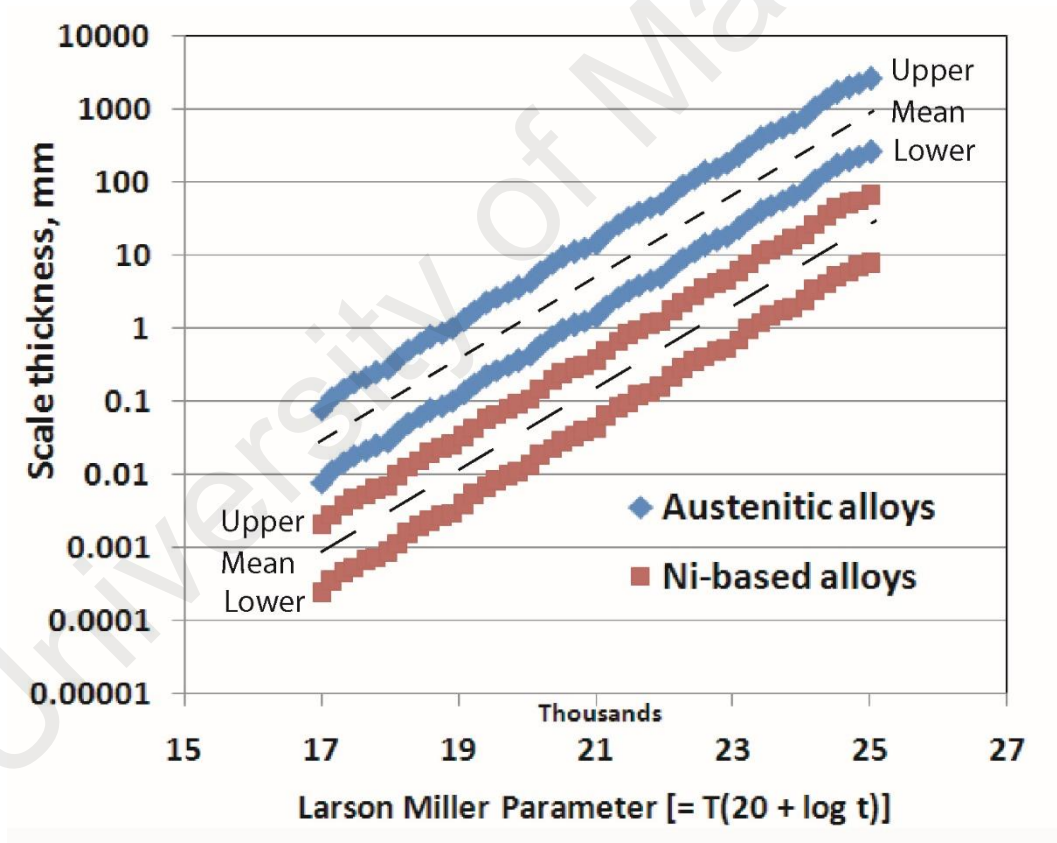


Figure 3.3: Bands of data for the relationship between the Larson-Miller Parameter and the oxide scale thickness for austenitic and nickel-based alloys (Fry, 2011).

The incremental procedures used to determine the metal temperature and scale thickness over a period of time in superheater/reheater tubes can be summarized as follows:

Step 1: The design temperature for the steam is set to \bar{T}_{steam} at the inlet of the reheater or superheater tube. In the absence of scale (X_0), the average temperature of T_{ave1} can be taken from the temperature on the internal diameter (ID) of the tube for steam-side scale estimation or on the outer diameter of the tube for fireside scale estimation. Eq. 3.88 is used to calculate the scale thickness of X_{1a} and X_{1b} for the service time of 1 h and 1000 h respectively (see Table 3.6) using the average temperature of T_{ave1} . Subsequently, by subtracting one from the other, the scale increase of $\Delta X_1 (=X_{1b} - X_{1a})$ is determined and a new scale thickness of $X_1 (=X_0 + \Delta X_1)$ is obtained.

Step 2: A newly calculated steam-side/fireside scale thickness is used to define the radii for steam-side scale/metal interface or/and metal/fireside scale interface. The average temperature of T_{ave2} can be obtained from the average of the temperatures at the ID of the tube and the steam-side scale/metal interface (for the internal scale estimation) or the average of the temperatures at the OD of the tube and the metal/fireside scale interface (for the external scale estimation). The average temperature of T_{ave2} is then used to calculate the scale thickness of X_{2a} and X_{2b} for the service time of 1000 and 2500 h respectively using Eq. 3.88. Subsequently, by subtracting one from the other, the scale increase of $\Delta X_2 (=X_{2b} - X_{2a})$ is determined and a new scale thickness of $X_2 (=X_1 + \Delta X_2)$ is obtained. The temperature distribution and thermo-mechanical stress-strain of the tube can be estimated based on the new geometry with scale thickness by using the computational procedure presented in section 3.2.6. Repeat *Step 2* for further estimations until the final step time as stated in Table 3.6. In the event of spallation of steam-side or fireside scales at the assumed service hours, the corresponding ID or OD of the tube is redefined for wall thinning.

3.4 Failure criteria for oxide scale

The approach used to estimate the critical failure strain in oxide scale is based on the Advance Oxide Scale Failure Diagram (AOSFD) which was reported in Schütze et al. (2010). Under the tensile loading, the critical strain equation for through-scale cracking can be written as following

$$\varepsilon_c = \frac{K_{Ic}}{f \cdot E \sqrt{\pi \tilde{c}_0}} \left(\frac{\tilde{c}_0}{\tilde{c}} \right)^{1/2} \quad \text{Eq. 3.90}$$

where K_{Ic} is fracture toughness (mode I) of the oxide as a material constant (MPa.m^{1/2}); f is geometrical parameter ($f = 1$ for buried defects, 1.12 for a surface defect of infinite length or 0.64 for a semicircular defect of radius c); \tilde{c} , \tilde{c}_0 are size of a physical scale defect (pore, flaw, etc. in μm) with \tilde{c}_0 as a value for normalizing the defect size (\tilde{c}/\tilde{c}_0 dimensionless), in current study the \tilde{c}_0 is set to 1 μm ; E denotes the Young's modulus of the oxide scale (MPa); ν is Poisson ratio.

3.5 Physical Data and Parameters

The properties of steam and flue gas from different sources (Ganapathy, 2003; Hay et al., 2009; NiDL, 2014; Salzgitter, 2008; VdTÜV, 2007; Wagner & Kretzschmar, 2007) are presented in Table 3.1. The steam flows through the internal bore of the tube with four different inlet temperatures of 650°C, 700°C, 750°C and 800°C and two steam mass flow rates of 1800 kg/h and 3600 kg/h have been considered. It is not uncommon that the supercritical fossil-fuel boilers have an operating flue gas temperature ranging from 1000-1200°C. However, in this study a flue gas temperature of 1400°C is also considered, particularly for those tube models used in advance ultra-supercritical power plant ($\bar{T}_{steam} \geq 700^\circ\text{C}$). The 50 mm OD (outer diameter) x 10 mm thick tube is primarily used for the simulations. There are other 2 different dimensions of tube such as stated in Table 3.2 are

being used for investigation of effect of tube geometry on the overall performance of the tube. The widely used austenitic steel TP 347HFG and nickel-based Alloy 617 are chosen for the simulations. The properties are presented in Table 3.3. High-temperature nickel based alloy 617 (A 617) has been considered as one of the candidate materials for the 700 °C power plants due to its combination of good creep strength and good fabricability. The alloy that has been approved by VdTÜV (2007) and ASTM (2011) has been investigated in numerous publicly sponsored and privately financed programmes for consideration in the use in USC boilers (Klöwer et al., 2013).

Table 3.1: Properties of steam and flue gas

<i>Inlet steam properties at 35 MPa pressure (Wagner & Kretzschmar, 2007)</i>				
Temperature, °C	650	700	750	800
Thermal conductivity, W/m °C	0.1185	0.1218	0.1262	0.1311
Specific heat, J/kg °C	3110	2944	2840	2774
Dynamic viscosity, N s/m ²	3.77E-05	3.97E-05	4.12E-05	4.29E-05
<i>Flue gas composition, mole%</i>				
N ₂	72.8			
O ₂	14			
CO ₂	2.7			
H ₂ O	10.5			
<i>Flue gas properties (Ganapathy, 2003)</i>				
Temperature, °C		1000	1200	1400
Dynamics viscosity (×10 ⁻⁵), N s/m ²		4.58	5.24	5.64
Specific heat, J/kg °C		1289	1323	1346
Thermal conductivity, W/m °C		0.0793	0.0879	0.0959

Table 3.2: Geometry of tube models

Tube	Outer diameter, mm	Thickness, mm
1	50	10
2	50	7
3	56	10

Table 3.3: Properties of tube wall materials

Material	k (W/m °C)	E (GPa)	ν	α ($\times 10^{-6}$ °C ⁻¹)	K _{IC} (MPa.m ^{1/2})
Nickel-based alloy, Alloy 617 (NiDL, 2014)	23.2	168	0.3	14.4	
Austenitic steel, TP 347HFG (VdTÜV, 2007)	23.8	210	0.3	21.8	
Chromium oxide, Cr ₂ O ₃ (Hay et al., 2009; Schütze, 2005)	2.73	283	0.29	7.3	1.8
Iron oxide, Fe ₃ O ₄ (magnetite) (French, 1993; Schütze, 2005)	0.592	208	0.29	14	1.4

Table 3.4 shows the parameters for the tubes layout arrangement and the gas flow rate that are required for the estimation of gas mass velocity and the determination of convection coefficient at fireside of boiler tube. The conditions used in the case study models for different steam temperatures and steam flow rates as well as the different flue gas temperatures are listed in Table 3.5. Since the initial increment of time is critical in the determination of the results, the time steps used are also presented in Table 3.6. A smaller increment of time might provide a better estimation, whereas a bigger increment of time for initial iteration may be resulting in inaccuracy of the estimation or a less conservative prediction.

Table 3.4: Parameters used to determine gas mass velocity G_v .

<i>Tubes layout (staggered arrangement)</i>	
Gas flow rate, kg/h	400,000
Number of tube wide	40
Transverse pitch, m	2 x OD
Tube length, m	10

Table 3.5: Materials and heat transfer parameters referring to properties presented in

Table 3.1 and Table 3.3

Model*	Material	Steam temp., °C	Steam flow rate, kg/h	Flue gas temp., °C	h_s (steam), W/m ² °C	h_g (gas), W/m ² °C
1	347HFG	600	3600	1000	6569	91.41
2	347HFG,	650	3600	1000	6275	91.41
3	347HFG, Alloy 617	700	3600	1000	6113	91.41
4	Alloy 617	700	3600	1200	6113	95.26
5	Alloy 617	700	3600	1400	6113	99.56
6	347HFG, Alloy 617	750	3600	1000	6065	91.41
7	Alloy 617	750	3600	1200	6065	95.26
8	Alloy 617	750	3600	1400	6065	99.56
9	Alloy 617	800	3600	1000	6048	91.41
10	Alloy 617	800	3600	1200	6048	95.26
11	Alloy 617	800	3600	1400	6048	99.56

*All models are made of Tube 1 unless stated otherwise

Table 3.6: The steps of time used in the incremental procedure

Step No., <i>i</i>	Time increment, h	
	<i>Growth</i>	<i>Presumed Re-growth</i>
1	1	1
2	1000	1000
3	2500	2500
4	5000	5000
5	10000	10000
6	20000	20000
7	40000	21000
8	60000	22500
9	80000	25000
10	100000	30000
11	120000	40000
.	.	.
Last	180000	180000

3.6 Summary

The proposed methodology used to perform the analyses covering heat transfer problems and the analytical expression of thermo-mechanical stress strain for tube with oxide scales has been presented. Then the proposed iterative procedure can be used to estimate the scale growth either on the steam-side or fire-side or both surfaces based on the presumed boundary conditions. The Larson-Miller parameter is utilized to predict the scale growth in the iterative procedure. The properties, parameters and models presented in chapter are considered for the parametric and case studies. The findings and the corresponding analyses and discussion are presented in Chapter 4.

University of Malaya

CHAPTER 4: RESULTS AND DISCUSSION

4.1 Results validation

The results for validation consist of two parts. Firstly, the results obtained by using the proposed analytical method and are compared with those produced by finite element analysis (FEA) software of ANSYS. Then, a test case reported in literature is selected for a comparison study. Secondly, the results produced by using the proposed iterative procedure to estimate the oxide scale growth are validated with the field data reported in literature. Next, the results produced by using the iterative procedure based on the proposed analytical method are compared with those obtained from the FEA.

4.1.1 Validation for estimation of thermo-mechanical stress-strain developed in oxide scale

This section presents the comparison of results obtained by using the proposed method and the finite element analysis (FEA) software of ANSYS. Model 2 (as shown in Table 3.5) which contains the steam-side and fireside oxide scales is chosen for the validation study. The thickness of the steam-side scale is 0.5482 mm and the fireside scale thickness is 2.1429 mm. The tube material is austenitic steel (TP347HFG), and the oxide scales on both steam-side and fireside surfaces are treated as all magnetite. The tube and the oxide scales properties are defined referring to Table 3.2 and the temperature at the reference state is set to 670.9°C. In FEA, the 2-D axisymmetric quadrilateral element PLANE13 is applied to the model. A converged mesh size of 0.0001 is used, and layer interfaces of domain areas are glued in order to ensure the mesh connectivity. The temperature distribution, radial stress-strain and hoop stress-strain under the generalized plane strain condition are presented in Figure 4.1, 4.2 and 4.3, respectively. In general, it can be observed that the results obtained from the proposed analytical solution are shown to be in good agreement with those produced by using the FEA.

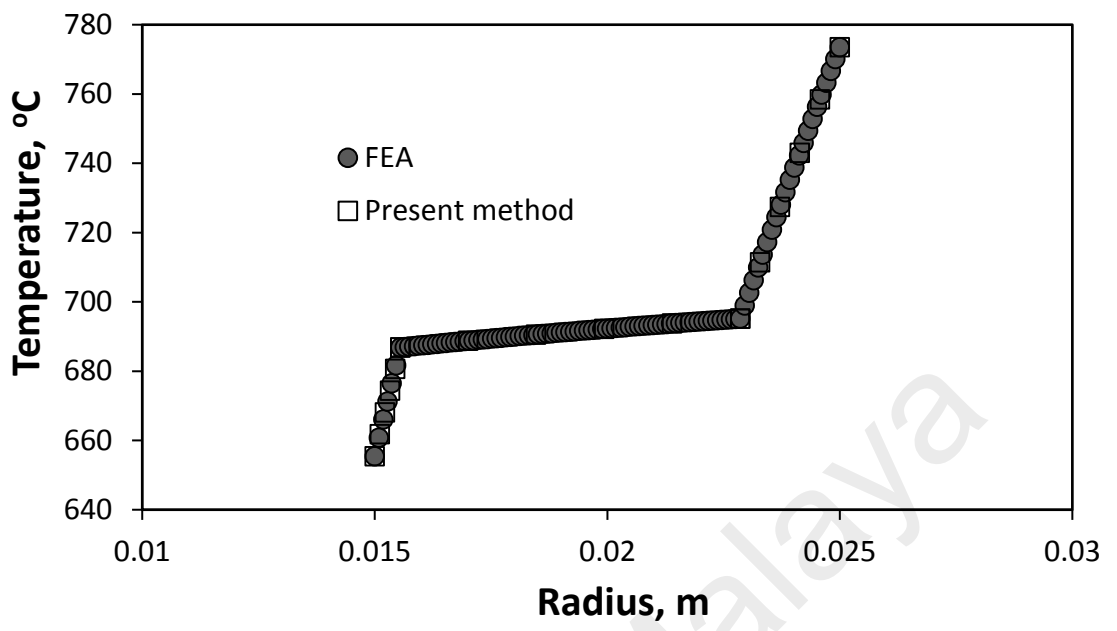


Figure 4.1: Temperature distribution across the tube.

University of Malaya

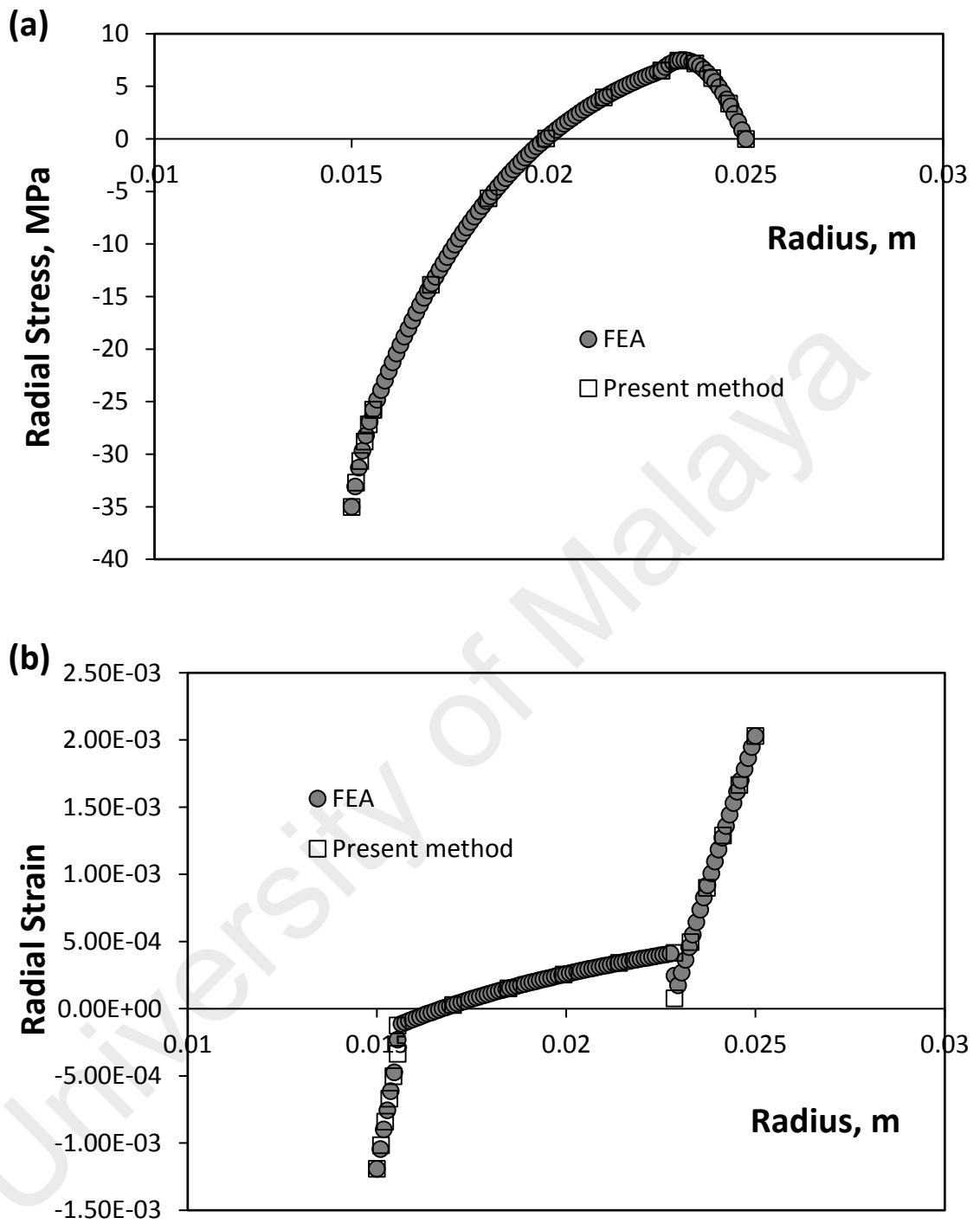


Figure 4.2: Radial stress and strain across the tube.

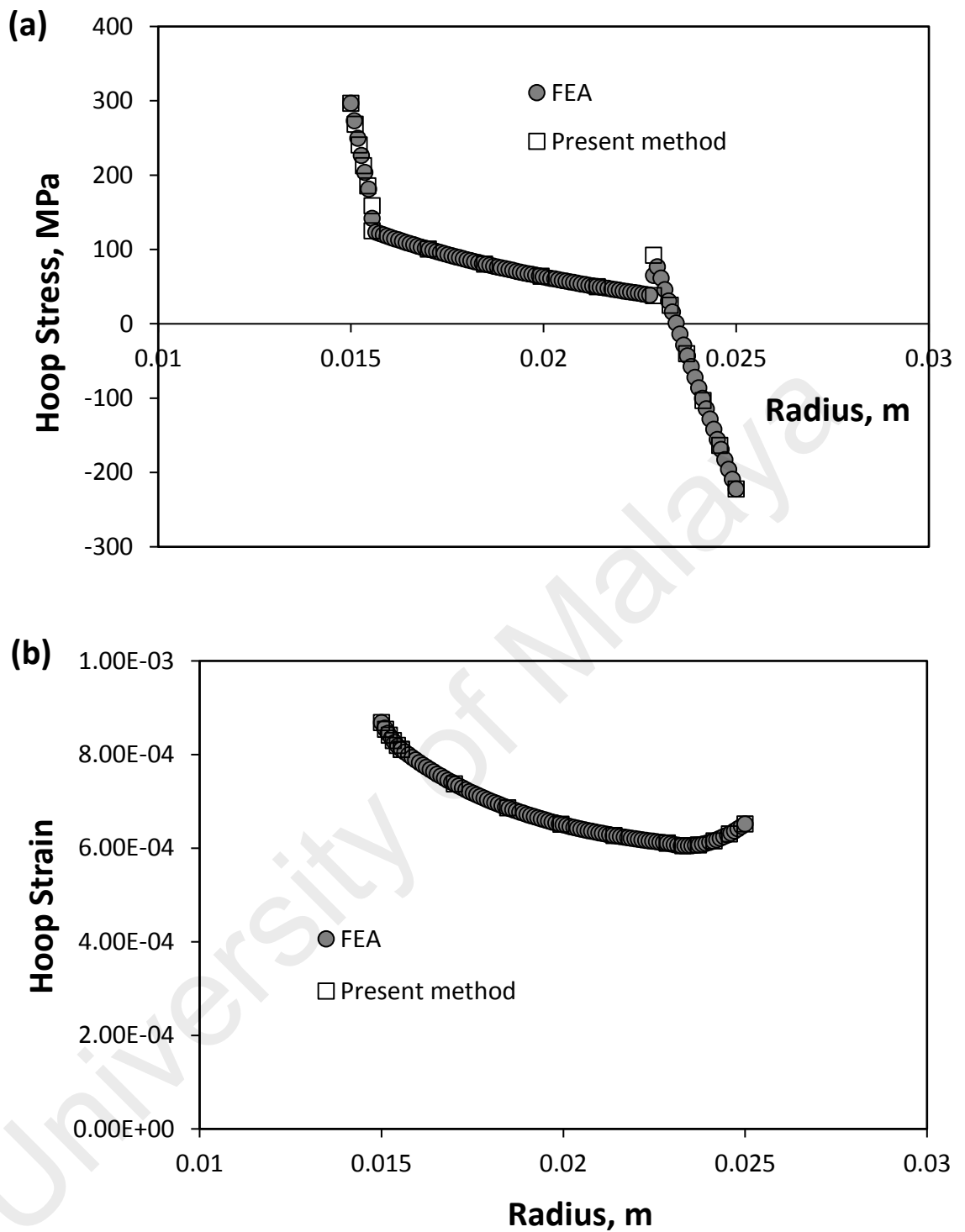


Figure 4.3: Hoop stress and strain across the tube.

To compare the results produced from the proposed analytical solution with those reported in literature, a test problem detailed in Sabau and Wright (2009) has been chosen. The geometric configuration in the test problem involving two hollow cylinders which

representing a tube with an oxide scale on its inner surface. The outer radius of the tube is 30 mm and the thickness and inner oxide layer of the tube are 5 mm and 200 μm , respectively. The tube material of T22 alloy is chosen and the oxide scale is assumed to be a single layer of Fe_3O_4 . Both metal tube and oxide scale are assumed to have the same Poisson's ratio (0.3) and Young's modulus (1.9×10^5 MPa) but different thermal expansion coefficients, which are $2.1 \times 10^{-5} \text{ K}^{-1}$ and $1.4 \times 10^{-5} \text{ K}^{-1}$ for the metal and oxide layers, respectively. The thermal conductivities are 3 W/m K and 30 W/m K for oxide scale and metal tube, respectively. For this test case, the plasticity and creep effect are neglected. The temperature is uniform in both the reference state (full load at 590°C) and current state (partial load, 460°C), thus, no temperature gradient effects are considered. As for the heat transfer coefficients on the flue gas side (h_g) and steam side (h_s), the following values are used, $h_s = 2800 \text{ W/m}^2 \text{ K}$ and $h_g = 100 \text{ W/m}^2 \text{ K}$. The pressure effects on the inner and outer surfaces are neglected so that the same pressure (10MPa) is used on both surfaces at the reference and current states.

The primary attention in this comparison study is focused on hoop stress and strain as they are the component stress strain that contribute to the damage of oxide scale (Sabau & Wright, 2009; Schütze, 2005; Schütze et al., 2010). Table 4.1 shows the comparison of hoop stress and strain results produced using present proposed method, the method reported in Sabau and Wright (2009) and FEA (ANSYS). It can be observed that the proposed analytical method has a good ability to estimate the hoop stress and strain better than the method reported in Sabau and Wright (2009). The results are comparable with those produced by using FEA-ANSYS. Therefore, the proposed computational method in the present work can be reliably used to estimate the thermo-mechanical stress-strain developed during the oxide growth.

Table 4.1: Hoop stress and hoop strain results in the oxide layer using present proposed method, Sabau & Wright method and FEA.

Stress-strain component	Sabau & Wright method		Present method		FEA	
	SPS	GPS	SPS	GPS	SPS	GPS
ε_{θ} ($\times 10^{-3}$)	-2.41	-1.86	-2.44	-1.89	-2.44	-1.89
σ_{θ} (MPa)	237		227		227	

SPS = Simple Plain Strain; GPS= Generalized plane strain assumption; ε_{θ} = hoop strain; σ_{θ} = Hoop stress.

4.1.2 Validation for prediction of oxide scale growth

In order to validate the reliability of the proposed iterative procedure for estimation of oxide scale growth, it is necessary to verify the simulation results with the actual data from power plants. Uerlings et al. (2008) have reported the measurements of steam-side scale thickness taken from the power plants for four different test steam loops (5,890 h, 12,000 h, 17770 h, and 23,215 h) under the KOMET 650 joint research project. It was reported that the average steam mass flow rate was 1 kg/s (3600 kg/h) and the tube geometry used was 31.8 mm OD x 5 mm thickness (Meyer et al., 2008). Three steam conditions, i.e. 575°C, 600°C, and 630°C, were considered in their work. However, more detailed operating heat transfer parameters of those power plants were not reported. The common operating flue gas temperature up to 1200°C is often used in this supercritical fossil-fuel boiler.

In the following comparisons, the steam-side scale growths are estimated by referring to the upper band of the relationship between the LMP and the scale thickness (Figure 3.3). The convection coefficients for the steam conditions of 600°C, 630°C, and 650°C in 31.8 mm OD x 5 mm are 11862 W/m² °C, 11557 W/m² °C, and 11414 W/m² °C, respectively. The flue gas temperature of 1200°C ($h_g = 74.5$ W/m² °C) is considered. The actual data (Uerlings et al., 2008) and the estimated results for the austenitic steels are presented in Figure 4.4. For a given service hour, the oxide scale growths for Super 304H

are shown to be larger than those of TP347HFG. It indicates that TP347HFG shows positive results. The actual data from the power plants are within the estimations.

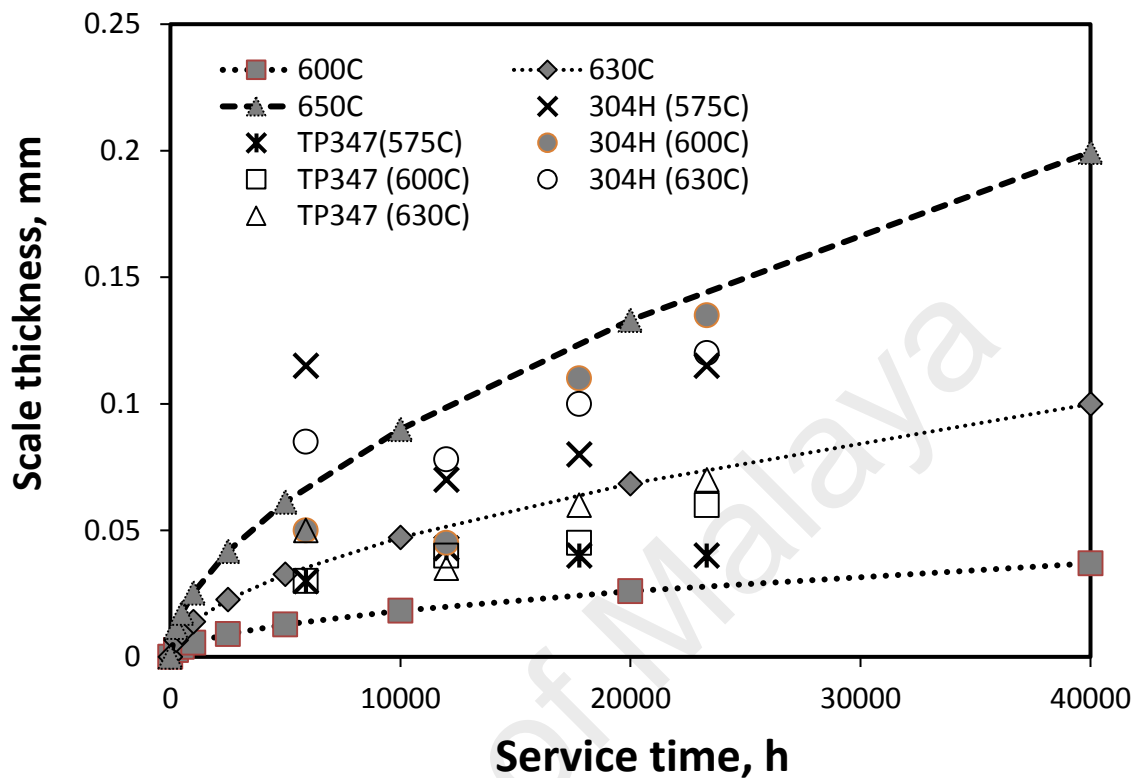


Figure 4.4: Estimated steam-side oxide scale growths and the actual data (304H and TP347) from the power plants for austenitic alloys (Uerlings et al., 2008).

Uerlings et al. (2008) also reported the measurements for nickel based alloy (Alloy 617) for a steam condition ranging from 639°C to 647°C at the same test steam loops. The steam-side oxide thicknesses were reported to be less 10 µm for all test steam loops. The estimations are shown to be in agreement with the actual data (Uerlings et al., 2008) at 630°C to 650°C steam condition (Figure 4.5). However, the calculations demonstrated here are intended to have rough estimations and shall ideally consider the real-time operating parameters for better estimations.

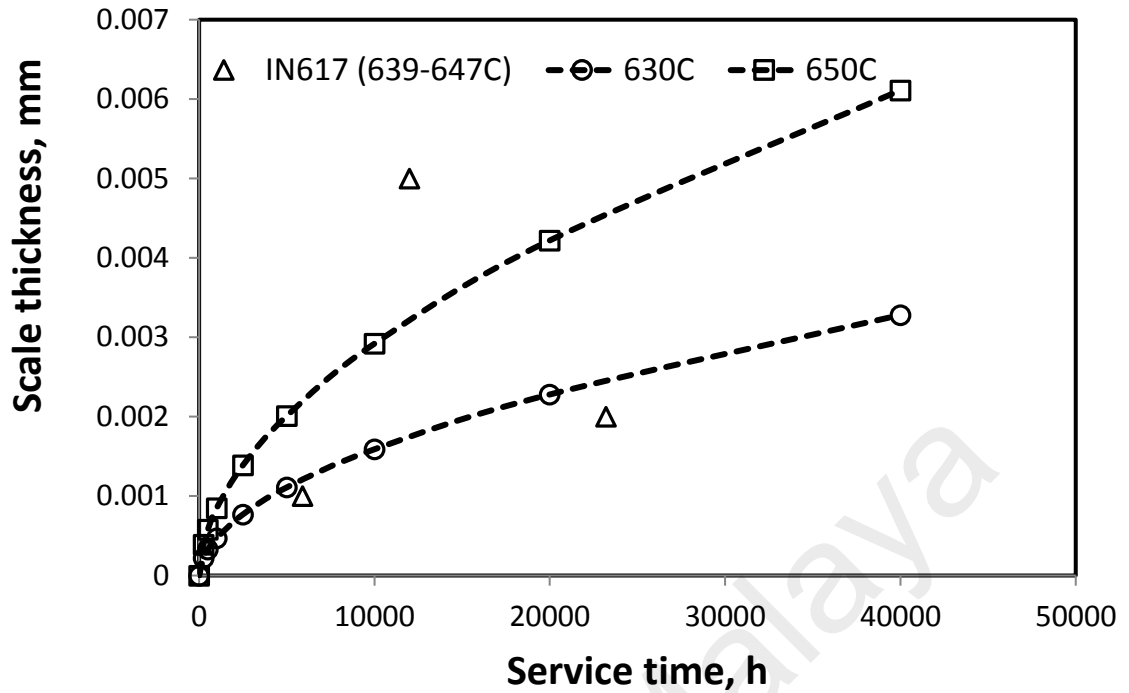


Figure 4.5: Estimated steam-side oxide scale growths and the actual data of nickel based alloy (Alloy 617) from the power plants (Uerlings et al., 2008).

To compare the scale growth results produced by using both analytical method and FEA, an austenitic boiler tube of 50 mm OD x 10 mm thickness with steam temperature of 700°C and flue gas temperature of 1000°C is used. Figure 4.6 shows the $\frac{3}{4}$ axisymmetric expansion of the simulated tube by using FEA after 80000 h in service. As it can be seen in Figure 4.7, the estimated results obtained using both proposed analytical method and FEA are shown to be in very good agreement. Although FEA may be utilized for the analysis, it could be too expensive in the implementation of the iterative procedure for the estimation of scale growth. On the other hand, the implementation of iterative procedure using the current proposed analytical solution is simple and efficient with good accuracy of the results.

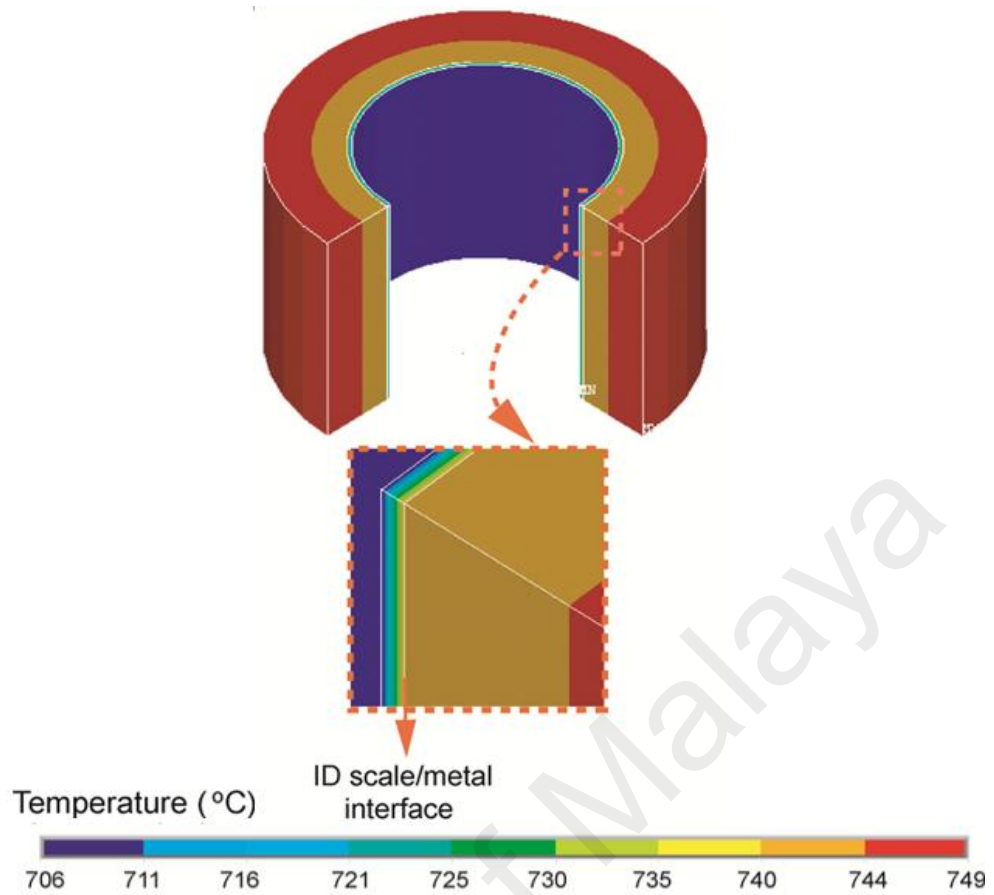


Figure 4.6: Temperature distributions of 2D axisymmetric solid in superheater tubes in FEA after 80000 h.

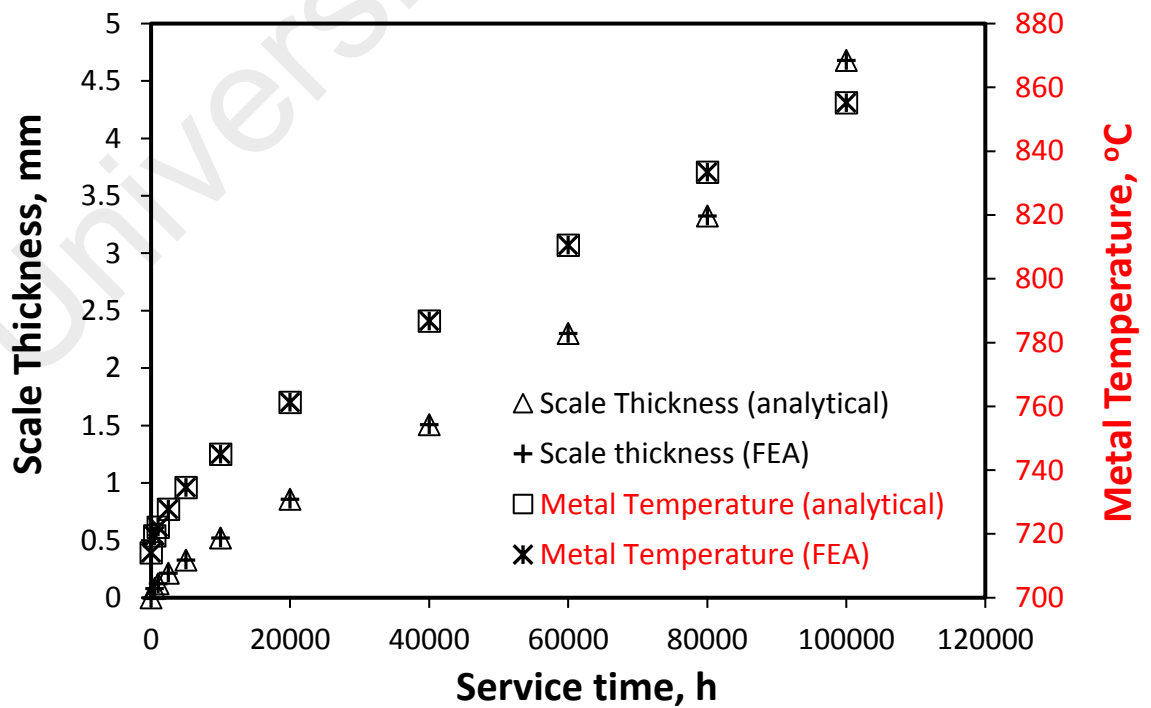


Figure 4.7: Comparison of simulated results obtained from analytical method and FEA.

4.2 The oxide scale failure diagram

The oxide scale failure diagram is plotted based on the Eq. 3.90 and it is used to examine the limit of integrity of the oxide scales. This critical failure strain in the failure diagram has considered the effects of physical defects, such as pores, cavities, and microcracks (Schütze et al., 2010). In order to plot the failure diagram in correlation with the scale thickness (d_{ox}), a factor of c/d_{ox} can be introduced. The c/d_{ox} can be established by comparing with the experimental data reported in the literatures such as shown in Figure 4.8 and Figure 4.9. Figure 4.8 shows the most of experimental data for the failure strain of magnetite (Fe_3O_4) are scattered between the two calculated curves corresponding respectively to $c/d_{ox} = 0.11$ and 0.4 . As for the chromium oxide (Cr_2O_3) shown in Figure 4.9, the experimental data for failure strain are mainly scattered between the curves to the case of $c/d_{ox} = 0.025$ and 0.5 . It should be pointed out that the data reported in literatures were obtained from different experiment conditions in the laboratory. Therefore, for conservative estimation, the critical failure strain can be obtained from the curve with $c/d_{ox} = 0.4$ for Fe_3O_4 and $c/d_{ox} = 0.5$ for Cr_2O_3 . Conversely, critical failure strain on the curve with $c/d_{ox} = 0.11$ for Fe_3O_4 and $c/d_{ox} = 0.025$ for Cr_2O_3 should be applied. It should be highlighted that the oxide scale failure diagram is to provide a general guide for the plant engineers to estimate when the exfoliation could start to occur. It is not meant to provide the size or amount of scale exfoliate from the tube.

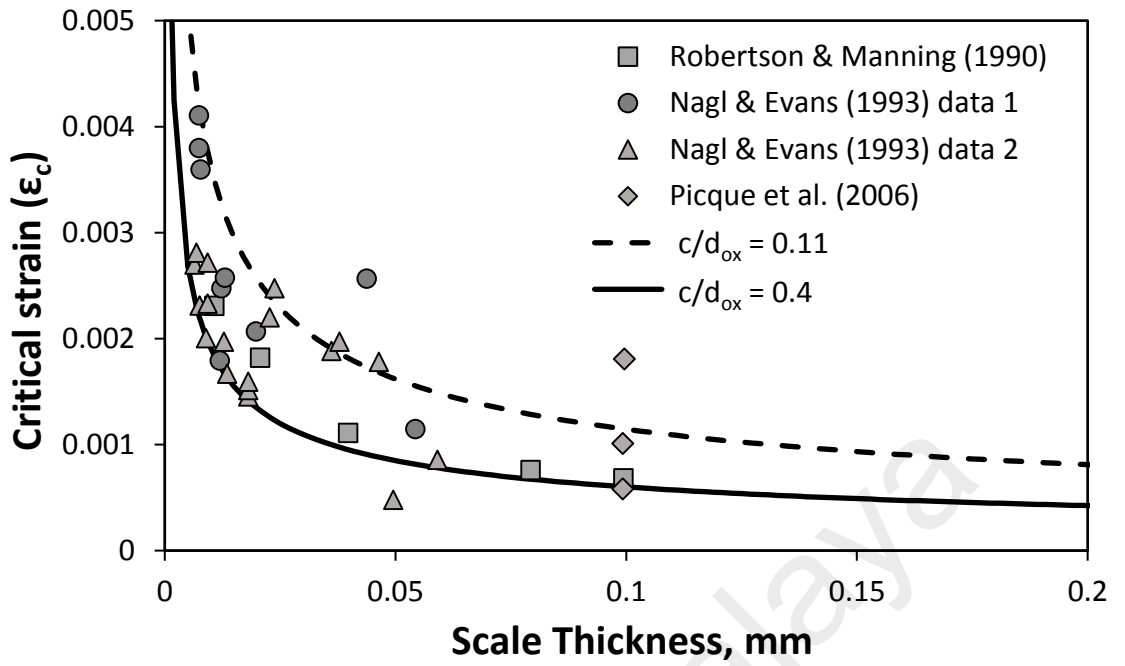


Figure 4.8: Oxide scale failure diagram of magnetite (Fe_3O_4)

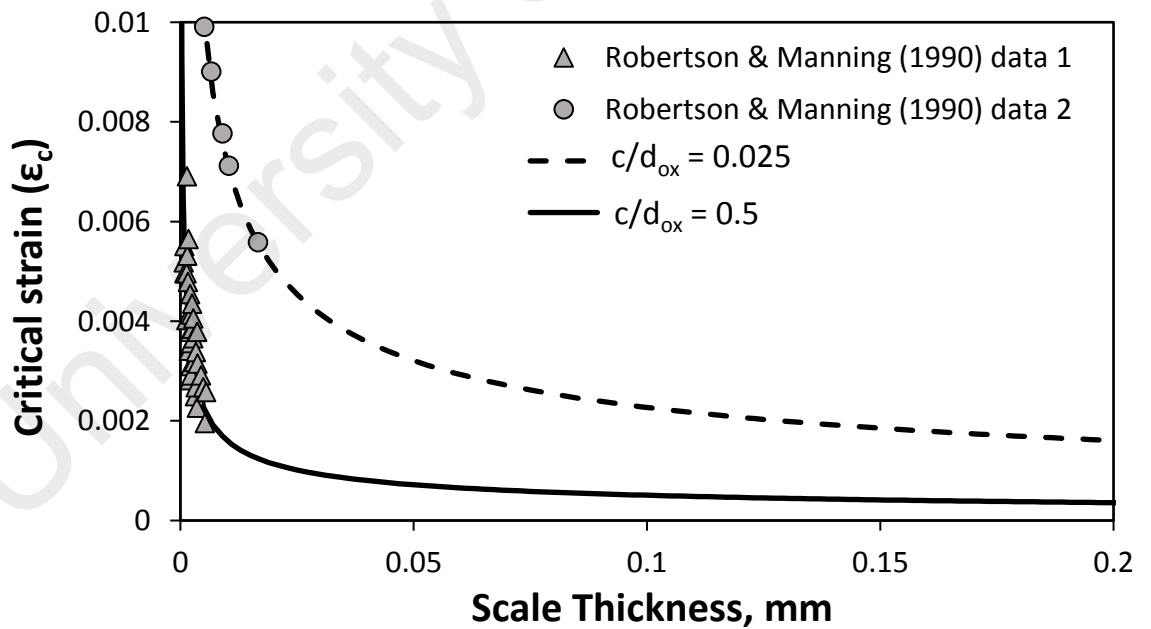


Figure 4.9: Oxide scale failure diagram of chromium oxide (Cr_2O_3)

4.3 Case A: Growth of steam-side oxide scale on tubes

Figure 3.3 shows scattered magnitudes of scale thickness in austenitic and nickel-based alloys versus the Larson-Miller Parameter (LMP) (Fry, 2011). In order to carry out a systematic analysis and show the magnitude of the steam-side oxide growth for different steam and flue gas temperatures (see Table 3.5), it is necessary to understand the effect of the data bands in LMP curve, particularly the upper band, mean values and lower band, on the rate of oxide scale growth over a period of time. Figure 4.10(a) shows the estimations of the steam-side scale growth and metal temperature for Model 1 (austenitic steel), which based on austenitic steel, using different LMP fitting constants (C_m) for upper, mean and lower bands. At 40,000 h in service, it is generally found that the estimation using Eq. 3.88 with constant, C_m based on upper band has order of three to four times of using the mean values, and it is similar order with the estimation using the mean value in comparison to that using C_m for lower band. However, those orders become greater as the service hours increase. Since the metal temperature increases, the oxide layers develop more rapidly. The increase of temperature and thickness in oxide layer can in turn generate a higher hoop stress and strain in the oxide layer as depicted in Figure 4.10(b). This phenomenon was discussed by Evans (1995), where the author explained the stresses and strains developed in oxide layer during the oxidation process were due to two main reasons: (1) the thickening of the oxide layer was constrained by metal substrate, (2) the differences in coefficients of thermal expansion (CTE) between metal and oxide. As the estimation of the oxide scale growth based on the upper band of LMP constant may be too conservative for the investigation, unless stated otherwise, the calculations for the following analyses are mainly based on the mean value of the LMP curve.

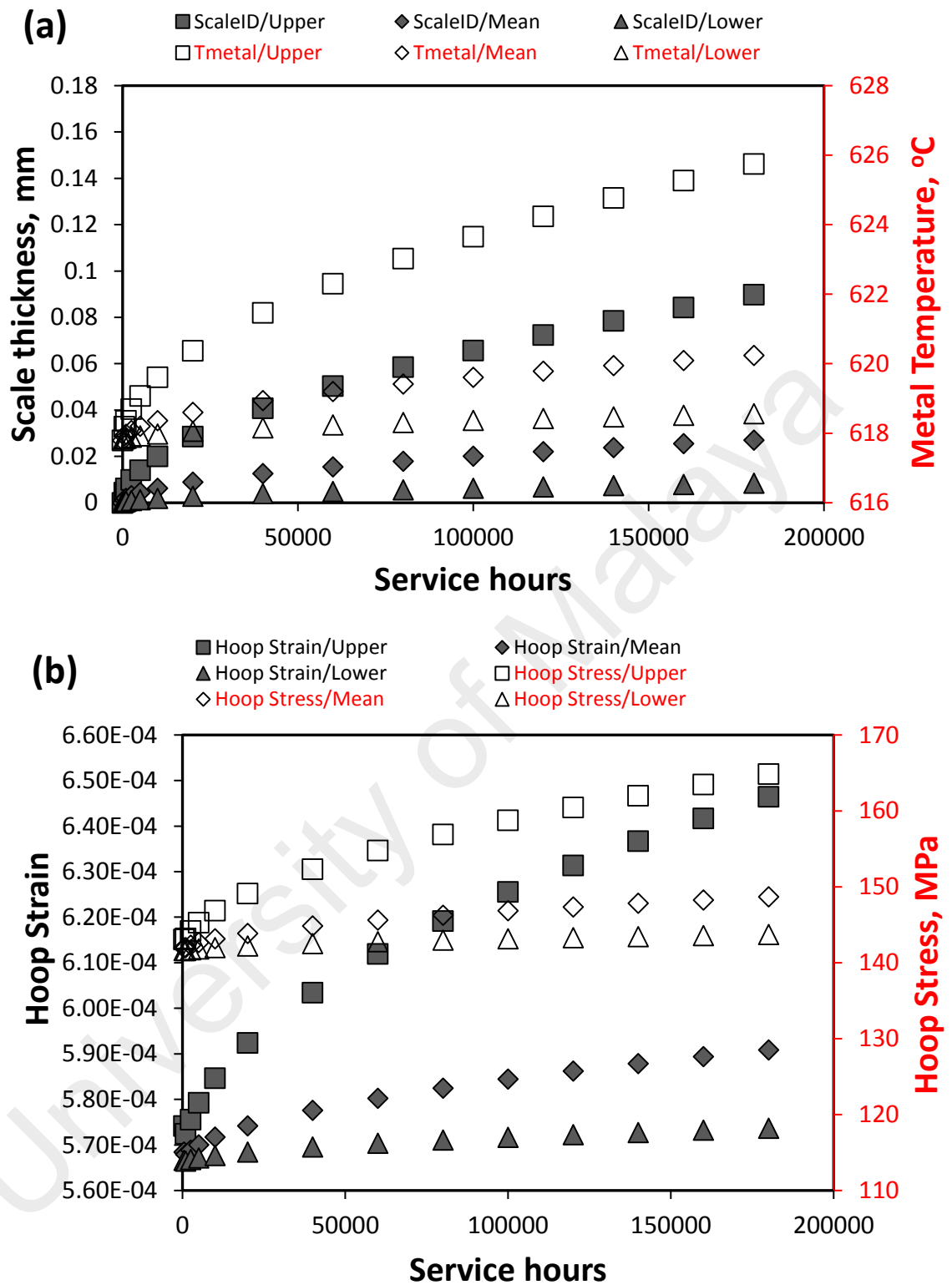


Figure 4.10: Model 1 with austenitic steel (TP347HFG): (a) estimation of oxide scale growth and metal temperature using different LMP fitting constants, (b) hoop stress and strain developed during the oxide growth.

In the literature, Huang et al. (2013), Vikrant et al. (2013), Sabau et al. (2011), Sabau and Wright (2009) and Uerlings et al. (2008) have reported various sizes of tube in their analyses, however, the effect of the different tube size on the oxide scale growth has not been reported and discussed in the any literature. In order to investigate the effect of different tube geometry on the oxide scale growth, Model 2 was selected and compared with 2 other different size of tubes. The original tube (Tube 1) in Model 2 was having outer diameter (OD) of 50 mm with wall thickness (t) of 10 mm. The size of other 2 tubes were stated in Table 3.2. Figure 4.11(a) shows the effect of different size of tubes on the steam-side oxide scale growth and metal temperature, while Figure 4.11(b) shows the associated hoop stress and strain developed in the oxide grown. There are generally no significant differences in the oxide scale growth and metal temperature of those models. However, it is interesting to see that Tube 2, which has bigger inner diameter with smaller tube thickness, is experiencing slightly slower oxide growth as compared to those in Tube 1 and Tube 3. The associated stress strain in the oxide grown in Tube 2 is also observed to be larger than Tube 1 and Tube 3. Typically, the bigger inner diameter with smaller tube thickness results in lower temperature distribution due to better heat flow in the thinner tube. The higher stress strain developed in the Tube 2 can be explained by referring to the hoop stress in Eq. 3.46, whereby the bigger inner radius may contribute to a lower negative term in the hoop stress equation. This results in a higher net value of the hoop stress and strain as compared to those in tubes with smaller inner radius.

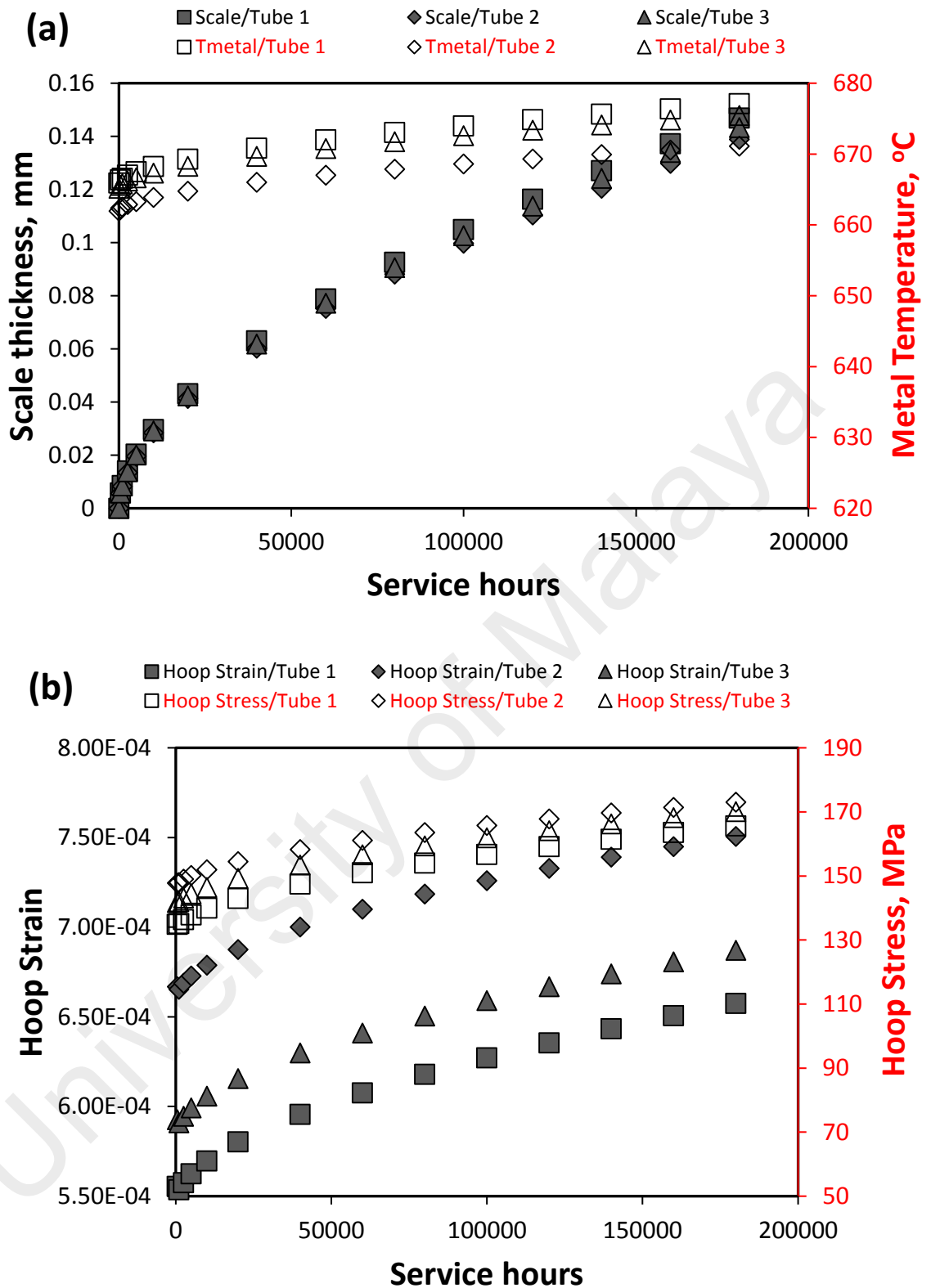


Figure 4.11: Model 2 with different size of tube: (a) estimation of oxide scale growth and metal temperature, (b) hoop stress and strain developed during the oxide growth.

Steam temperature in USC and A-USC boilers are commonly reported to be operating in the range of 597°C-760°C (Wheeldon & Shingledecker, 2013; D. Zhang, 2013). The estimation of oxide scale growth and the metal temperature for Models made of austenitic steel (TP347HFG) under steam temperature ranging from 600°C to 750°C is shown in Figure 4.12(a). It can be observed that most of the oxide scale growths follow parabolic kinetics, except those of Models 3 and 6. The growth rate of Model 3 is initially parabolic up to 40,000 hours in service, then it follows linear rate up to around 180,000 hours. Severe scale growth is also found in Model 6 in which the kinetic rate is already almost linear from the beginning of operations. Similarly, the associated hoop stress and strain developed in same fashion like the oxide scale growth for the corresponding models as depicted in Figure 4.12(b).

University of Malaya

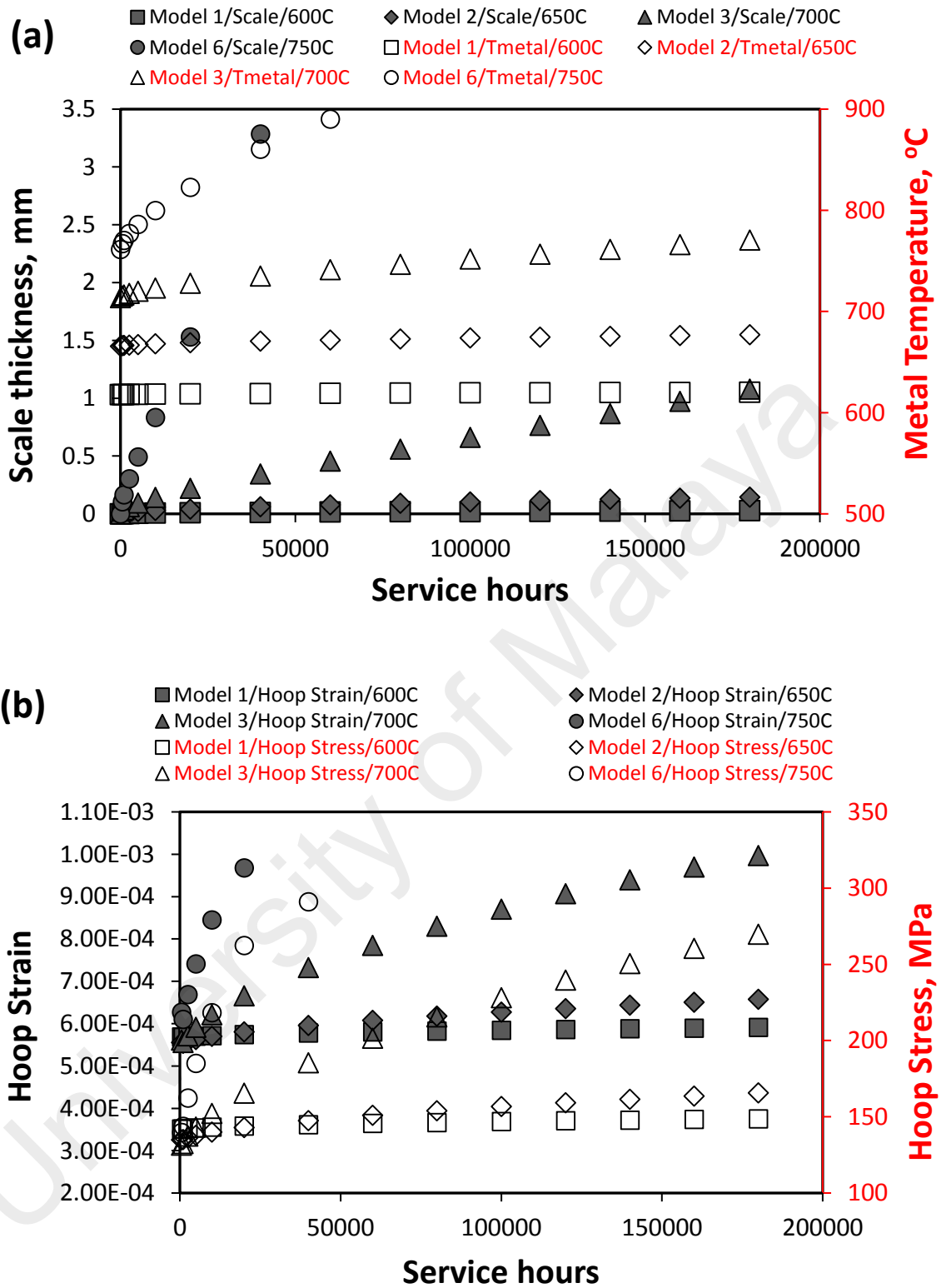


Figure 4.12: Models with austenitic steel working under steam temperature ranging from 600°C to 750°C: (a) estimation of oxide scale growth and metal temperature, (b) hoop stress and strain developed during the oxide growth.

The rapid increase of temperature and thickness in the oxide layer of Models 3 and 6 can result in higher hoop strain accumulated in the oxide layer. This could contribute to the oxide failure and causing the scale detachment from the tube. Figure 4.13 shows the oxide scale failure analysis for the austenitic tube models such as Models 1, 2, 3 and 6. Under the conservative estimation (ϵ_c at $c/d_{ox} = 0.4$), none of the hoop strain developed in the oxide grown will experience scale detachment in Model 1. However, in Model 2, the scale exfoliation could take place at around 60000 hours. As for Models 3 and 6, which have steam temperatures of 700°C and 750°C, the scale detachment could occur in the early stage. For example, Model 3 and 6 could occur, respectively, after 5000 hours and less than 500 hours in service. This may indicate that the use of austenitic steel (TP347HFG) as a material for boiler tubes is only suitable when the steam temperature is around 650°C.

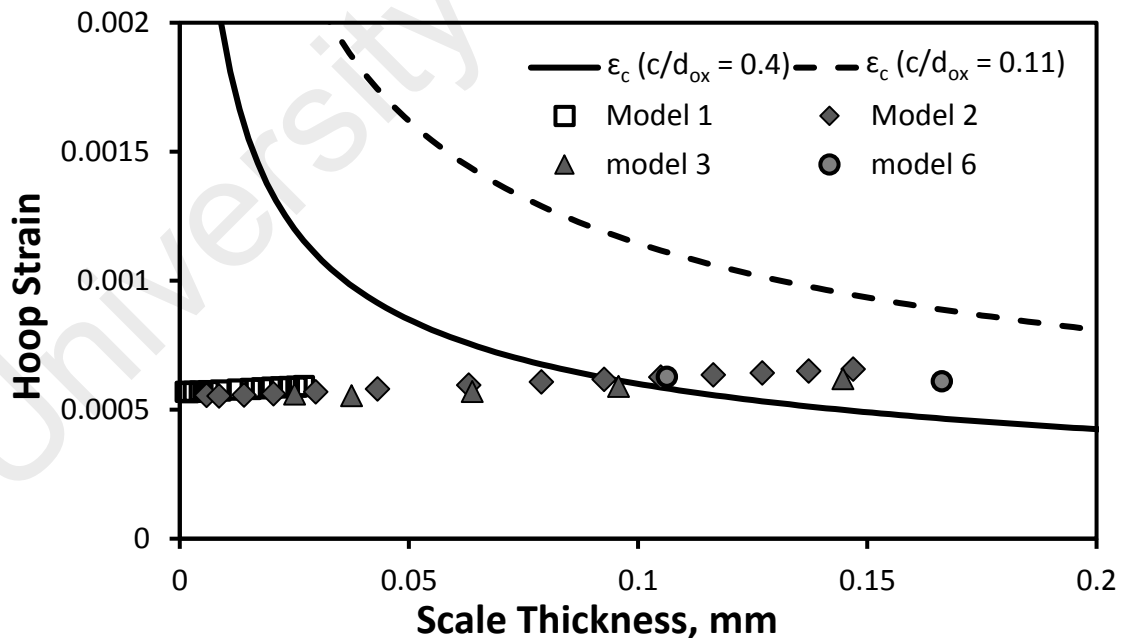


Figure 4.13: Representation of oxide scale failure diagram and evolution of strain in the magnetite (Fe_3O_4) layer formed on austenitic tube under Models 1, 2, 3 and 6.

To further verify the suitable steam temperature range for TP347HFG tube, Figure 4.14 shows estimations of oxide scale growth and metal temperature for Model 3 with austenitic and nickel-based alloys using a more conservative condition (upper band), and to be compared the results under less conservative condition (mean value). Based on upper band condition, the oxide scale growth for Model 3 with austenitic steel initially follows a linear rate at steam environment of 700°C, then followed by hyperbolic rate. However, when nickel-based alloy under the conservative condition (upper band) is used in Model 3, only a very small growth of oxide scale (<0.1mm) is observed. Figure 4.14 implies that the use of nickel-based alloy is preferable for steam condition at 700°C and above. Wheeldon and Shingledecker (2013) and Starr (2014) reported the austenitic steel has inadequate creep strength when exposed to steam temperature at around 680°C in the superheater and reheater tubes. The authors also recommended that the nickel-based alloy should be used for steam temperature 700°C and above. The observation in present work is found in agreement with temperature limit reported by the authors (Starr, 2014; Wheeldon & Shingledecker, 2013). In addition to the limitation of creep strength reported by the authors (Starr, 2014; Wheeldon & Shingledecker, 2013), the present study revealed the aggressive steam-side oxidation at temperature 700°C and above. This may hinder the austenitic steel as a choice of material for boiler tubes, particularly at steam temperature around 700°C and above.

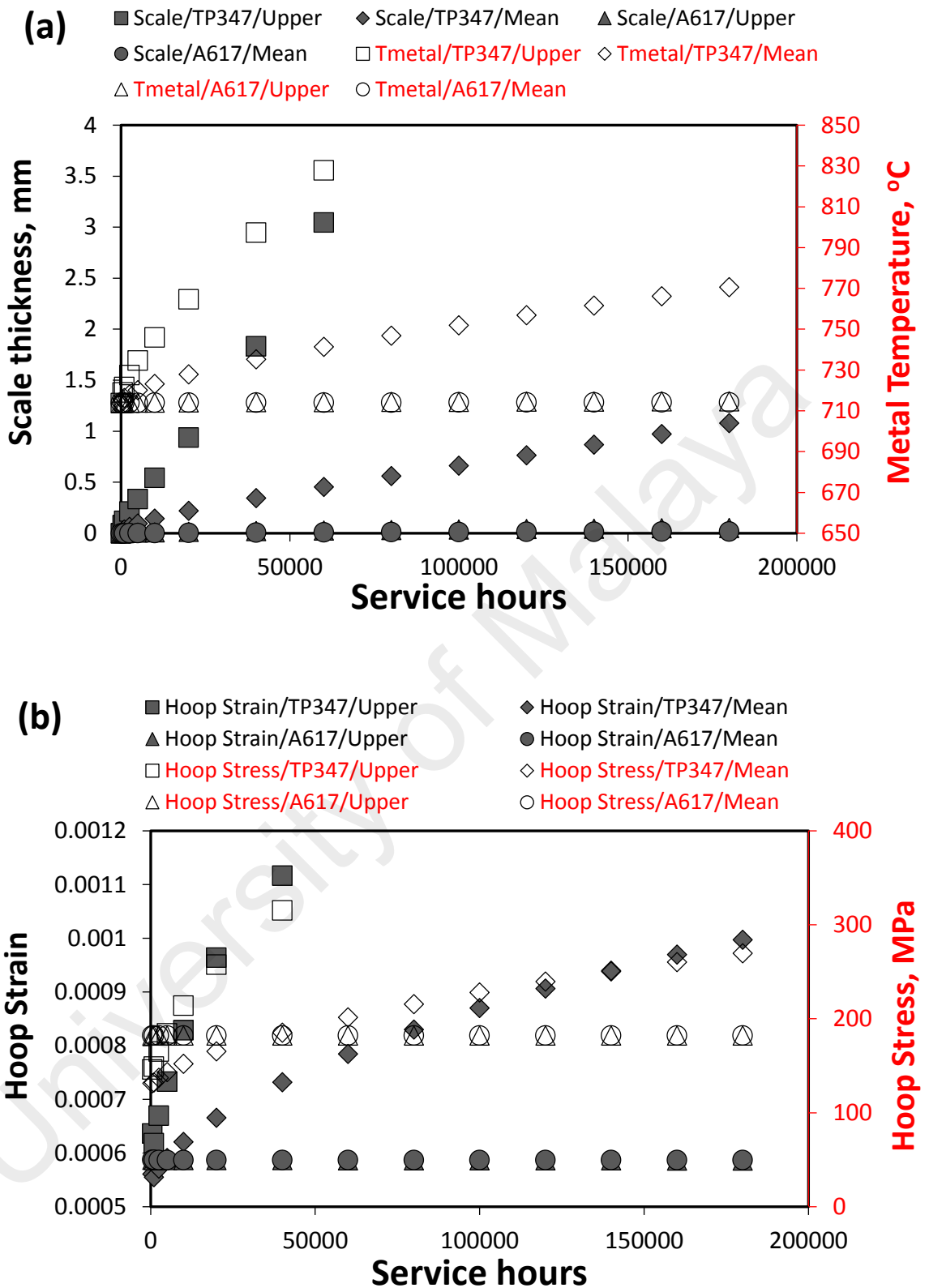


Figure 4.14: Model 3 with austenitic (TP347) and nickel-based alloy (A617): (a) estimation of oxide scale growth and metal temperature using upper band and mean value of C_m in LMP equation, (b) hoop stress and strain developed during the oxide growth.

The estimations of the steam-side growth and temperature increase using upper band condition for the nickel-based Alloy 617 were made at steam conditions of 700°C, 750°C and 800°C and the results are presented in Figure 4.15 to Figure 4.17, respectively. In general, the steam-side scale growths at the 700°C and 750°C steam conditions (Figure 4.15 and Figure 4.16) follow parabolic kinetics. Though the calculations in the present work are designed to be a guide, the estimations for 180,000 h may illustrate tolerable phenomenon with regard to the detrimental aspects of the steam-side oxide formation. Thus, it is not impossible for coal-fired power plants to have more efficient operation by increasing steam temperature to be around 750°C with Ni-based alloys. Careful consideration has to be taken if the plant operators plan to operate steam temperature at 800°C or higher. It can be seen from Figure 4.17(a), though oxide scale growths with a flue gas temperature up to 1200°C follow parabolic rate, the corresponding estimated metal temperatures are higher than 825°C after just 20,000 hours in service. The creep strength of the nickel-based alloys is thus of great concern. Furthermore, if the flue gas temperature is set to 1400°C, the oxide scale growth and the metal temperature increase are shown to be almost linear after a few thousand hours in service.

On the other hand, the development of hoop stress and strain in the oxide scale of models with steam temperature of 700°C and 750°C (as shown in Figure 4.15 and Figure 4.16) are considered to be minor. However, at steam temperature of 800°C, a decreasing trend is observed. This is primarily affected by the change of scale temperature (ΔT_{oxide}) and the change scale thickness (ΔX) in the tube. A correlation function (B) of the oxide scale growth and the temperature increase can be established using the equation of $\Delta T_{oxide} = B\Delta X$.

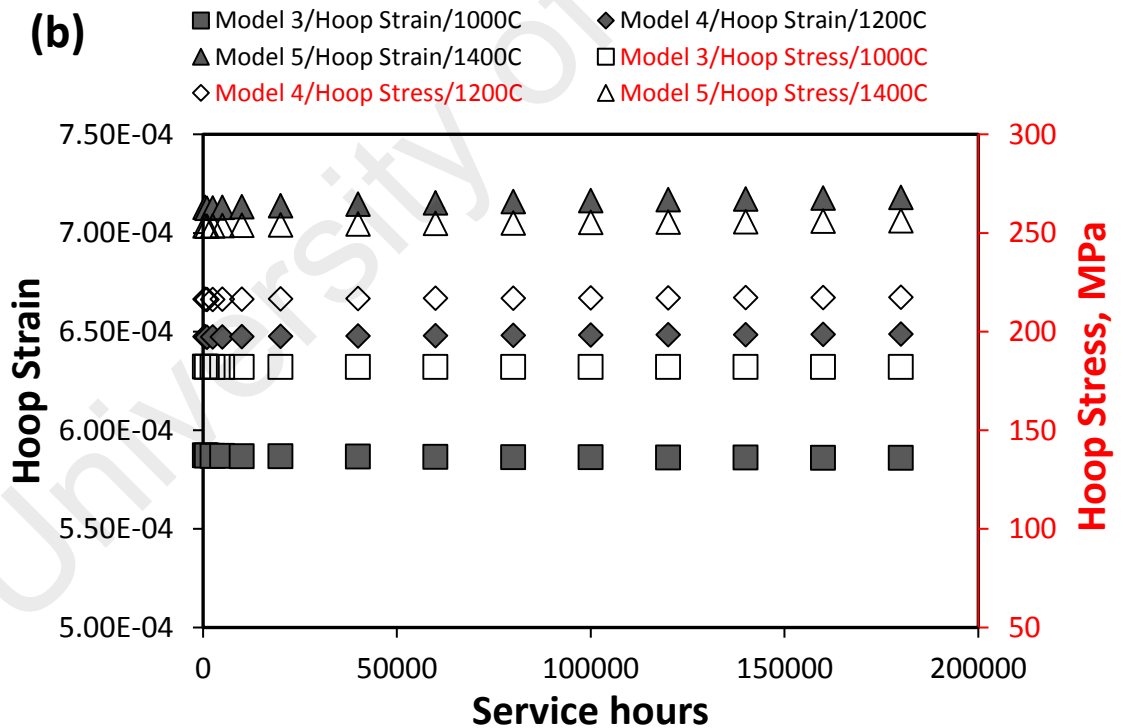
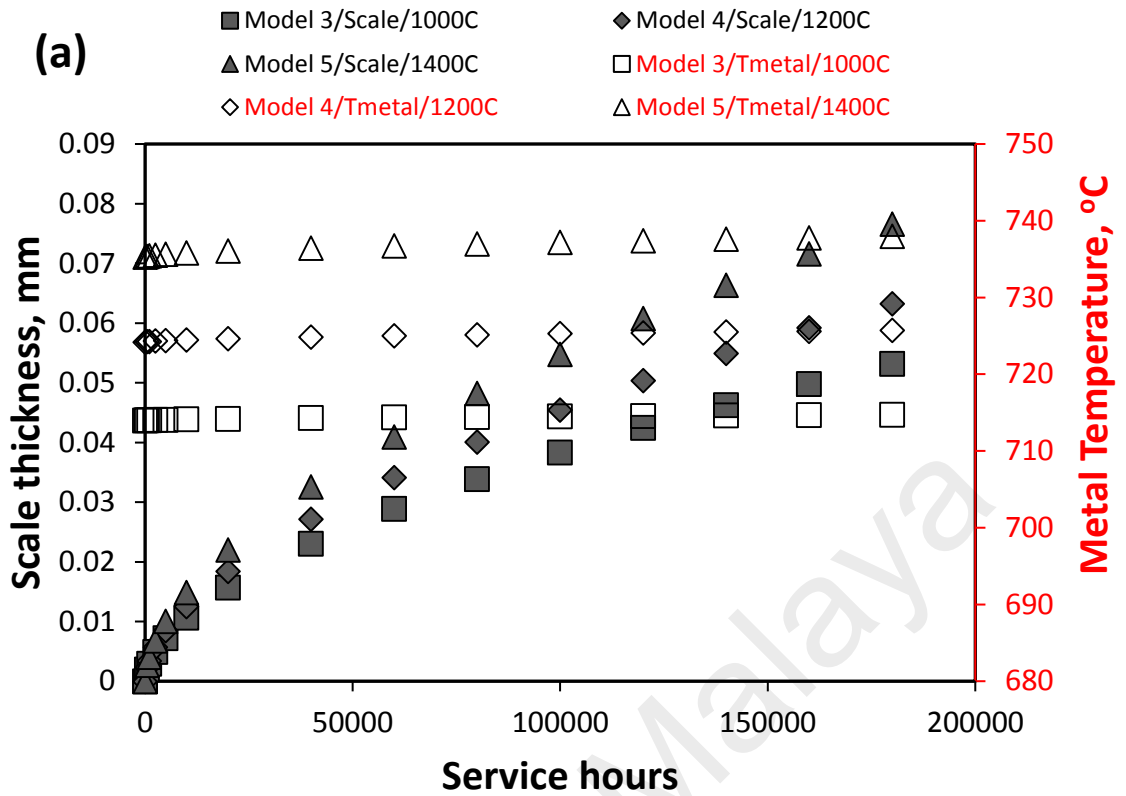


Figure 4.15: Models 3, 4 and 5 with nickel-based alloy (A617) under different flue gas temperatures: (a) estimation of oxide scale growth and metal temperature, (b) hoop stress and strain developed during the oxide growth.

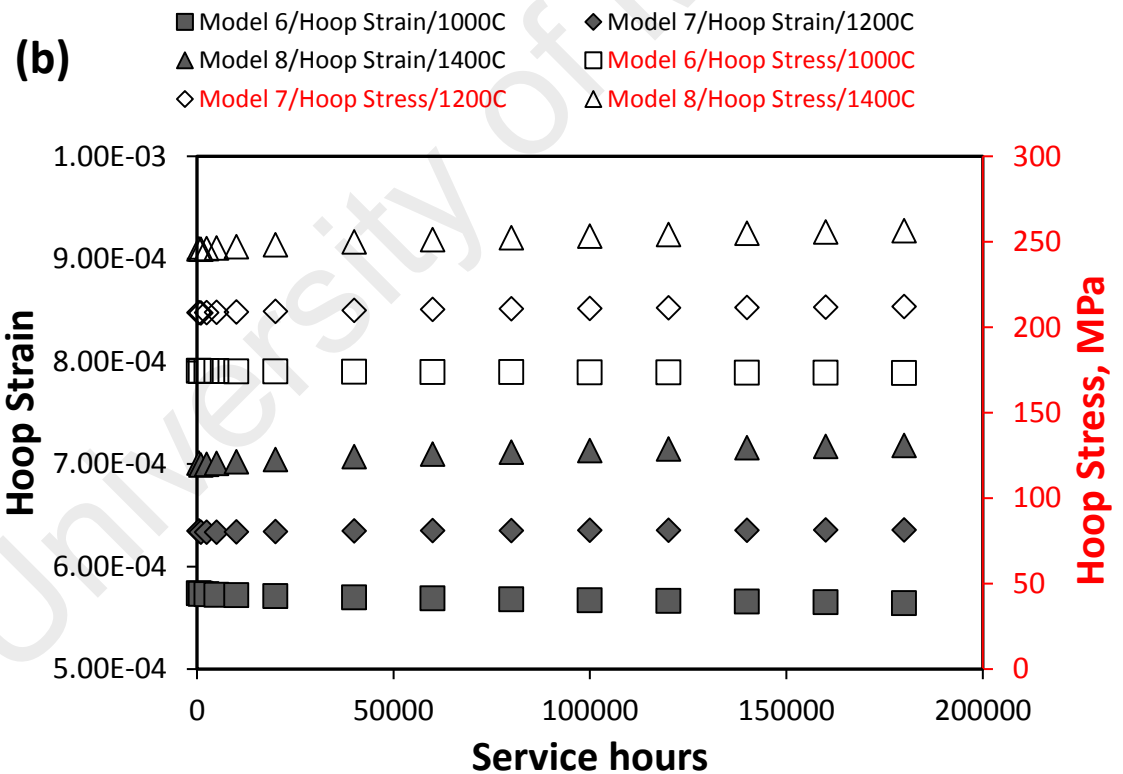
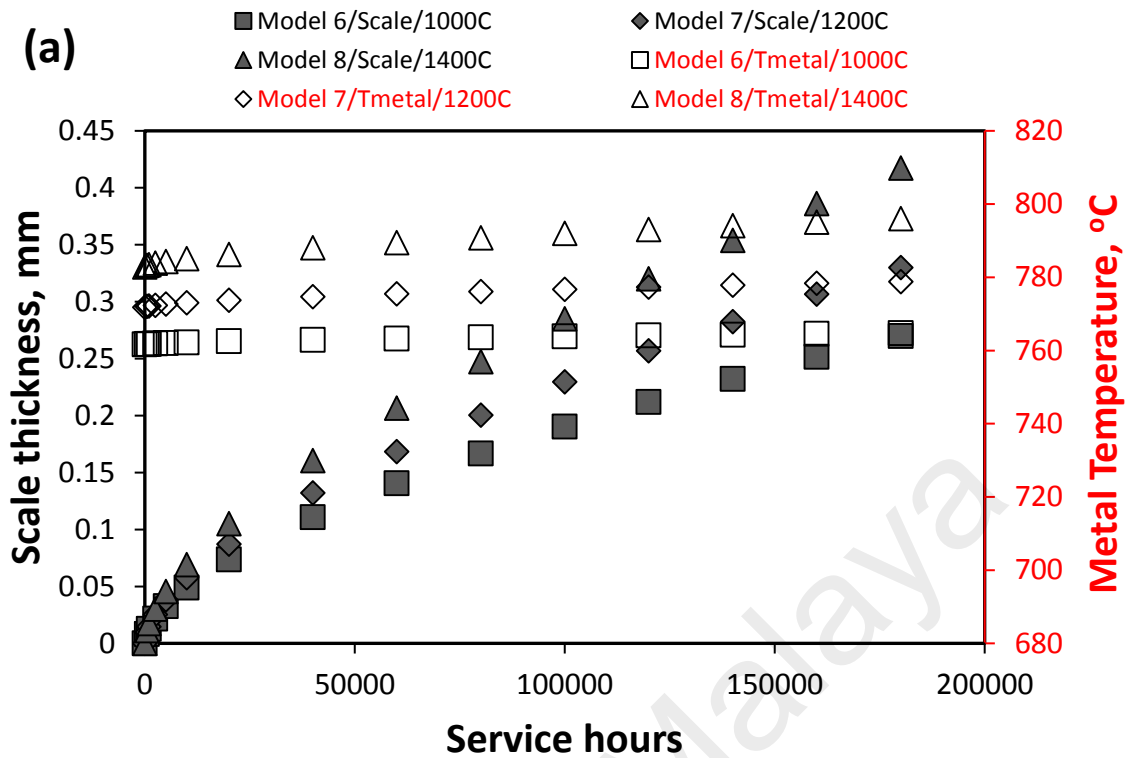


Figure 4.16: Models 6, 7 and 8 with nickel-based alloy (A617) under different flue gas temperatures: (a) estimation of oxide scale growth and metal temperature, (b) hoop stress and strain developed during the oxide growth.

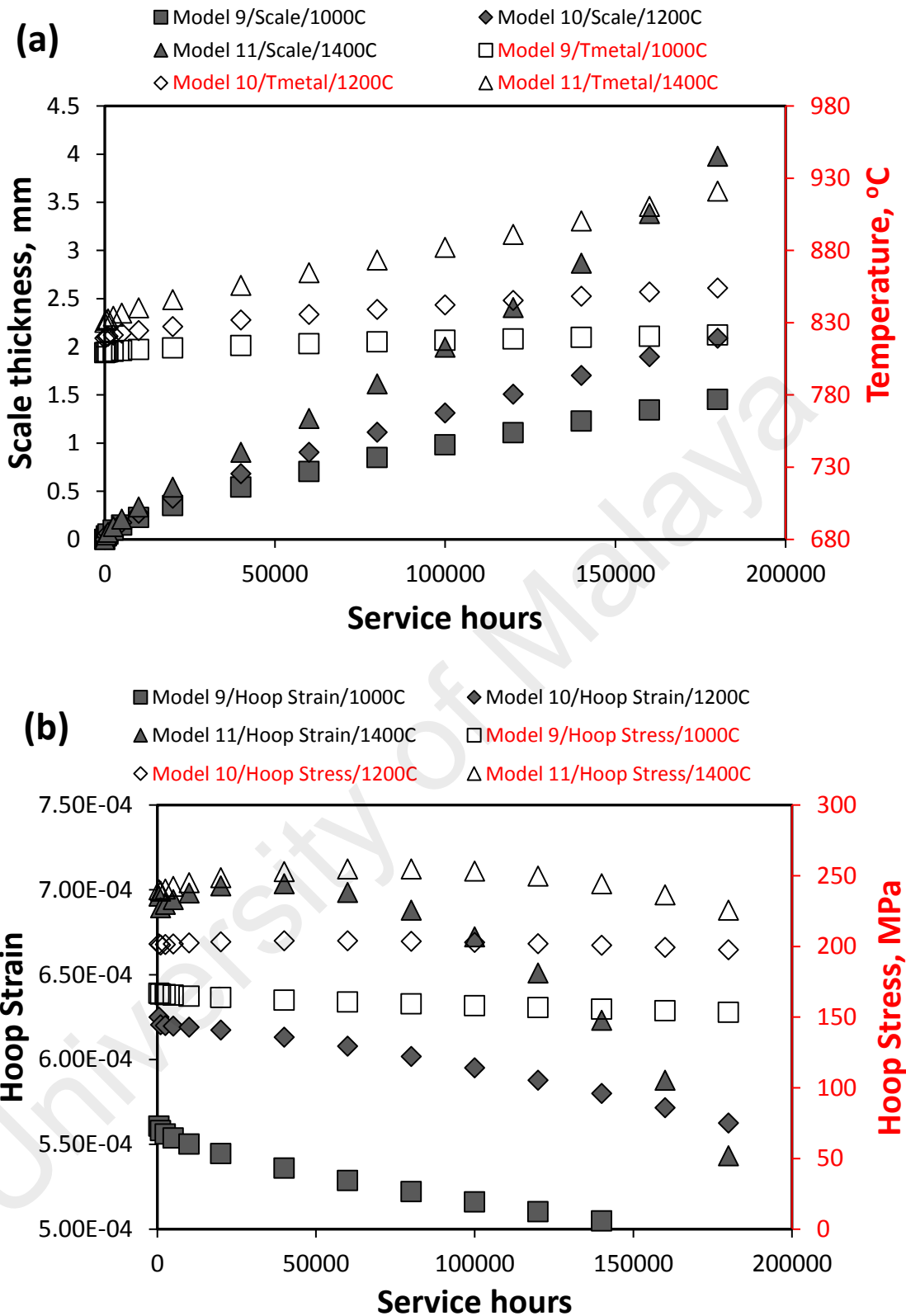


Figure 4.17: Models 9, 10 and 11 with nickel-based alloy (A617) under different flue gas temperature: (a) estimation of oxide scale growth and metal temperature, (b) hoop stress and strain developed during the oxide growth.

A parametric study on different steam and flue gas temperatures has been carried out to determine the correlation functions of all nickel based models reported in Figure 4.15-Figure 4.17. The results tabulated in Table 4.2 imply that the decreasing hoop strain could happen in the oxide when B is less than 10.

Table 4.2: The correlation functions (*B*) of nickel based models

Model no.	Steam temp. (°C)	Flue gas temp. (°C)	Strain behaviour	Constant B
Model 3	700	1000	minor decreasing	6.0852
Model 4	700	1200	minor increasing	12.841
Model 5	700	1400	increasing	18.67
Model 6	750	1000	minor decreasing	7.4345
Model 7	750	1200	minor increasing	11.3
Model 8	750	1400	increasing	16.833
Model 9	800	1000	decreasing	6.0852
Model 10	800	1200	decreasing	4.4414
Model 11	800	1400	increasing until 40000 hours and decreasing after that	17.227 until 40000 hours after that B= 4.2042

Figure 4.18 to Figure 4.20 show estimations of the oxide scale failure in the nickel based alloy (A617) tube. Under conservative estimation, it is observed that the hoop strain developed in the oxide of models with steam temperature of 700°C could be higher than the critical strain at the prolonged operation hours, for examples, Model 4 after 160000 hours and Model 5 after 90000 hours. Under the steam temperature of 750°C, the oxide scale exfoliation in Models 6, 7 and 8 are estimated to occur at around 20000 hours, 10000 hours and 5000 hours, respectively. The rapid growth of scale thickness and temperature change under the steam temperature of 800°C can cause high strains developed in the oxide scale and this could promote the scale exfoliation happen at less than 2500 hours. Under the flue gas temperature of 1400°C (Model 11), the scale exfoliation is estimated to take place as early as 500 hours. Oxide scale exfoliation is an undesirable phenomenon as it is the primary factor for blocking of steam flow that in turn causes overheating of

the superheater/reheater tubes in power plant (Abe, 2014a; Liu, 2015). More simulation studies based on this steam side scale exfoliation are presented in Case D in Section 4.5.

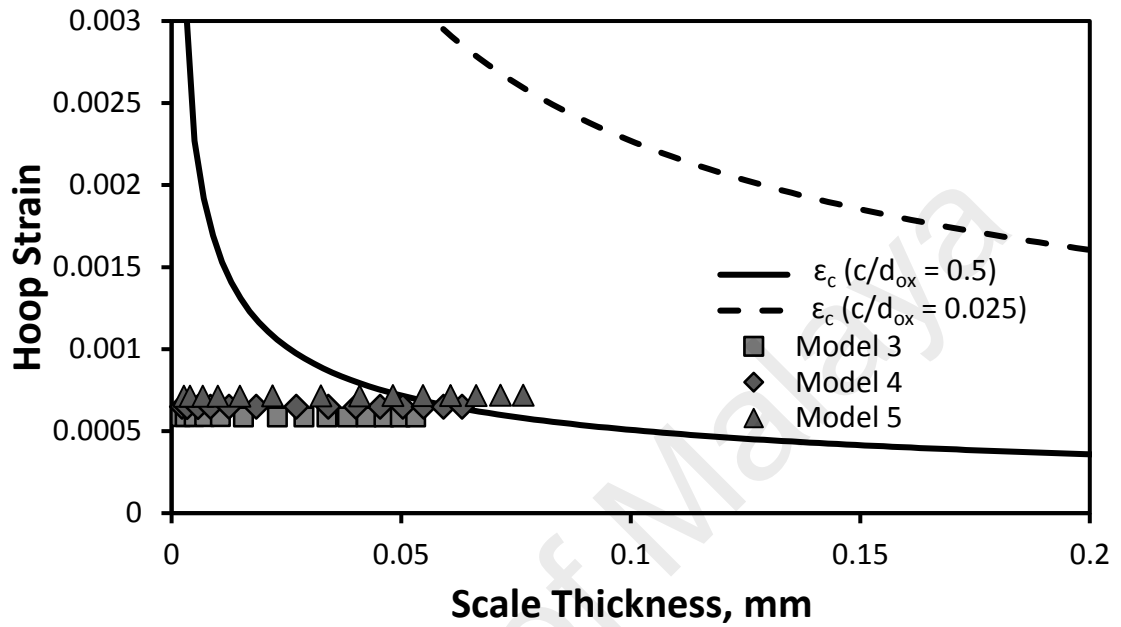


Figure 4.18: Representation of oxide scale failure diagram and evolution of strain in the Cr_2O_3 layer formed on nickel-based alloys tube under the steam temperature of 700°C (Models 3, 4, 5).

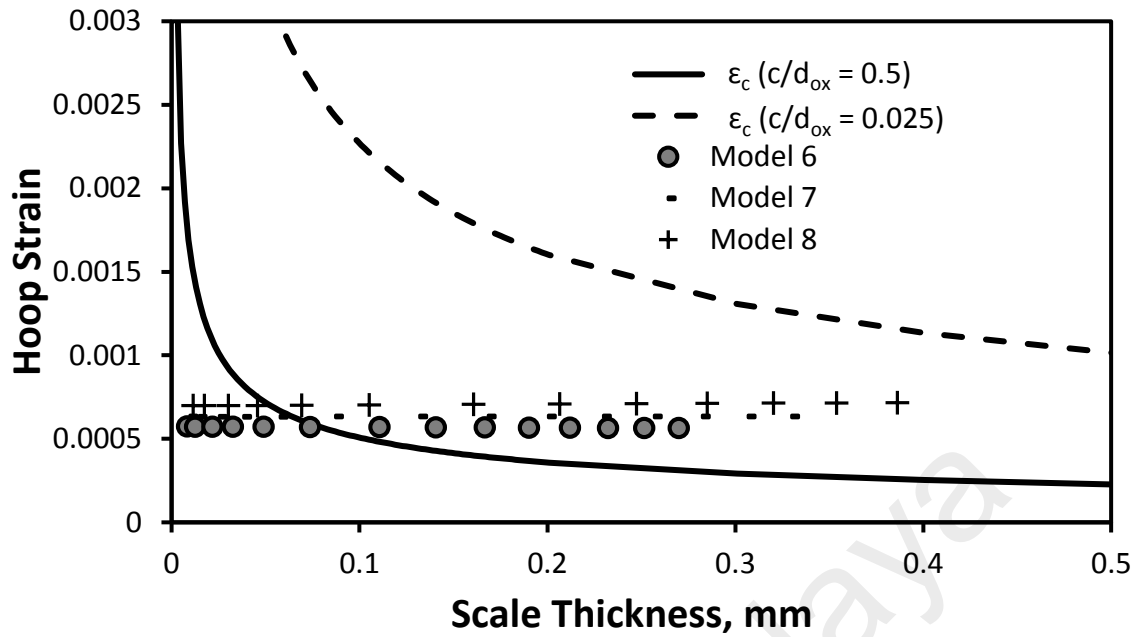


Figure 4.19: Representation of oxide scale failure diagram and evolution of strain in the Cr_2O_3 layer formed on nickel-based alloy tube under the steam temperature of 750°C (Models 6, 7, 8).

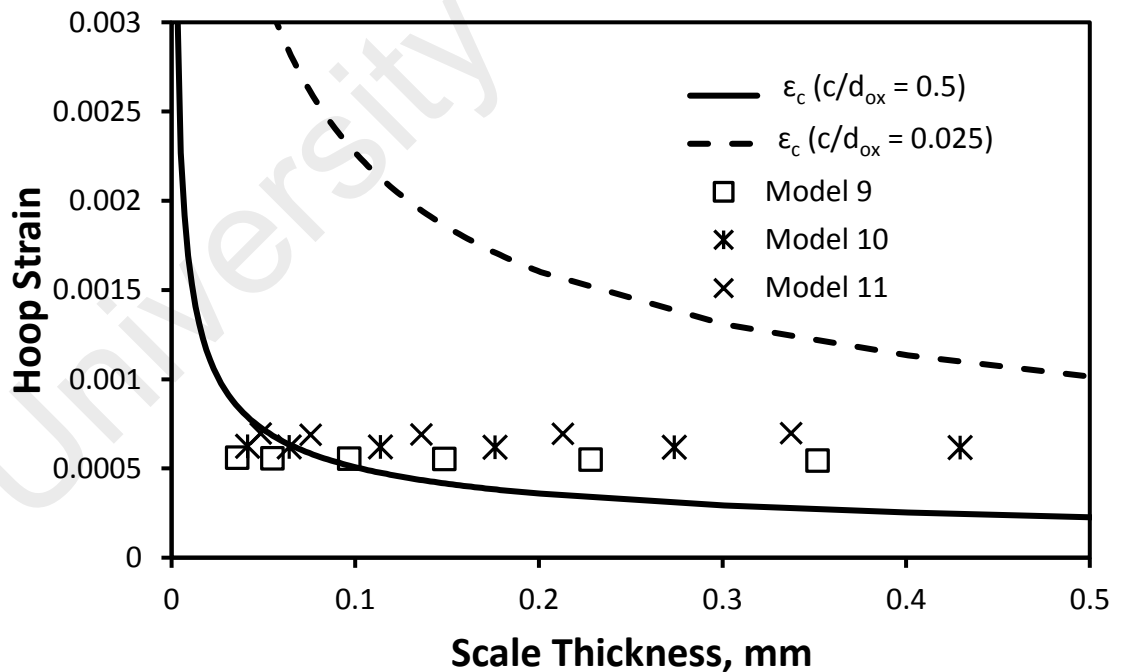


Figure 4.20: Representation of oxide scale failure diagram and evolution of strain in the Cr_2O_3 layer formed on nickel-based alloy tube under the steam temperature of 800°C (Models 9, 10, 11).

4.4 Case B: Growth of both steam-side and fire-side scales

Fireside oxide scale formation in the superheater/reheater tubes is also common phenomenon during service. Adherent fireside scale will however lower the thermal performance of the flue-gas-to-steam heat flow. Figure 4.21(a) depicts the estimations of scale thickness and metal temperatures for Model 2 with austenitic material TP347HFG. Under the conservative estimation, all simulations in this section (Case B) used the upper band of LMP data for the prediction of oxide growth. It can be observed from Figure 4.21(a) that the growth of steam-side/ID scale and the increase of metal temperature in Case B developed slightly faster than those in Case A (without fireside scale). The fireside/OD surface temperature is found to be higher than that in the absence of fireside scale. However, the average metal temperature is shown to be lower. In general, the fireside/OD scales grow more rapidly than the steam-side/ID scales. Failure case studies of boiler tubes as reported by French (1993) also showed that the OD scale of the as-received samples is frequently found to be thicker than the steam-side scale. Furthermore, a failure analysis carried out by Liu (2015) has also reported that the OD scale of the sample, which was close to the burst region, was found to be thicker than the steam-side scale. After 64000 hours of in service, the scale thickness on the steam-side and fireside were reported to be 710 μm and 960 μm , respectively. The traces of OD scales was also detected on the adjacent tube, however, they were found eroded off completely or partially by the flume particles.

For the hoop stress and strain developed in the oxide grown as shown in Figure 4.21(b), it is found that the hoop stress in the OD scale is decreasing and changing from tensile to compressive stress as the OD scale become thicker. This could be attributed to the higher temperature in the OD scale and the decreasing radius of metal-oxide interface.

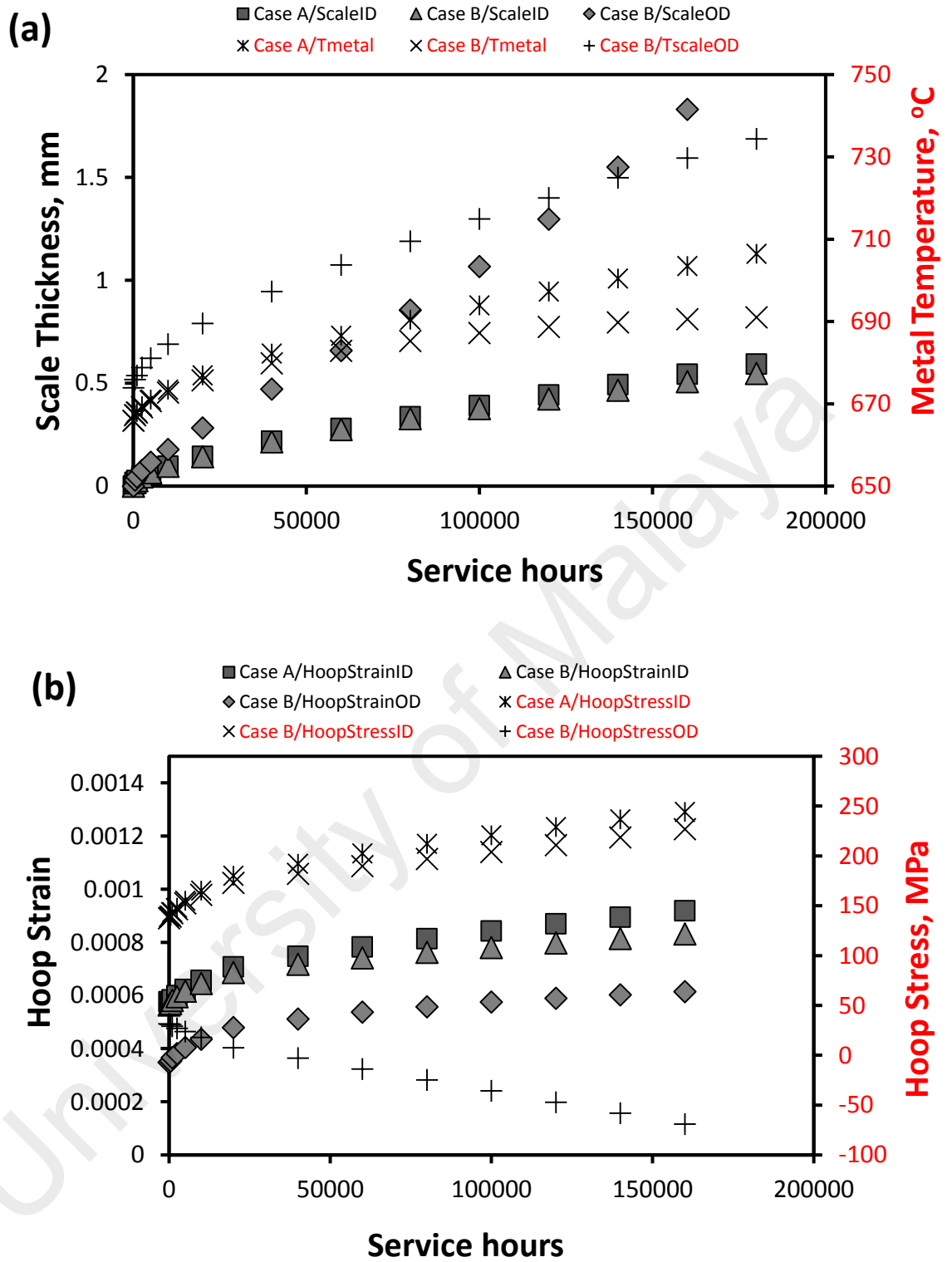


Figure 4.21: Model 2 with (case B) and without (case A) fireside scale: (a) estimation of oxide scale growth and metal temperature, (b) hoop stress and strain developed during the oxide growth.

Figure 4.22(a) shows severe fireside scale growth in the austenitic tube under the steam temperature of 700°C (Model 3). Major portion of the tube wall thickness is lost due to the fireside scale. The rapid fireside scale growth and temperature increase have also resulted in the decrease of hoop stress drastically to compressive state as shown in Figure 4.22(b). It may be observed from the oxide failure diagram shown in Figure 4.23, the ID scale in Model 3 could exfoliate after 500 hours as compared to possible failure of Model 2 at around 10000 hours. The OD scales exfoliation take place at a slight longer hours due to the smaller strain developed in the layer. This may be another reason for which the OD scale is observed to be thicker in the as-received tubes from power plant (French, 1993; Liu, 2015).

University of Malaya

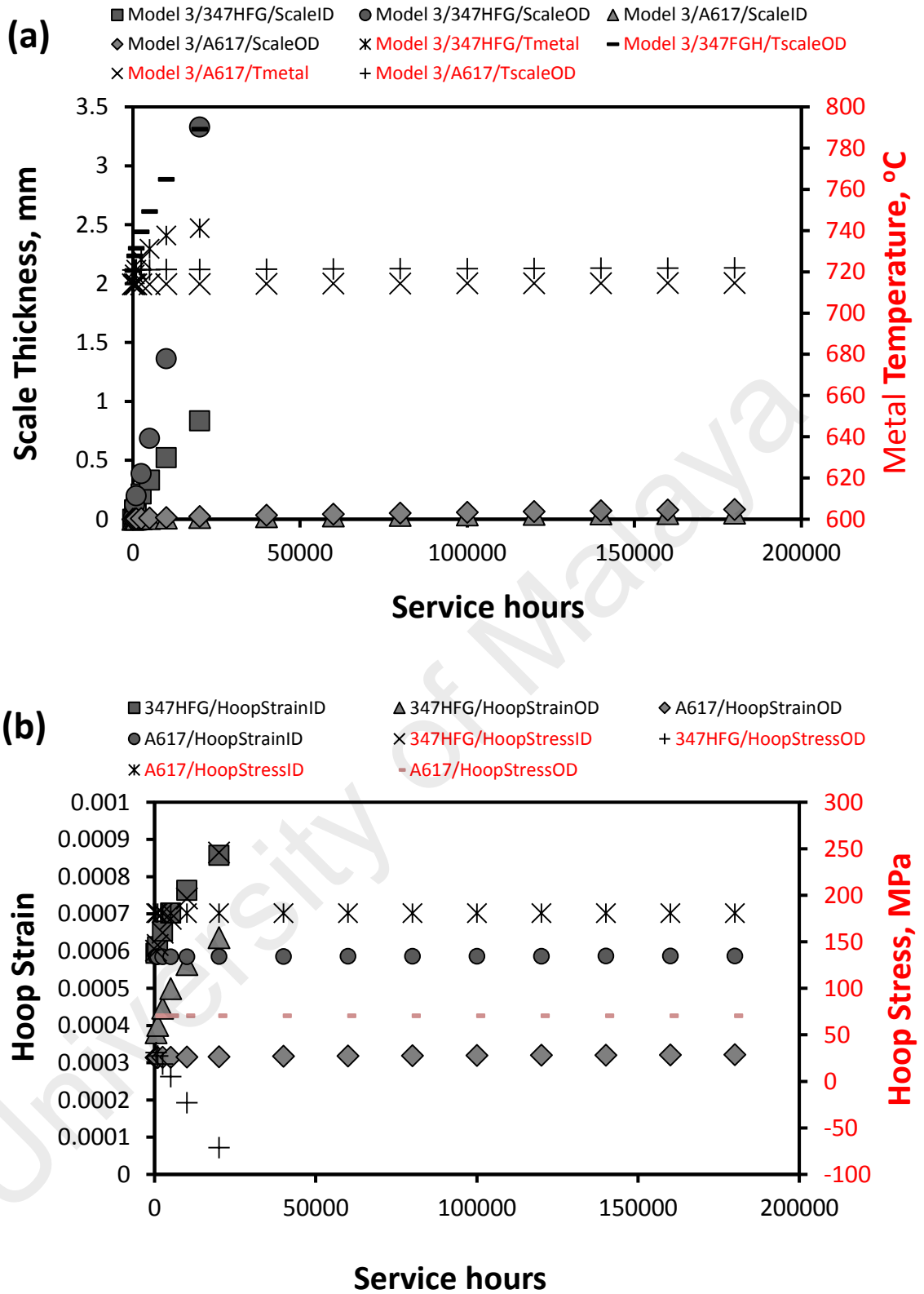


Figure 4.22: Model 3 with austenitic (TP347) and nickel-based alloy (A617): (a) estimation of oxide scale growth and metal temperature, (b) hoop stress and strain developed during the oxide growth.

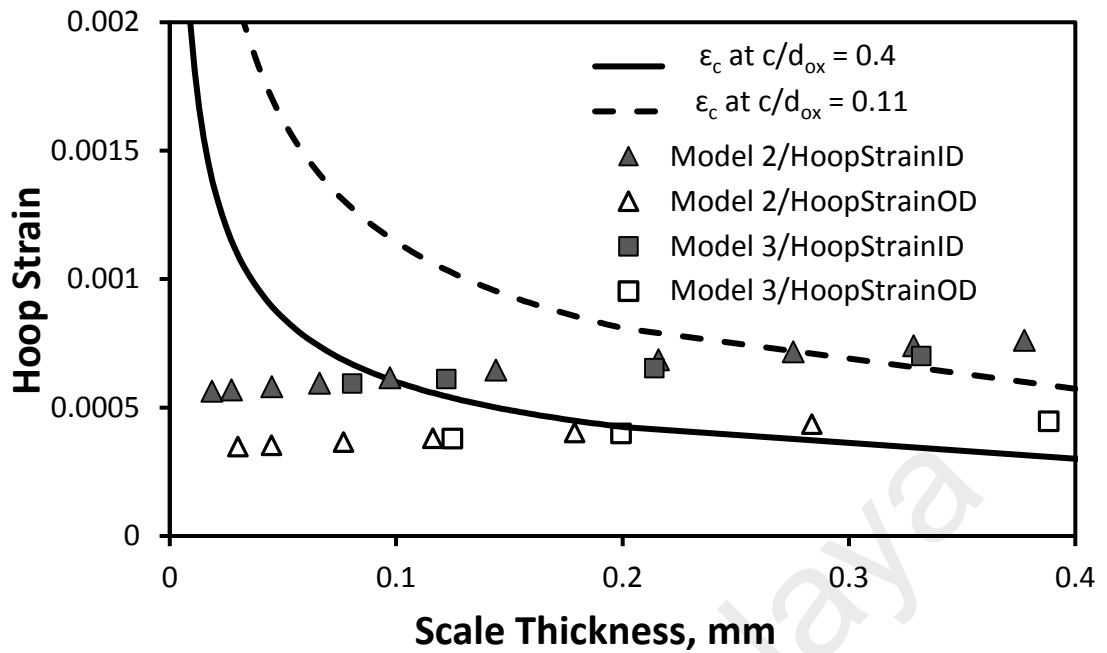


Figure 4.23: Representation of oxide scale failure diagram and evolution of hoop strain in the magnetite (Fe_3O_4) layer formed on inner (ID) and outer diameter (OD) of austenitic tube (Models 2 and 3).

On the other hand, when Ni-based alloy (A617) is used in Model 3, the steam-side and fireside scales are developed more slowly ($<0.1\text{mm}$). The simulation results in Figure 4.22(a) suggest that austenitic steel is not suitable to be used in steam temperature of 700°C as the fireside scale can develop in the hyperbolic rate. The estimations in Figure 4.22 - Figure 4.25 indicate that Ni-based alloy should be considered as the material candidate for boiler tube under the operation steam temperature of 700°C and higher, because the steam-side and fireside scales are growth in the acceptable rate and the associated hoop stress and strain developed during the oxide growth are relatively small.

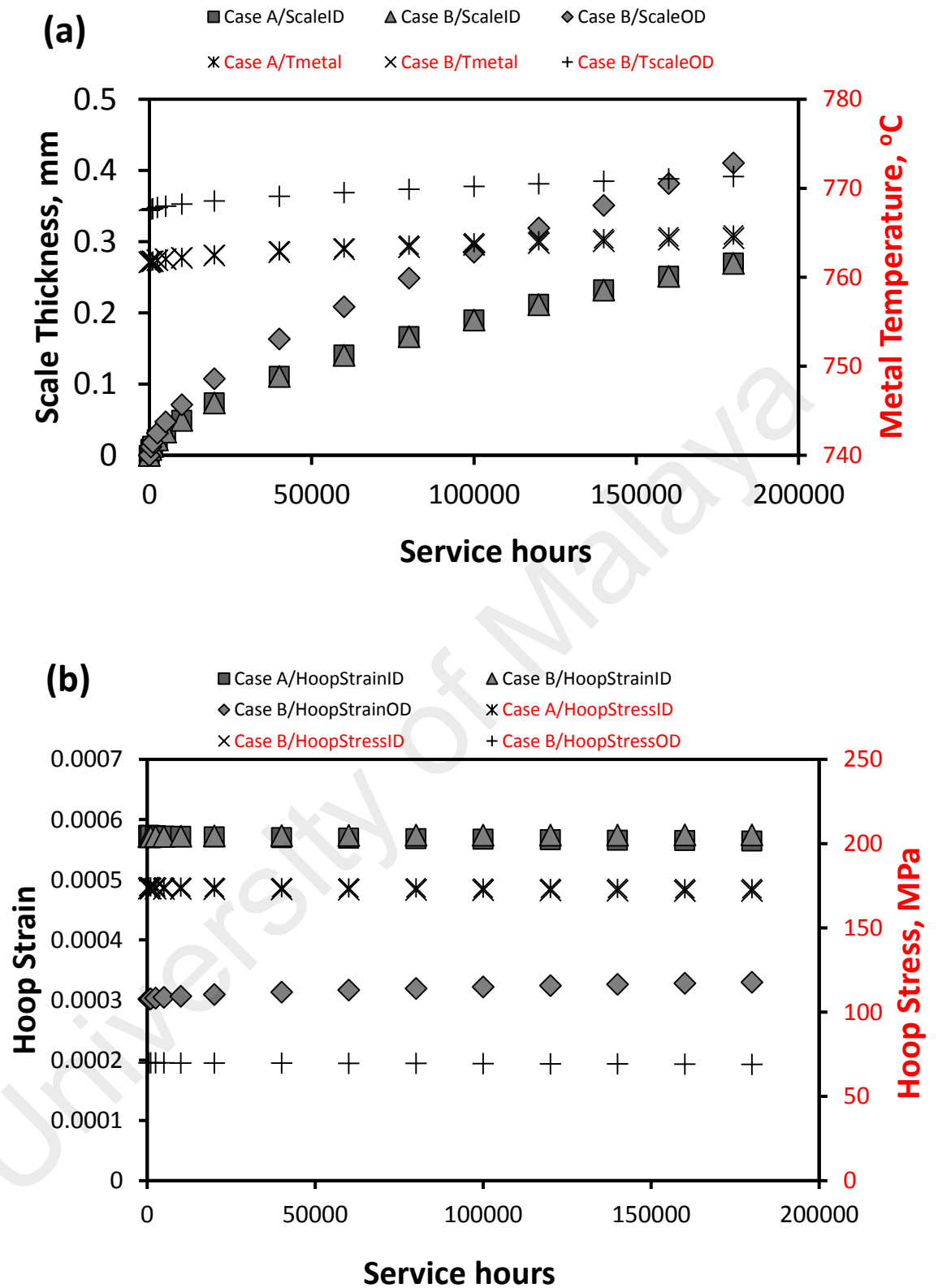


Figure 4.24: Model 6 with Ni-based alloy (A617): (a) estimation of oxide scale growth and metal temperature, (b) hoop stress and strain developed during the oxide growth.

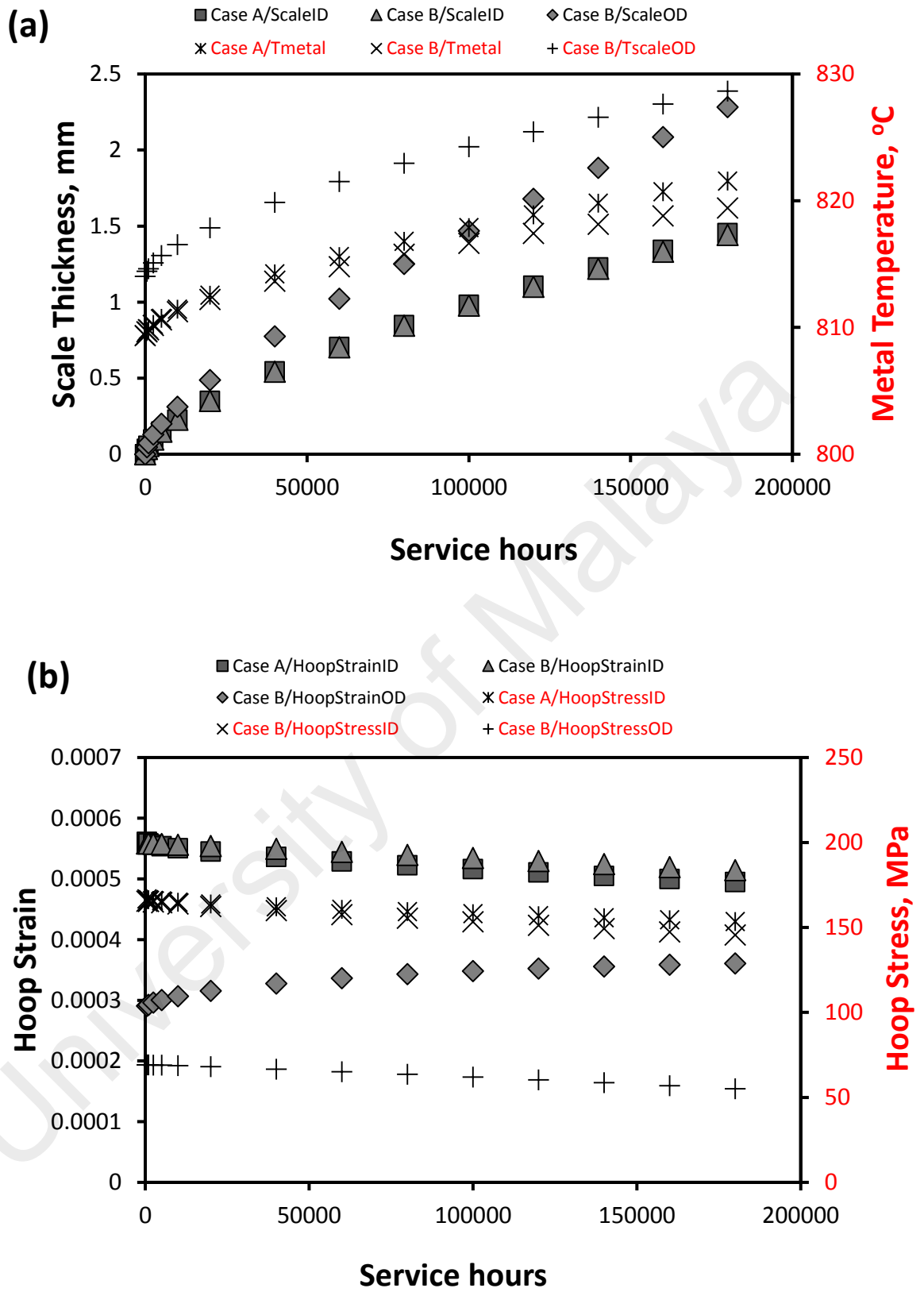


Figure 4.25: Model 9 with Ni-based alloy (A617): (a) estimation of oxide scale growth and metal temperature, (b) hoop stress and strain developed during the oxide growth.

In addition to that, the oxide failure diagram shown in Figure 4.26 also suggests that hoop strain developed in the both ID and OD scales of Model 3 ($T_s = 700^\circ\text{C}$) is below the critical strain. Similar to the models with austenitic steel, it is observed that as a result of the higher strain in the ID scale layer the exfoliation could take place earlier in ID scale as compared to the OD scale. As for steam temperature at 800°C , rapid rate of scale growth in Model 9 is observed to critically trigger the scale failure in less than 2500 hours. Hence, the viability of using nickel based alloy for steam conditions at 800°C and above requires further studies and careful investigations.

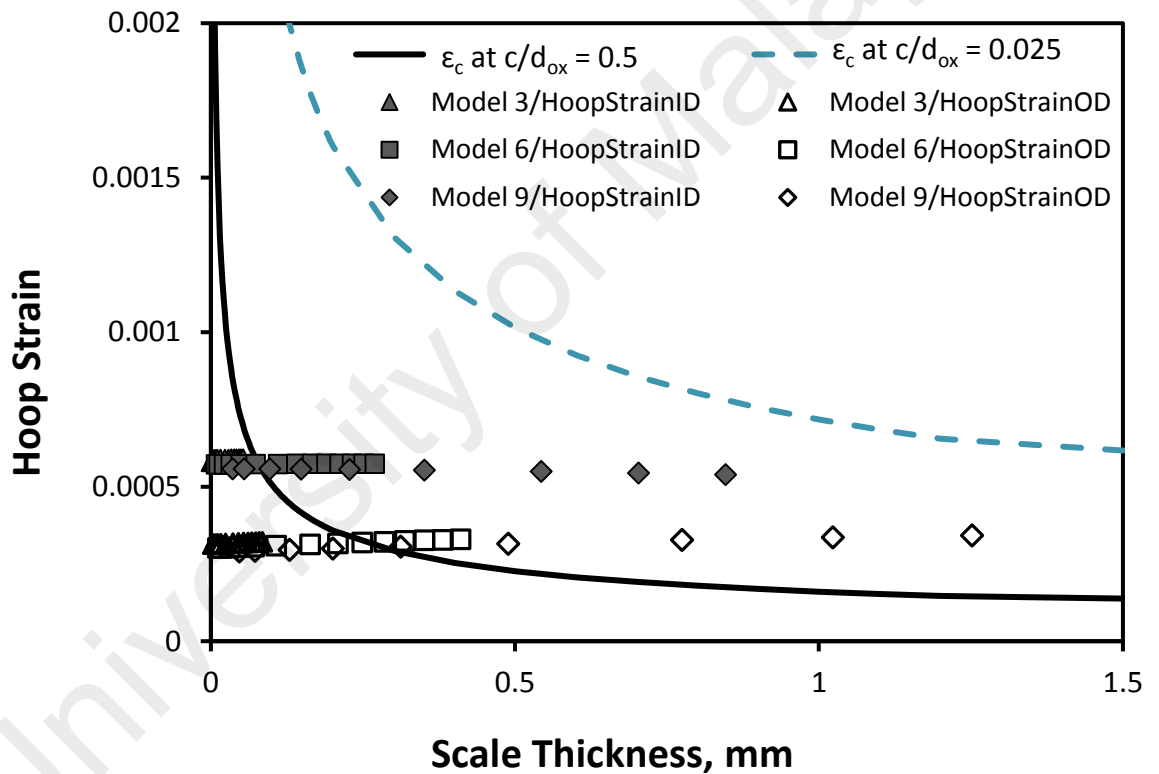


Figure 4.26: Representation of oxide scale failure diagram and evolution of hoop strain in Cr_2O_3 layer formed on inner (ID) and outer diameter (OD) of nickel-based alloy tube under Models 3, 6 and 9.

4.5 Case C: Growth of both steam-side and fireside scales, exfoliation on fireside scale

When the fireside scale becomes thicker and has higher temperature, the exfoliation event is expected. The austenitic steel and Ni-based alloy that have greater difference in coefficient of thermal expansion (CTE) between the oxide and the metal possess the potential for the increased cracking and exfoliation of the scales. Repetition of exfoliation-re-oxidation process could take place during the service, leading to severe wall thinning. In this study, the purpose of simplicity, only the formation of oxides is considered and hot corrosion rates and deposition are neglected.

The proposed method reported here can also be used to demonstrate the exfoliation and re-growth events. Oxide scale re-growth after exfoliation has been discussed by Sabau et al. (2011). Evans and Lobb (1984) described an oxide scale exfoliation process in two scenarios called Route 1 and Route 2. The Route 1 process occurs when the oxide-metal interface is more resistant to rupture compared to the oxide layer itself. At a larger temperature change, the subsequent states of stress and strain energy are relaxed by decohesion at the oxide-metal interface, resulting in a spall particle. Route 2 process arises when the oxide-metal interface has a lower strength than the oxide layer. This process results in progressive buckling and rumpling of the surface film as the decrease of temperature continues, causing the increase of strain between the oxide and the metal. In the following case study, a conservative calculation was made to study the repeated exfoliation-re-oxidation event of fireside scale on austenitic and nickel-based alloy tubes. The spalling event usually occurs when the scale thickness is unable to withstand the increased stress/strain. For the simulations purpose, the exfoliation event is conservatively assumed to occur at every 20,000 hours of the service life. A half-thickness of the scale formation is considered to exfoliate at each event. This presumed condition is primary based on the experience published in the literatures, whereby evidences from

micrographs have suggested the separation of scale are commonly occurred in the middle of the scale structure (Dooley et al., 2007; Quadakkers et al., 2005).

The effect of fireside scale formation and exfoliation on oxide scale growth and metal temperature for TP347HFG & A617 tubes are illustrated in Figure 4.27. In general, it can be noticed that the exfoliation can result in re-oxidation of tube at a more rapid rate. Similar to Case B, the formation of fireside scale behaves like an insulator and lower the heat flow from the flue gas to steam as indicated Figure 4.28. In the case of Ni-based alloy (A617), the fireside scale under the repetition of exfoliation and re-growth is developed at the slower rate at steam temperature of 750°C. Thus, it implies the minimum effect in lowering the heat flow in the tube. Typically, while the fireside scale is adhered, the consequence is not as serious as the damage caused by scale exfoliation that is resulting in wall thinning of tube, causing a serious consequence by elevating hoop stress. As a result, higher hoop stress at higher metal temperatures will increase the likelihood of creep rupture.

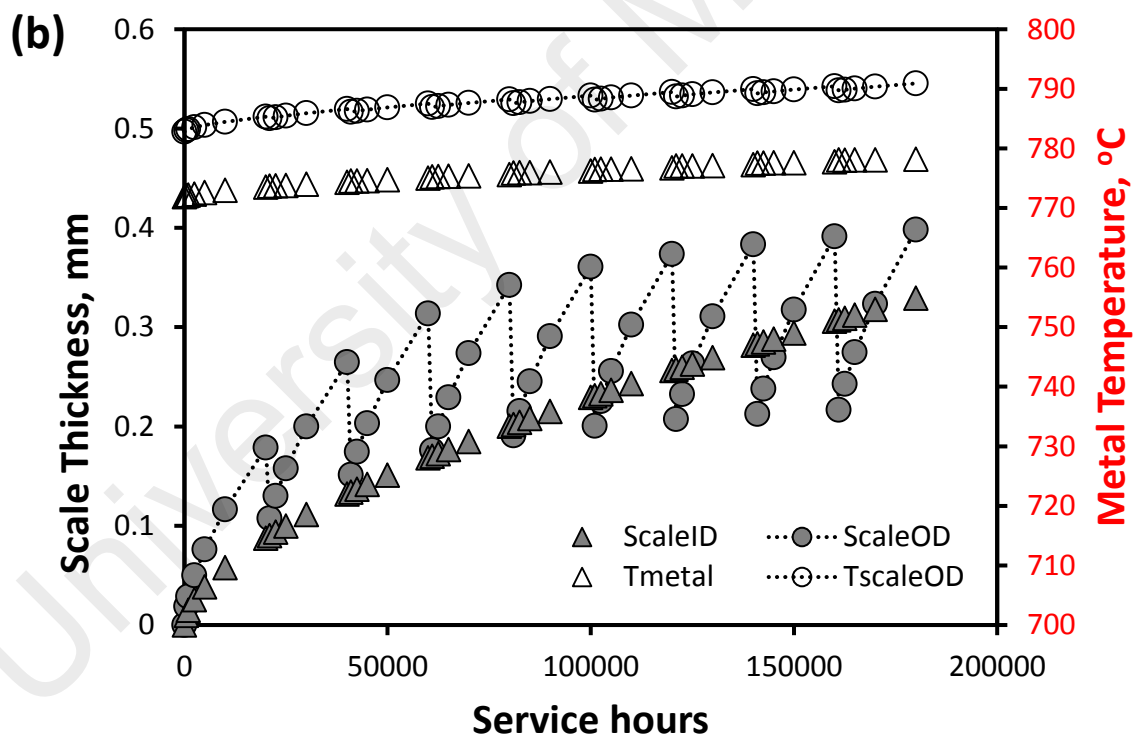
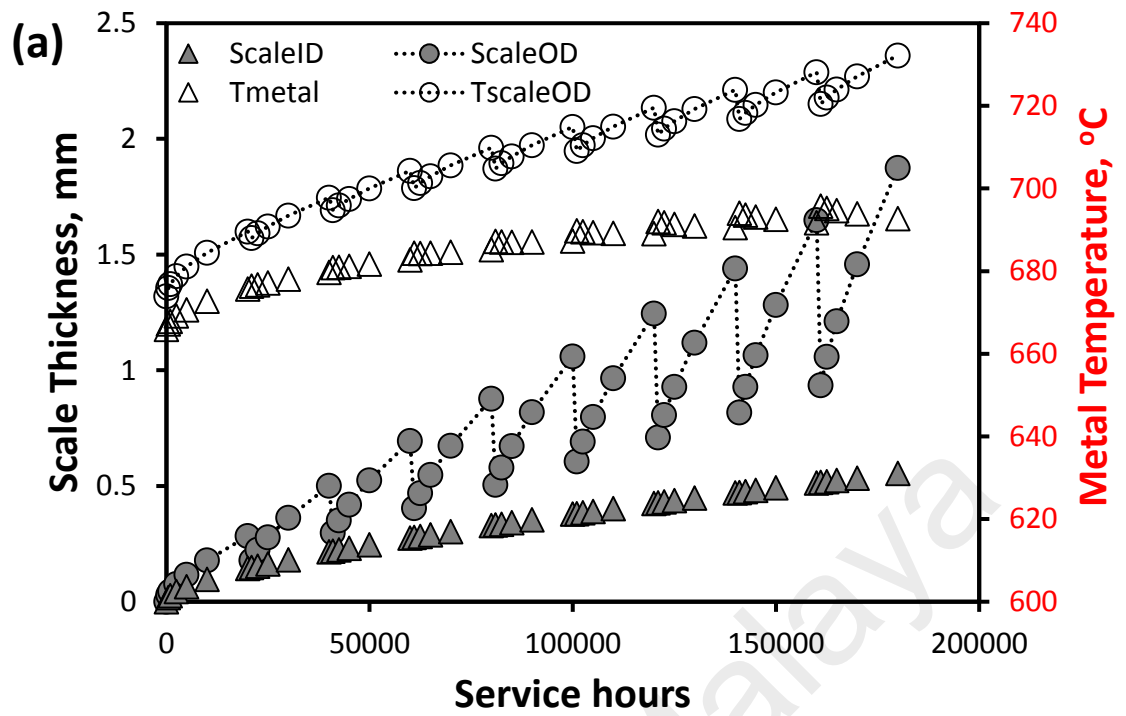


Figure 4.27: Effect of fireside scale formation and exfoliation on oxide scale growth and average metal temperature in (a) Model 2 (austenitic steel, TP347HFG) and (b) Model 7 (Ni-based alloy, A617).

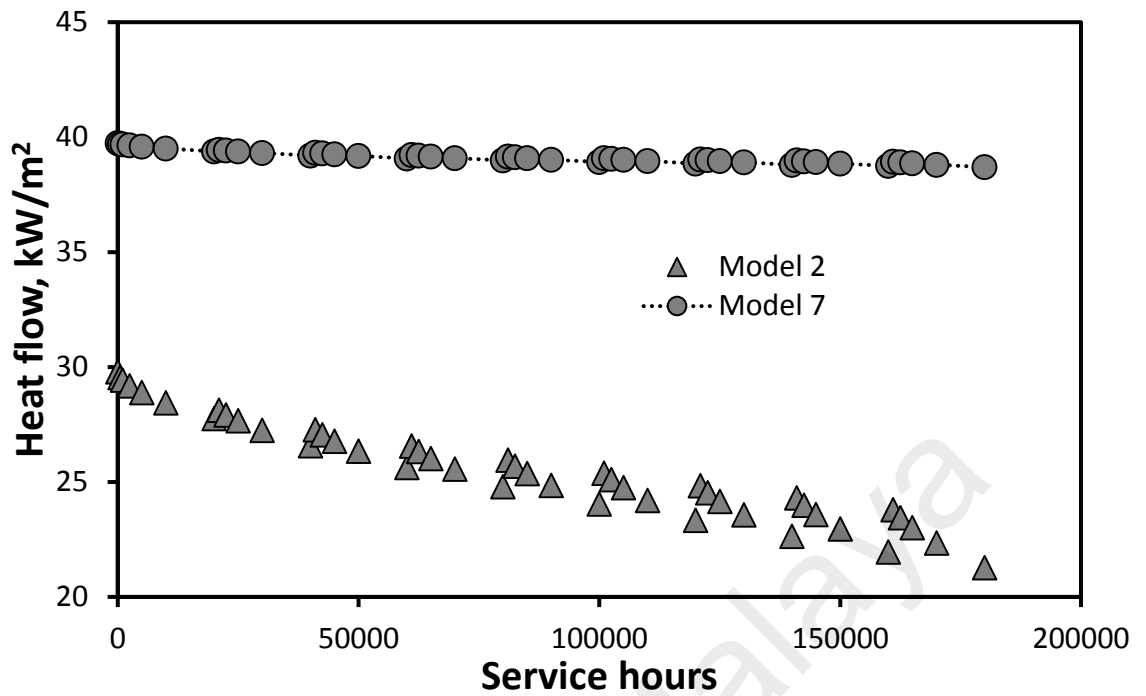


Figure 4.28: Effect of fireside scale formation and exfoliation on heat flow in Models 2 and 7.

4.6 Case D: Growth of both steam-side and fireside scales, exfoliation of steam-side scale

Here, more severe events due to steam-side scale exfoliation are simulated. The exfoliations of the steam-side scale in both ferritic alloys and austenitic stainless steels are associated with the stress-strain in the scale (Wright & Dooley, 2010). Exfoliation could become worse in the advanced steam plants because of the increase oxidation rates due to the operation of higher steam temperatures. The differences in the coefficients of expansions between various scale and the base metal have been identified by a number of researchers as being significant impact on the magnitude of strain acting on the scale when it is cooled (Viswanathan et al., 2006b). Similar to the fireside scale exfoliation in Case C, for simulation purpose, the event is also assumed to have taken place at every 20000 hours in service and half-thickness of the scale formation is also considered to

spall. In this case, the exfoliated materials can collect somewhere in the tube-line to block steam flow. When there are instances of flow restriction, the convective coefficient h_s can drop tremendously. The mass flow rate (\dot{m}) of 1800kg/h and 900kg/h are chosen to illustrate the flow starvation after steam-side exfoliations. Figure 4.29 shows the case of Model 2 with austenitic steel (TP347HFG) at the steam temperature of 650°C, under flow starvation the mass flow rate of 1800kg/h and 900kg/h are equivalent to the convective coefficient of 3604.61 W/m² °C and 2070.30 W/m² °C, respectively. When the flow starvation happened at higher steam temperature of 750°C (Figure 4.30), the mass flow rate of 1800kg/h and 900kg/h are equivalent to the convective coefficient of 3485.39 W/m² °C and 2001.83 W/m² °C, respectively, for the Model 6 with Ni-based alloy A617. The estimations for no flow restriction after spalling are used for comparison. It can be seen from Figure 4.29 and Figure 4.30, when the steam flow experiences massive blockage (e.g. $\dot{m} = 900$ kg/h), the oxide scale grows rapidly. In turn it will substantially elevate the metal temperature. Thus, tube rupture due to short-term overheating is expected. If the flow restriction is quite moderate then the long-term overheating is the predominant case to result in tube rupture. All cases of steam-side exfoliation will threaten the plant availability. The tube wall thinning caused by the steam-side spalling is perhaps not as severe as the case resulting from steam flow restriction. It is widely reported that the detached scales are often very abrasive and can cause erosion in the steam turbine (Holcomb, 2011).

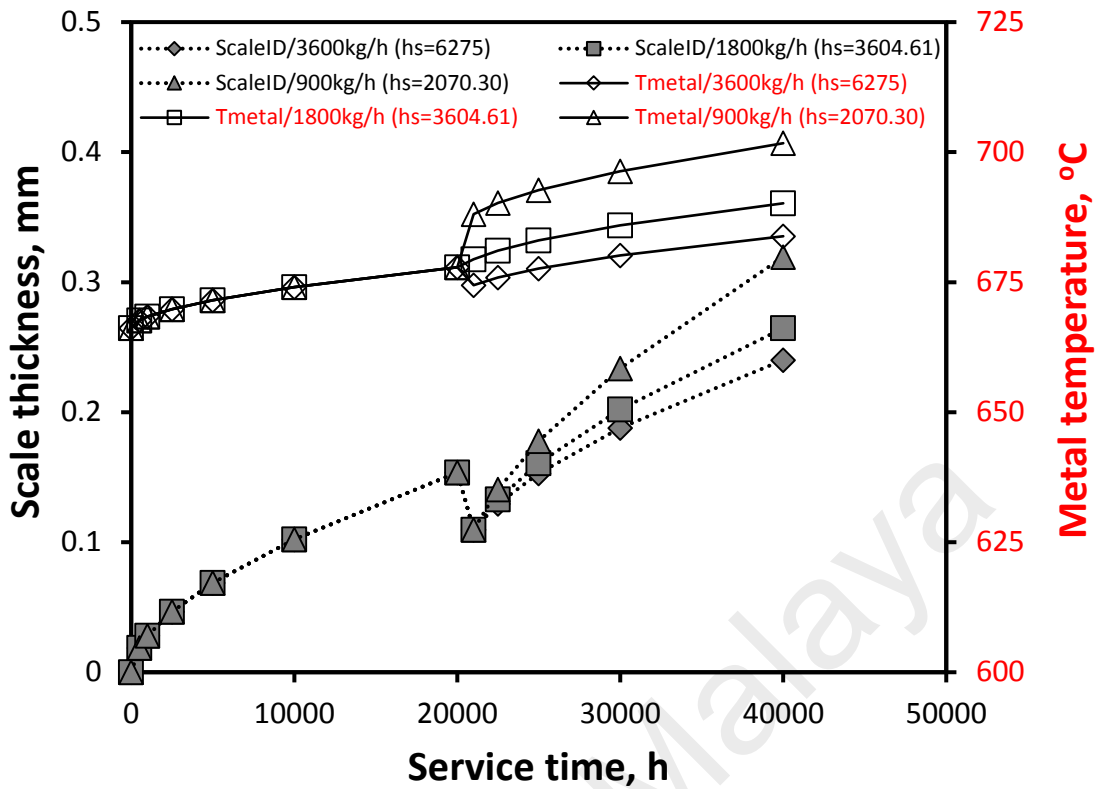


Figure 4.29: The exfoliation and re-growth of the steam-side oxide scale in Model 2 with austenitic steel (TP347HFG) at 650°C steam condition.

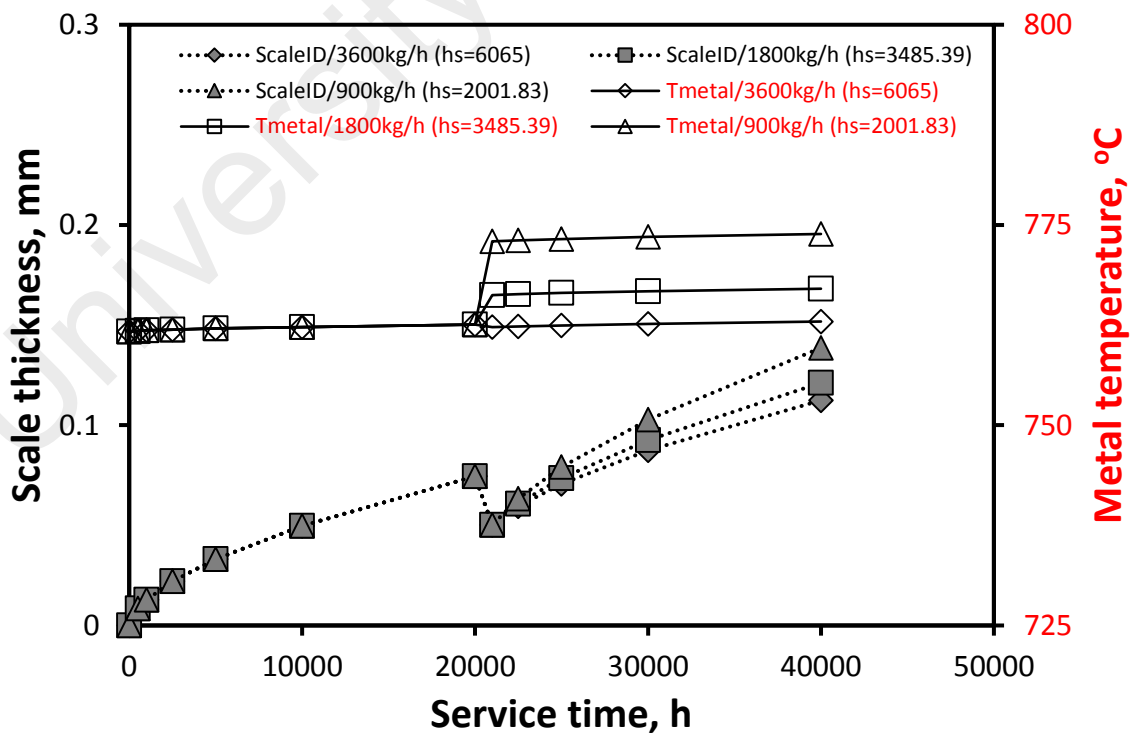


Figure 4.30: The exfoliation and re-growth of the steam-side oxide scale in Model 6 with nickel-based alloy (A617) at 750°C steam condition.

4.7 Summary

In summary, a simple and efficient analytical solution to estimate the thermo-mechanical stress-strain of multi-layered tube has been proposed and verified. Besides that, the iterative procedure to predict scale growth was presented and the results were validated with those collected from power plant. For the estimation of oxide scale exfoliation, an Advance-Oxide Scale Failure Diagram (A-OSFD) based on through scale cracking was used. The required parameters to plot the oxide scale diagrams particularly for the magnetite (Fe_3O_4) and chromium oxide (Cr_2O_3) were obtained by comparing and verifying with the published data in literature. By using the proposed analytical solution and iterative procedure, the implications of oxide scale growth and presumed exfoliation in austenitic and nickel based alloy tube under different assumed service conditions were simulated. From the simulation results, it was found that austenitic steel is suitable to be used for superheater and reheater tubes under operation temperature of around 650°C , while nickel-based alloy should be considered for steam temperature up to 750°C . The use of nickel-based alloys at operation steam temperature of 800°C or higher requires further viability studies and careful consideration, especially with regard to the potential of faster rates of oxidation. Typically, when both steam-side/ID and fireside/OD scales developed on the tube, it was found that the OD scales could develop at the faster rate as compared to those of ID scales. However, the ID scales would experience higher strain than the OD scales. Thus, ID scales were found more susceptible to oxide scale failure as compared to OD scales. The simulation study also revealed that the blockage due to steam-side scale exfoliation could lead to elevation of metal temperature and rapid scale growth in the tube. Next chapter would present more comprehensive conclusions and the suggestions for future work for this research.

CHAPTER 5: CONCLUSIONS AND FUTURE WORK

5.1 Conclusions

The most significant conclusions derived from this work are presented below:

1. A simple and efficient analytical solution to evaluate the thermo-mechanical stress-strain of multi-layered cylinder tube has been proposed. The analytical solution was then incorporated into the proposed iterative method to estimate the development of oxide scales and the thermo-mechanical behaviour of the superheater and reheater tube used in ultra-supercritical (USC) power plant.
2. The scale growth estimations obtained by using the proposed technique have been verified with actual data available in the published literatures, meanwhile the analytical solutions used to evaluate the thermo-mechanical stress-strain for tubes containing oxide scales were compared and verified with those by the finite element analysis software of ANSYS. As compared to other works reported in literature, the analytical solutions proposed in the present work were shown to be more accurate.
3. To predict the oxide scale exfoliation, a method based on Advance-Oxide Scale Failure Diagram (A-OSFD) was used. The required parameters used to establish A-OSFD for magnetite (Fe_3O_4) and chromium oxide (Cr_2O_3) were determined by comparing and verifying with the experimental results reported in literature.
4. Based on the simulations demonstrated in the present work, the implications of oxide scale formation and presumed exfoliation in austenitic and nickel based alloy tube of USC power plants under different assumed service conditions were presented and discussed. Four different cases were considered in this research and their conclusions are as summarised below:

- a) *Case A: Only steamside scale was considered;*

Based on the simulation results, the oxide scale growth rates of austenitic steel (TP347HFG) at steam temperatures of around 650°C were shown to be acceptable in USC operation conditions. The evolution of strains in the oxide scale was found to be increased as the scale thickness was increasing. The oxide scale failure could possibly occur when the strain developed in the scale exceeded a value obtained from the failure criteria at around 60000 hours. Meanwhile, the steam temperatures at 700°C and above, the use of nickel based alloy for superheater and reheater tubing should be considered. The steam-side oxidation rates and the exfoliation of nickel based alloy (A617) at steam temperatures up to 750°C were shown to be allowable in service. Operating steam temperature at 800°C or higher for nickel-based alloys requires further viability studies and careful consideration, especially with regard to the potential of faster rates of oxidation.

b) Case B: Both steamside and fireside scales were considered;

The outer diameter (OD) surface temperature was found to be higher than that in the absence of fireside scale. Besides that, the fireside/OD scales were growing more rapidly than the steam-side/ID scales. However, the hoop strains developed in the OD scales were lower than those in the ID scales. Hence, the oxide failure of OD scales is expected to be slower than the ID scales. This could lead to OD scales often thicker than the ID scales in the tube. In general, the observations in Case B were found to be quite similar to Case A, whereby the austenitic steel (TP347HFG) was observed to be suitable for steam temperatures of around 650°C while the nickel based alloy was found to be appropriate up to for 750°C steam conditions. As for the steam conditions of 800°C and above, further studies and investigations are required.

- c) *Case C: Both steam-side and fireside scales were considered, while exfoliation was assumed on fireside scale;*

This case study was simulated based on the half thickness of the scale to be presumably exfoliated. It was observed that the re-growth of oxide scale on the tube was at faster rate. It was found that the repetition of exfoliation and re-growth of nickel based alloys were found to be at the slower rate than those of the austenitic alloys. The scale exfoliation could lead to serious consequence as the wall thinning of tube can elevate the hoop stress and result in creep rupture.

- d) *Case D: Both steam-side and fireside scales were considered, while exfoliation was assumed on steam-side scale;*

The exfoliated steam-side scales could travel and cause build-ups at the tube bends area and causing blockage of the steam flow. The slower steam flow rates in the tube could lead to the significant elevation of metal temperature and subsequently resulted in rapid scale growth in the tube. This mechanism is often found to be the root cause of long-term overheating and short-term overheating depending on the condition of deposit which could affect the flow rate of the steam. Nevertheless, all cases of steam-side exfoliation will threaten the plant availability.

5.2 Suggestions for future work

Following are some suggestions for further study:

1. Present research revealed the use of nickel-based alloys in reheater/superheater tubing with steam temperature of 800°C could lead to faster rate of oxidation. Since no literature has reported for the use of the materials under 800°C, it would be interesting

to carry an experimental study to further understand the oxidation behavior and temperature limit of the materials.

2. The proposed analytical solutions for thermo-mechanical stress-strain of multi-layered tube in the present work were derived without consideration of creep effect. The incorporation of the creep strain into the proposed analytical solutions can be considered for a more comprehensive investigation.
3. The sudden change of steam temperature due to plant shut down could affect the stress and strain distributions in the tube. An investigation should be carried out to evaluate effect of the steam temperature variation on the strain distribution and possibility of having exfoliations.
4. For simplicity, the oxide scales presented in this work are considered as a single layer, which were magnetite (Fe_3O_4) for austenitic steel and chromium oxide (Cr_2O_3) for nickel-based alloy. Although in some literatures have reported that other traces such hematite or spinel are present in the scales, the understanding on the kinetics of growth behaviors and the morphological development of these oxide materials are insufficient. A simulation study could be carried out to evaluate the effect of the oxide layers treated as a separate layer and intermixed layer which compose of two constituents on the thermo-mechanical behavior of the tube.

REFERENCES

- Abe, F. (2014a). 1 - Grade 91 heat-resistant martensitic steel. In A. Shibli (Ed.), *Coal Power Plant Materials and Life Assessment* (pp. 3-51): Woodhead Publishing.
- Abe, F. (2014b). 9 - Development of creep-resistant steels and alloys for use in power plants. In A. Shirzadi & S. Jackson (Eds.), *Structural Alloys for Power Plants* (pp. 250-293): Woodhead Publishing.
- Armitt, J., Holmes, R., Manning, M. I., Meadowcroft, D. B., & Metcalfe, E. (1978). *The Spalling of Steam-Grown Oxide from Superheater and Reheater Tube Steels*. Palo Alto, CA: EPRI.
- ASTM. (2011). *Standard Specification for Nickel-Chromium-Iron Alloys, Nickel-Chromium-Cobalt-Molybdenum Alloy, and Nickel-Iron-Chromium-Tungsten Alloy Rod, Bar/Plate, Sheet*. West Conshohocken, PA: ASTM International.
- Baker, B. A., & Gollihue, R. A. (2011). *Optimization of INCONEL alloy 740 for advanced ultra supercritical boilers*. Paper presented at the Advances in materials technology for fossil power plants, Santa Fe, New Mexico, USA.
- Beer, J. M. (2007). High efficiency electric power generation: the environmental role. *Progress in Energy Combustion Science*, 33(2), 107-134.
- Dewitte, M., & Stubbe, J. (1986). [Personal communication to D.A. Roberts of G.A. Technologies from Laboretec Company].
- Dooley, R., Wright, I., & TORTORELLI, P. (2007). Program on technology innovation: oxide growth and exfoliation on alloys exposed to steam. *EPRI Report, Palo Alto, CA*.
- Ennis, P. J. (2014). 6 - Nickel-base alloys for advanced power plant components. In A. Shibli (Ed.), *Coal Power Plant Materials and Life Assessment* (pp. 147-167): Woodhead Publishing.
- Eslami, M. R., Hetnarski, m. B., Ignaczak, J., Noda, N., Sumi, N., & Tanigawa, Y. (2013). *Theory of Elasticity and Thermal Stresses: Explanations, Problems and Solutions*: Springer Netherlands.
- Evans, H. E. (1995). Stress effects in high temperature oxidation of metals. *International Materials Reviews*, 40(1), 1-40.

- Evans, H. E., & Lobb, R. C. (1984). Conditions for the initiation of oxide-scale cracking and spallation. *Corrosion Science*, 24(3), 209-222.
- Fleming, A., Maskell, R. V., Buchanan, L. W., & Wilson, T. (2000). *Material Developments for Supercritical Boilers and Pipework*. Paper presented at the Materials for High-Temperature Power Generation and Process Plant Applications, London.
- French, D. (1993). *Metallurgical failures in fossil fired boilers*: John Wiley & Sons.
- Fry, A. (2011). [A personal communication on behalf of the National Physical Laboratory, United Kingdom].
- Fukuda, J. (2011). Development of Advanced Ultra Supercritical Fossil Power Plants in Japan: Materials and High Temperature Corrosion Properties. *Materials Science Forum*, 696, 236-241.
- Ganapathy, V. (2003). *Industrial boilers and heat recovery steam generators: design, applications and calculations*. New York: CRC Press.
- Garrison, W., & Buck, R. F. (1999). *An Overview of the Development of Advanced 9-12% Cr Steels*. Paper presented at the ASM Symposium on Materials for Rotating Machinery, Cincinnati.
- Hay, B., Davee, G., Filts, J.-R., Hameury, J., & Rongione, R. (2009, 29 August – 02 September). *Diffusivity and Thermal Conductivity of Ceramic Coating at High Temperature by Laser Flash Method*. Paper presented at the Thermal Conductivity 30 Thermal Expansion 18, Joint Conferences, Pittsburg, Pennsylvania, USA.
- Henry, J., Zhou, G., & Ward, T. (2007). Lessons from the past: materials-related issues in an ultra-supercritical boiler at Eddystone plant. *Materials at High Temperatures*, 24(4), 249-258.
- Hetnarski, R. B., & Eslami, M. R. (2009). *Thermal Stresses – Advanced Theory and Applications*. Netherlands: Springer
- Holcomb, C., Cramer, S., Covino, B., & Ziomek-Moroz, M. (2005). *Ultra Supercritical Steamside oxidation*. Paper presented at the 4th International Conference on Advance Materials Technology for Fossil Power Plant.
- Holcomb, G. R. (2011). 11 - Steam oxidation in steam boiler and turbine environments. In J. E. Oakey (Ed.), *Power Plant Life Management and Performance Improvement* (pp. 453-489): Woodhead Publishing.

- Huang, J.-L., Zhou, K.-Y., Xu, J.-Q., & Bian, C.-X. (2013). On the failure of steam-side oxide scales in high temperature components of boilers during unsteady thermal processes. *Journal of Loss Prevention in the Process Industries*, 26(1), 22-31.
- Incropera, F. P. (2011). *Introduction to heat transfer*: John Wiley & Sons.
- Janna, W. (2009). *Engineering heat transfer*: Boca Raton : CRC Press.
- Khanna, A. S. (2002). *Introduction to High Temperature Oxidation and Corrosion*: ASM International.
- Klöwer, J., Husemann, R., & Bader, M. (2013). Development of nickel alloys based on alloy 617 for components in 700 C power plants. *Procedia Engineering*, 55, 226-231.
- Kritzer, P. (2004). Corrosion in high-temperature and supercritical water and aqueous solutions: a review. . *The Journal of Supercritical Fluids*, 29(1-2), 1-29.
- Liu, W. (2015). The dynamic creep rupture of a secondary superheater tube in a 43 MW coal-fired boiler by the decarburization and multilayer oxide scale buildup on both sides. *Engineering Failure Analysis*, 53, 1-14.
- Lu, K. (2010). The future of metals. *Science*, 328, 319.
- Mäenpää, L., Klauke, F., Tigges, K. D., Matsuda, J., Kukoski, A., & Gaffoor, A. (2009). *Material Aspects of a 700C Power Plant*. Paper presented at the Third Symposium on Heat Resistant Steels and Alloys for High Efficiency USC Power Plants, Tsukuba, Japan.
- Masuyama, F. (2001). History of power plants and progress in heat resistant steels. *ISIJ*, 41, 612-525.
- Masuyama, F. (2011). *R&D Program for A-USC material development with creep strength/degradation assessment studies*. Paper presented at the Advances in materials technology for fossil power plants, Santa Fe, New Mexico, USA.
- Matsuo, H., Nishiyama, Y., & Yamadera, T. (2005). *Steam Oxidation of Fine-Grain Steels*. Paper presented at the Advances in Materials Technology for Fossil Power Plants.
- Meyer, H., Erdmann, D., Moser, P., & Polenz, S. (2008). KOMET 650 –Coal-fired Power Stations with Steam Temperatures up to 650 °C. *VGB Power Tech-International Journal for Electricity and Heat Generation*, 3, 36-42.

- Montgomery, M., Hansson, A. N., Vilhelmsen, T., & Jensen, S. A. (2012). Steam oxidation of X20CrMoV121: Comparison of laboratory exposures and in-situ exposure in power plants. *Materials and Corrosion*, 63, 674-684.
- Nagl, M. M., & Evans, W. T. (1993). The mechanical failure of oxide scales under tensile or compressive load. *Journal of Materials Science*, 28(23), 6247–6260.
- NiDL. (2014). High-Temperature High Strength Nickel Base Alloy, 393. from Nickel Development Institute www.nickelinstitute.org
- Nishiyama, Y., Hayaso, Y., & Otsuka, N. (2003). *Corrosion Resistant Boiler Tube Materials for Advanced Coal Fired Steam Generating Systems*. Paper presented at the Proc. of the 28th International Conference on Coal Utilization, Clearwater, FL.
- Osgerby, S., & Fry, A. (2003). [Simulating steam oxidation of high temperature plant under laboratory conditions: practice and interpretation of data].
- Paterson, S. R., Moser, R., & Rettig, T. R. (1992). Proc. International Conference on Interaction of Iron-Based Materials with Water and Steam. In R. B. Dooley & A. Bursik (Eds.), (pp. 8.1-8.5): EPRI
- Paterson, S. R., & Rettig, T. W. (1987). Remaining Life Estimation of Boiler Pressure Parts – 2-1/4Cr-1Mo Superheater and Reheater Tubes: Electric Power Research Institute.
- Pettinau, A., Ferrara, F., & Amorino, C. (2012). Techno-economic comparison between different technologies for a CCS power generation plant integrated with a subbituminous coal mine in Italy. *Applied Energy*, 99, 32-39.
- Picque, B., Bouchard, P. O., Montmitonnet, P., & Picard, M. (2006). Mechanical behaviour of iron oxide scale: experimental and numerical study. *Wear*, 260(3), 231-242.
- Purbolaksono, J., Khinani, A., Rashid, A. Z., Ali, A. A., Ahmad, J., & Nordin, N. F. (2009). A new method for estimating heat flux in superheater and reheater tubes. *Nuclear Engineering and Design*, 239(10), 1879-1884.
- Quadackers, W. J., Ennis, P. J., Zurek, J., & Michalik, M. (2005). Steam oxidation of ferritic steels – laboratory test kinetic data. *Materials at High Temperatures*, 22(1-2), 47-60.
- Rehn, I. M., & Abplett, W. (1981). Corrosion Problems in Coal-Fired Boiler Superheater and Reheater Tubes. Palo Alto, CA: EPRI.

- Robertson, J., & Manning, M. I. (1990). Limits of adherence of oxide scales. *Materials Science and Technology*, 6(1), 81-92.
- Rudolphi, M., & Schütze, M. (2013). Investigations for the Validation of the Defect Based Scale Failure Diagrams—Part I: Nickel Oxide. *Oxidation of metals*, 79(1-2), 167-177.
- Sabau, A. S., Shingledecker, J. P., & Wright, I. G. (2011). *Steam-side oxide scale exfoliation behavior in superheaters and reheaters: differences in the behavior of alloys T22, T91, and TP347 based on computer simulation results*. Paper presented at the Advances in materials technology for fossil power plants, Santa Fe, New Mexico, USA
- Sabau, A. S., & Wright, I. G. (2009). On the estimation of thermal strains developed during oxide growth. *Journal of Applied Physics*, 106(2), 023503.
- Salzgitter. (2008). Data Sheet: Boiler Grade DMV 304 HCu from Salzgitter Mannesmann Stainless Tubes GmbH www.smst-tubes.de
- Sandström, R. (2014). 5 - Creep strength of austenitic stainless steels for boiler applications. In A. Shibli (Ed.), *Coal Power Plant Materials and Life Assessment* (pp. 127-146): Woodhead Publishing.
- Sarver, J. M., & Tanzosh, J. M. (2003). *Steam oxidation testing of candidate ultra-supercritical boiler materials*. Paper presented at the The 28th International Technical Conference on Coal Utilization and Fuel Systems, Clearwater, Florida, USA.
- Sato, T., Fukuda, Y., Mitsuhara, K., & Sakai, K. (2005). *The Practical Application and Long-term Experience of New Heat Resistant Steels to Large Scale USC Boiler*. Paper presented at the Advances in Materials Technology for Fossil Power Plants.
- Schütze, M. (2005). Modelling oxide scale fracture. *Materials at High Temperatures*, 22(1-2), 147-154.
- Schütze, M., Tortorelli, P., & Wright, I. (2010). Development of a comprehensive oxide scale failure diagram. *Oxidation of metals*, 73(3-4), 389-418.
- Shafiee, S., & Topal, E. (2009). When will fossil fuel reserves be diminished? *Energy Policy*, 37, 181-189.
- Shibli, A. (2011). 7 - Boiler steels, damage mechanisms, inspection and life assessment. In J. E. Oakey (Ed.), *Power Plant Life Management and Performance Improvement* (pp. 272-303): Woodhead Publishing.

- Shibli, A., & Ford, J. (2014). 13 - Damage to coal power plants due to cyclic operation. In A. Shibli (Ed.), *Coal Power Plant Materials and Life Assessment* (pp. 333-357): Woodhead Publishing.
- Shingledecker, J. P., Stantella, M. L., Wilson, D. F., & Wright, I. G. (2009). State of knowledge for advanced austenitics: Progress update 2009: EPRI.
- Speight, J. G. (2013). *Coal-fired power generation handbook.*: Scrivener Publishing, John Wiley & Sons.
- Starr, F. (2014). 3 - High temperature materials issues in the design and operation of coal-fired steam turbines and plant. In A. Shirzadi & S. Jackson (Eds.), *Structural Alloys for Power Plants* (pp. 36-68): Woodhead Publishing.
- Tonti, A. (2014). 8 - Residual life evaluation techniques, defect assessment procedures and monitoring in coal power plants. In A. Shibli (Ed.), *Coal Power Plant Materials and Life Assessment* (pp. 199-228): Woodhead Publishing.
- Uerlings, R., Bruch, U., & Meyer, H. (2008). KOMET 650-Investigations of the operational behavior of boiler materials and their welded joints at temperatures up to 650oC. *VGB Power Tech-International Journal for Electricity and Heat Generation*, 3, 43-49.
- VdTÜV. (2007). Material Data Sheet 547
- Vikrant, K. S. N., Ramareddy, G. V., Pavan, A. H. V., & Singh, K. (2013). Estimation of residual life of boiler tubes using steamside oxide scale thickness. *International Journal of Pressure Vessels and Piping*, 104, 69-75.
- Viswanathan, R., Coleman, K., & Rao, U. (2006a). Materials for ultra-supercritical coal-fired power plant boilers. *International Journal of Pressure Vessels and Piping*, 83, 778-783.
- Viswanathan, R., Henry, J. F., Tanzosh, J., Stanko, G., & Shingledecker, J. (2005). *U.S. Program on Material Technology Ultrasupercritical Coal Power Plants*. Paper presented at the ECCO Creep Conference, London.
- Viswanathan, R., Purgert, R., & Rao, U. (2002). Materials technology for advance coal power plants: EPRI.
- Viswanathan, R., Sarver, J., & Tanzosh, J. (2006b). Boiler materials for ultra-supercritical coal power plants—steamside oxidation. *Journal of Materials Engineering and Performance*, 15(3), 255-274.

- Wagner, W., & Kretzschmar, H.-J. (2007). *International Steam Tables-Properties of Water and Steam based on the Industrial Formulation IAPWS-IF97: Tables, Algorithms, Diagrams, and CD-ROM Electronic Steam Tables-All of the equations of IAPWS-IF97 including a complete set of supplementary backward equations for fast calculations of heat cycles, boilers, and steam turbines*: Springer.
- Wang, Z. W., Zhang, Q., Xia, L. Z., Wu, J. T., & Liu, P. Q. (2015). Thermomechanical Analysis of Pressure Vessels With Functionally Graded Material Coating. *Journal of Pressure Vessel Technology*, 138(1), 011205-011210.
- Weitzel, P. S. (2011). *Steam Generator for Advanced Ultra-Supercritical Power Plants 700 to 760°C*. Paper presented at the ASME 2100 Power Conference, Denver, CO.
- Wheeldon, J. M., & Shingledecker, J. P. (2013). 4 - Materials for boilers operating under supercritical steam conditions. In D. Zhang (Ed.), *Ultra-Supercritical Coal Power Plants* (pp. 81-103): Woodhead Publishing.
- Wright, I. G., & Dooley, R. B. (2010). A review of the oxidation behavior of structural alloys in steam. *International Materials Reviews*, 55(3), 129-167.
- Wright, I. G., Maziasz, P. J., Ellis, F. V., Gibbons, T. B., & Woodford, D. A. (2004b). *Materials issues for turbines for operation in ultra-supercritical steam*.
- Wright, I. G., Schütze, M., Paterson, S. R., Tortorelli, P. F., & Dooley, R. B. (2004a). *Progress in prediction and control of scale exfoliation on superheater and reheater alloys*. Paper presented at the EPRI International Conference on Boiler Tube and HRSG Tube Failures and Inspections.
- Wright, I. G., & Shingledecker, J. P. (2015). Rates of fireside corrosion of superheater and reheater tubes: making sense of available data. *Materials at High Temperatures*, 32(4), 426-437.
- Yamamoto, Y., Brady, M. P., Lu, Z. P., Maziasz, P. J., Liu, C. T., Pint, B. A., . . . Payzant, E. A. (2007). Creep-Resistant, Al₂O₃-Forming Austenitic Stainless Steels. *Science*, 316-433.
- Zhang, D. (2013). 1 - Introduction to advanced and ultra-supercritical fossil fuel power plants. In D. Zhang (Ed.), *Ultra-Supercritical Coal Power Plants* (pp. 1-20): Woodhead Publishing.
- Zhang, X. (2013). Inaugural Issue, Coal's role in the global energy mix: trading water or full steam ahead. *Cornerstone 1*.

Zhong, X., Wu, X., & Han, E.-H. (2012). The characteristic of oxide scales on T91 tube after long-term service in an ultra-supercritical coal power plant. *The Journal of Supercritical Fluids*, 72, 68-77.

University of Malaya

LIST OF PUBLICATIONS

1. W.H. Yeo, A.T. Fry, S. Ramesh, R. Mohan, H.L. Liew, J.I. Inayat-Hussain, J. Purbolaksono. (2014). Simulating the implications of oxide scale formations in austenitic steels of ultra-supercritical fossil power plants. *Engineering Failure Analysis*, 42, 390-401. (ISI-Cited Publication)
2. W.H. Yeo, A.T. Fry, J. Purbolaksono, S. Ramesh, J.I. Inayat-Hussain, H.L. Liew, M. Hamdi. (2014). Oxide scale growth and presumed exfoliation in a 700 °C or higher steam condition: A simulation study for future operations of ultra-supercritical power plants. *The Journal of Supercritical Fluids*, 92, 215-222. (ISI-Cited Publication)

University of Malaya